

Proceedings of the 11th Meeting of Japan CF Research Society

Edited by Ken-ichi Tsuchiya

December 11-12, 2010

Iwate University, Japan

Copyright © 2011 by Japan CF Research Society

All rights reserved. No part of this publication may be reproduced, stored in a retrieval system, or transmitted, in any form or by any means, electronic, mechanical, photocopying, recording or otherwise, without the prior permission of the copyright owner.

PREFACE

This is the Proceedings of the 11th Meeting of Japan CF-Research Society (JCF11), which was held at Iwate University on December 11-12, 2011. In this meeting, 14 oral presentations were given and 13 papers were submitted to the editorial board. They were peer reviewed by the referees, and revised for the publication as the proceedings. As a result, 8 papers concerning the experiment and 5 papers concerning the theory were accepted. Editing them, we have successfully completed our work. Now, the abstracts of all the presentations are available at our web-site <http://jfrs.org>. The electronic version of the proceedings is also available in the same web-site. Needless to say, any responses from the world scientists will be welcomed.

At first, the deadline of the proceedings submission was March 14, 2011. However, a huge earthquake happened in the Tohoku region in Japan on March 11. This earthquake disaster seriously damaged the TEPCO Fukushima Daiichi Nuclear Power Station. The influence of this accident to the society of Japan was enormous. And also in JCF, we could not help extending the deadline of the proceedings submission. As scientists who research the nuclear energy from a new viewpoint, we think we should make further efforts in order to get over this crisis.

Finally, we would like to thank all the participants, and also the people who have collaborated in organizing this meeting. In particular, we would like to express our sincere appreciation to the financial support by The Thermal & Electric Energy Technology Foundation.

Finishing the editing work, we would like to express heartfelt condolences to the people who passed away by the earthquake disaster.

Editor in Chief

Ken-ichi Tsuchiya (Tokyo National College of Technology)

August 2011

CONTENTS

Preface

<i>K. Tsuchiya</i> -----	i
--------------------------	---

EXPERIMENTS

Heat Generation from the Palladium Deuteride

<i>Ken-ichi Tsuchiya, Hiroshi Arikawa, Masao Ozaki and Shigeru Sasabe</i> -----	1
-------------------------------------------------------------------------------------	---

Energetic Charged Particle from Multi-layered Pd Sample by Hydrogen Permeation

<i>Y. Suzuki, S. Sato, T. Kuroha, H. Ohata, T. Mihara, S. Narita and H. Yamada</i> -----	5
----------------------------------------------------------------------------------------------	---

Hydrogen Isotope Absorption/Adsorption Characteristics of Pd-Zr Oxide Compounds

<i>Y. Miyoshi, H. Sakoh, A. Taniike, A. Kitamura, A. Takahashi, R. Seto and Y. Fujita</i> -----	10
-----------------------------------------------------------------------------------------------------	----

Hydrogen Isotope Absorption/Adsorption Characteristics of Ni-Pd Binary Nano-Particles

<i>H. Sakoh, Y. Miyoshi, A. Taniike, A. Kitamura, A. Takahashi, R. Seto and Y. Fujita</i> -----	16
-----------------------------------------------------------------------------------------------------	----

Search for Nuclear Phenomena in Deuterium Irradiation to Nano-Structured Metal under Glow Discharge

<i>H. Ougida, H. Sasaki, A. Tamura, S. Narita and H. Yamada</i> -----	23
-----------------------------------------------------------------------	----

Search for Nuclear Phenomena in Deuterium Desorption Process with Multi-layered Metal Complex

<i>M. Kawashima, A. Taguchi, N. Oikawa, H. Yamada, and S. Narita</i> -----	29
----------------------------------------------------------------------------	----

Systematic Uncertainties of Isotopic Abundance Measured by TOF-SIMS

<i>S. Narita, H. Yamada, H. Sasaki, H. Ougida, S. Sato and Y. Suzuki</i> -----	36
--------------------------------------------------------------------------------	----

Detection of Energetic Charged Particles from Thin Metal Cathodes in Heavy and Light Water Electrolysis Using CR39

<i>H. Yamada, S. Narita, S. Sato, H. Aizawa, K. Mita, Y. Takahashi, Y. Abe, Y. Shida and H. Nanao</i> -----	41
-----------------------------------------------------------------------------------------------------------------	----

THEORIES

Mesoscopic Catalyst and D-Cluster Fusion <i>A. Takahashi, A. Kitamura, Y. Miyoshi, H. Sakoh, A. Taniike, R. Seto and Y. Fujita -----</i>	47
Brief Explanation of Experimental Data Set on Excess Heat and Nuclear Transmutation in Multiplly Nanocoated Ni Wire <i>Hideo Kozima and Francesco Celani -----</i>	53
Localization of Nuclear Reactions in the Cold Fusion Phenomenon <i>Hideo Kozima -----</i>	59
Numerical Simulation of the Motion of Cascade Vortices in the Sub-Surface Layer <i>Hiroo Numata -----</i>	70
Neutron Emission in the Cold Fusion Phenomenon <i>Hideo Kozima -----</i>	76

Heat generation from the Palladium deuteride

Ken-ichi TSUCHIYA^{a)}, Hiroshi ARIKAWA^{a)}, Masao OZAKI^{b)} and Shigeru SASABE^{c)}

^{a)} Tokyo National College of Technology, 1220-2 Kunugida, Hachioji, Tokyo 193-0997
E-mail; tsuchiya@tokyo-ct.ac.jp

^{b)} Tokyo University of Agriculture, 1-1-1 Sakuragaoka, Setagaya, Tokyo, 156-8502

^{c)} Tokyo Metropolitan University, 1-1 Minami-Ohsawa, Hachioji, Tokyo 192-0397

Abstract: In this study, we have done deuterium loading to Pd black in order to find the sign of the nuclear reaction in solid. The loading were done two times repeatedly. The loading ratio in the first run was higher than that of the second run because the starting material was oxidized. After the loading, we have observed the heat generation from the palladium deuteride in the air. We consider that this exothermal reaction depends on the usual chemical reactions. They are the deuterium desorption and the heavy water formation.

Keywords: palladium oxide, palladium deuteride, Raman spectroscopy

1 Introduction

In JCF10, the heat generations during the deuterium loading to the Pd nano-powders were reported by Hioki et al. [1] and Sasaki et al. [2]. Commonly, they observed the 1st phase different from the 2nd one in the loading. In the 1st phase, the deuterium pressurization to 1MPa was done. In this phase, characteristics of heat generation by the two types of chemical reactions were observed. They were heavy water formation because of the reduction reaction of the palladium oxide and the deuterium absorption reaction. In the 2nd phase, the deuterium pressure was stabilized at 1MPa and the heat generation close to the detection limit of the calorimeter was observed. Both of the groups reported that this anomaly was hardly explained by the chemical reactions.

In this study, we have done deuterium loading experiment to the Pd powders and observed the heat generation from the powder of Pd deuteride. The Raman spectroscopy was used to observe the

quantum state of the optical phonon induced by interactions between deuterons. This observation is based on the Sharman's work which has investigated the DD interactions in the palladium deuteride using Raman spectroscopy [3].

2 Experimental

Firstly, we have done deuterium loading to Pd powder using the glass tube apparatus. It is shown in Fig.1. We can know the loading ratio by observing the decrease of the pressure in the apparatus.

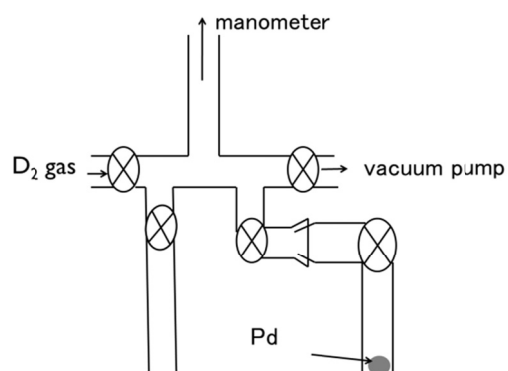


Fig.1 Deuterium loading apparatus.

We used two types of Pd powders as loading materials. One is made by filing the Pd plate of 99.9% purity (Tanaka Kikinzoku Kogyo). The other is Pd black (Kojima Chemical Co.).

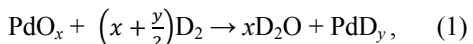
Secondly, we have observed the Raman spectra of Pd deuteride. The excitation wavelength of the Raman spectroscopy (NRS3100, JASCO) is 532.25 nm. The tube including the Pd deuteride shown in Fig.1 can be taken off after closing the cock and be put into the detection chamber of the Raman spectroscopy.

3 Results and discussions

3.1 Deuterium loading

The time behaviors of deuterium loading for the Pd powders are plotted in Figs.2 and 3. In each case, Run2 was done after completing Run1 with the degassing operation.

In Fig 2, the equilibrium D/Pd ratios for Run1 and Run2 are 0.7 and 0.6, respectively. The rise time of Run2 is about 10 min. while Run1 takes 1000 min. to reach plateau. This sample was made by filing the Pd plate before the gas loading. This process may contaminate the surface of the sample and lead to the large raise time of the first loading. In Fig.3 for Pd black, the equilibrium D/Pd ratios for Run1 and Run2 are 0.8 and 0.6, respectively. The raise times for both runs are about 2 min., which are shorter than that for the plain Pd powder as shown in Fig.2. In Figs.2 and 3, the equilibrium loading ratios of the first runs are commonly higher than those of the second runs. Since the reduction reactions of the deuterium oxides are written as



the energy accompanied by this reaction is defined as

$$E = xQ_r + yQ_D, \quad (2)$$

where Q_r and Q_D mean reduction energy and

deuteride formation energy, respectively [2]. In the first runs, the appearance D/Pd ratio $2x+y$ were observed because the starting materials were oxidized. However, the ratio y was observed in the second runs because the materials were completely reduced at the first runs. Therefore, we recognize the true loading ratio to be 0.6.

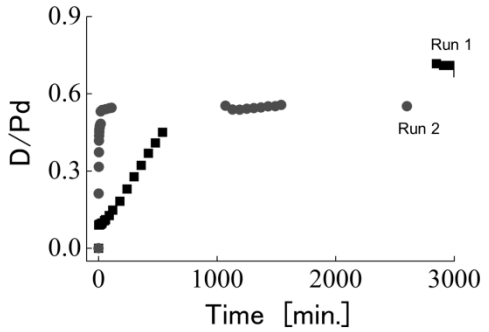


Fig.2 Time behavior of deuterium loading
Pd powder, which was made by filing down the plate, was used for the loading material. Run2 was done after completing Run1 with the degassing operation.

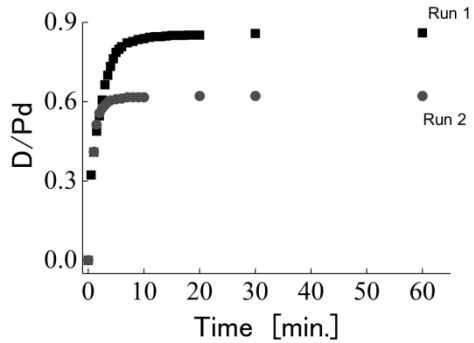


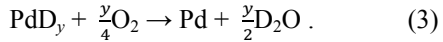
Fig.3 Time behavior of deuterium loading
Pd black was used for the loading material. Run2 was done after completing Run1 with the degassing operation.

3.2 Observations of the Raman spectra and the heat generation

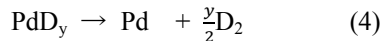
We observed the Raman spectra in order to know the quantum states of deuterons in the samples. The results are plotted in Figs.4 and 5. Finally, the samples were taken out from the test tube. Then we found the heat generation from

some samples. Fig.6 shows the burning facial tissue due to the heat from the Pd deuteride. The Raman spectra of the samples after the heat generation are also plotted in Figs.4 and 5. In Figs.4 and 5, broad peaks due to the interactions between deuterons at 58 meV [3] are found on the spectra before the heat generation. However, they are disappeared on the spectra after the heat generation. This means that deuterons in the samples are released to the air at the heat generation.

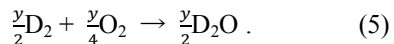
We did not do the calorimetry at the heat generation from the palladium deuteride because we did not have suitable instrument for the calorimetry. However, we guess that the heat generation from the palladium deuteride is caused by the chemical reaction of the heavy water formation, which is written as



This reaction is divided into the following two steps as



and



Therefore, the reaction energy of eq.(3) is written as

$$E = yQ_D' + \frac{y}{2}Q_{HW}, \quad (6)$$

where Q_D' and Q_{HW} mean the deuterium desorption energy and the heavy water formation energy, respectively. It is well known that the formation energy of the liquid water is 286kJ/mol=2.96eV/(H₂O molecule), which is almost same for heavy water. On the other hand, the deuterium desorption energy of Pd black is estimated to be ranging from -0.2 to -0.45eV/(Pd atom) [2]. Therefore, the reaction in eq.(3) is estimated to be exothermal. This reaction rate may be small because deuteriums are slowly released from the surface of the palladium powder. However, it is considered to be enough for the

released deuterium gas to fire, as shown in Fig.6.

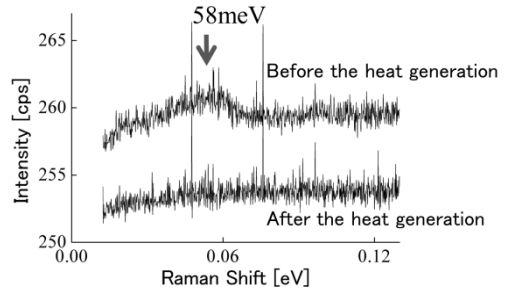


Fig.4 Raman spectra of Pd deuteride before and after the heat generation. The time behavior of deuterium loading to this sample is plotted in Fig.2.

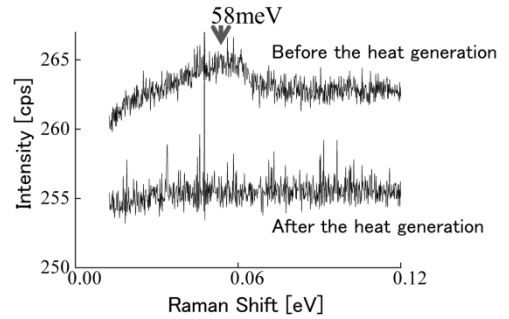


Fig.5 Raman spectra of Pd deuteride before and after the heat generation. The time behavior of deuterium loading to this sample is plotted in Fig.3.



Fig.6 Burning facial tissue due to the heat from the Pd deuteride. The time behavior of deuterium loading to this sample is plotted in Fig.3.

4 Conclusions

The conclusions of this study are summarized as following.

- (i) The palladium powders used in this study absorbed deuterium to the atomic ratio of 0.6 at the second runs after the degasing operation for the samples of the first runs. The loading ratios of the first runs were commonly higher than those of the second runs, because the starting materials included palladium oxide which wasted deuterium by the reduction reaction. This agrees with the results of Hioki [1] and Sasaki [2].
- (ii) After exposing the palladium deuteride to the air, we observed burning facial tissue due to the heat generated on the surface of the palladium deuteride. We guess that this is caused by the burning of the deuterium gas released from the bulk by the catalysis of Pd. This is regarded as the heavy water formation reaction between the oxygen in the air and the deuterium released from the palladium deuteride. It is written as eq.(3).
- (iii) In this study, we could not find the signs of the nuclear reactions. In the future work, we will try to obtain the sign of the nuclear reaction from a marked change of the Raman spectra.

Acknowledgements

The authors wish to thank Professor Akito Takahashi of Osaka University, Professor Akira Kitamura of Kobe University and Professor Hiroshi Yamada of Iwate University for helpful discussions and encouragements. We also wish to thank Professor Noboru Akuzawa of TNCT for the advices on the hydrogen storage techniques.

References

1. T. Hioki, H. Azuma, T. Nishi, A. Itoh, T. Motohiro and J. Kasagi, "Hydrogen/deuterium absorption capacity of Pd nanomaterials and its relation with heat generated upon loading of hydrogen isotope gases", Proc. JCF10, p1
2. Y. Sasaki, Y. Miyoshi, A. Taniike, A. Kitamura, A. Takahashi, R. Seto and Y. Fujita, "Measurement of heat and radiation from Pd nano-powders during absorption of hydrogen isotopes", Proc. JCF10, p14
3. R. Sherman, H. K. Birnbaum, J. A. Holy and M. V. Klein, "Raman studies of hydrogen vibrational modes in palladium", Phys. Lett., 62A(1977)353

Energetic Charged Particle from Multi-layered Pd Sample by Hydrogen Permeation

Y. Suzuki, S. Sato, T. Kuroha, H. Ohata, T. Mihara, S. Narita and H. Yamada,

Department of Electrical and Electronic Engineering, Iwate University, Ueda 4-3-5, Morioka,
020-8551 Japan t2309031@iwate-u.ac.jp

Abstract

We have performed a test of high pressure H₂ gas permeation using the Pd sample with multi-layers and Li deposition in conjunction with using CR39 for detection of energetic charged particle. As the results, we observed more etch pits on the area of CR39 facing the Pd sample than these on other area covered by the metal foil. Etch pit density observed on facing the Pd sample area was around 80 times larger than that on the other area. There was no increasing number of etch pits observed when Pd samples without multi-layer and the deposited element were used. This result suggests the possibility that a charged particles was emitted from Pd sample during H₂ gas permeation process and presents the possibility of the low energy nuclear reaction for this hydrogen system.

Keywords: multi-layered Pd sample, H₂ permeation, CR39, low energy nuclear reaction

1. Introduction

We have been studied low energy nuclear reaction(LENR) for high pressure H₂ permeation method using TOF-SIMS. As a result, we observed increasing B and Si peaks in ToF-SIMS spectra on multi-layered Pd sample with Li deposition after H₂ permeation. The result suggests that the LENR occurs in H₂ system as well as in D₂ system. However, change in isotope abundance ratio of these elements was not found. Therefore, few reliable date of LENR has still been obtained from this hydrogen system.

On the other side, the plastic track detector CR39 has became a popular method to measure charged particle emissions in LENR studies. Oriani et al.¹⁾ and Yamada et al.²⁾ performed

light water electrolysis of Li₂SO₄ solution using CR39 and have reported the generation of charged particle emission during the electrolysis. The results indicate the LENR occurring in the light water electrolysis.

When LENR occurs in hydrogen system using H₂ permeation method, there exists a possibility that a charged particle emission occurs. Accordingly, we have performed a H₂ gas permeation experiment using CR39 to detect energetic charged particle.

2. Experimental

Fig. 1 shows the Pd/CaO multi-layered sample. The base Pd foil of 12.5 x 12.5 x 0.1 mm in size was washed by acetone for 30 min. Next, the sample was annealed for 8h at

900 °C. It was washed by aqua regia to remove metallic impurities, followed by ultrasonic cleaning in ultra pure water for 30 min. The CaO and Pd thin films were formed on the Pd foil by Ar ion beam sputtering. Each thickness of CaO and Pd films were 2 and 18 nm, respectively. Only the thickness of uppermost Pd film was 40 nm. Total numbers of layers were 10. After forming the thin films, small amount of Li was deposited on the uppermost surface of the multi-layered Pd sample by an electrochemical method in a $\text{Li}_2\text{SO}_4/\text{H}_2\text{O}$ solution.

Fig. 2 shows the H_2 gas permeation system used in this experiment. The sample was placed between the upper and the lower stream chamber. H_2 gas was introduced into the upper chamber with pressure 1 MPa, followed by evacuation of lower stream chamber. The gas moved downstream passing through the sample at 70 °C by difference of pressure. The time period of H_2 gas permeation was 14 days.

The track detector CR39 (Fukuvi Chemical Industry Co.) was used to detect charged particles for the gas permeation experiment. The CR39 of 9 x 20 mm in size was placed above the Pd sample at the distance of 3 mm from the sample surface in the upper chamber, as shown in Fig. 3. After the gas permeation, the CR39 was removed from the holder and etched in 5N NaOH solutions for 8h at 70 °C. After the etching, the surface of the CR39 was scanned to count the number and to measure the size of the etch pits using a digital microscope system (KEYENCE VHX-200).

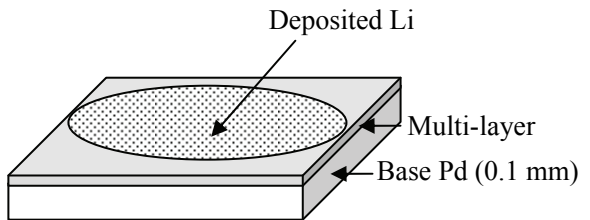


Fig. 1 Multi-layered Pd sample.

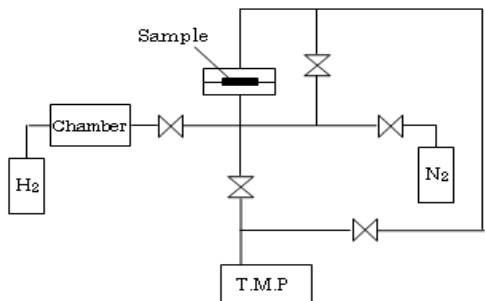


Fig. 2 H_2 gas permeation system.

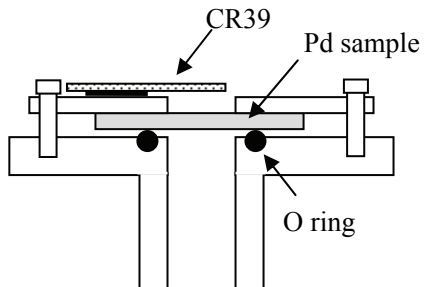


Fig. 3 Sample holder with CR39.

Fig. 4 shows the position of the CR39 set on the holder. Here, the area of CR39 facing Pd sample is designated FOREGROUND and the other area covered by the metal foil BACKGROUND. The FOREGROUND has about 12.5 mm^2 and the BACKGROUND 167.5 mm^2 . The BACKGROUND is about 13 times larger than the FOREGROUND.

3. Result and Discussion

Fig. 5 shows the relation between the number and diameter of etch pit on CR39 for a sample after H₂ gas permeation. Number of 12 and 2 etch pits were observed in the FOREGROUND and the BACKGROUND, respectively. The density of etch pits on the FOREGROUND was around 80 times larger than that on the BACKGROUND. The measured diameter of etch pits in the FOREGROUND ranges 5-7 μm , as shown in Fig. 5. Another diameter distribution of etch pit obtained from next run under the same experimental condition is shown in Fig. 6. Number of 5 and 3 etch pits were observed in the FOREGROUND and the BACKGROUND, respectively. The measured diameter of etch pit in the FOREGROUND ranges 5-7 μm , which is same as that obtained in Fig. 5, even though the number of etch pit decreased to 5 in the FOREGROUND.

In these 2 experiments, we observed even higher density of etch pit on the area of CR39 facing Pd sample than that on other area covered by the metal foil after H₂ gas permeation. This result suggests the possibility that a charged particle was emitted from Pd sample during H₂ gas permeation. However other possible sources for the etch pits would be active H₂ gas, bulk defect and radioactive atoms in environment. Thus, we carried out the following control and blank experiments.

The control experiment was performed to search the effect of active H₂ gas on producing defect in the CR39. A plane Pd foil sample without any layers and deposited elements was

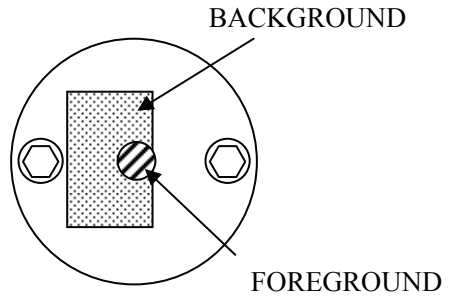


Fig. 4 CR39 set on the holder.

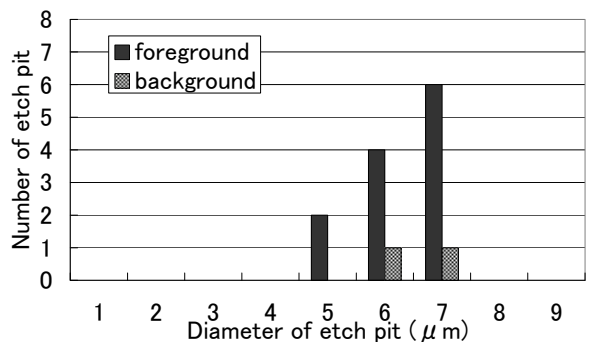


Fig. 5 Diameter distribution of etch pit after H₂ gas permeation (first run).

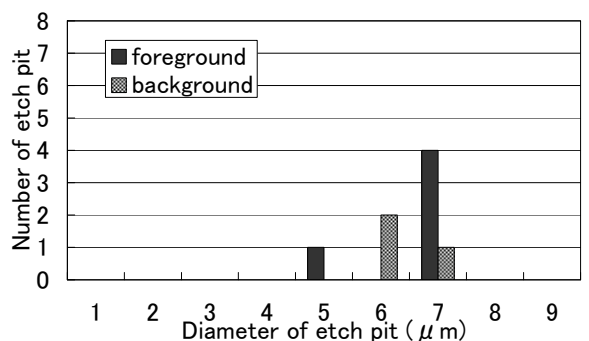


Fig. 6 Diameter distribution of etch pit after H₂ gas permeation (second run).

used. The gas pressure of 1 MPa and the exposure time of 14 days were same as those for the above mentioned 2 experiments. Fig. 7 shows the diameter distribution for the control

experiment. Only 1 etch pit was observed in the FOREGROUND and 3 in the BACKGROUND. There was no increasing number of etch pit observed in the FOREGROUND. Therefore, it is not likely that the anomalous increasing number of etch pit in these FOREGROUND in Fig. 5 and 6 was produced by the active H₂ gas

In this study the sheet of CR39 was stored in an incubator and the surface of CR39 chips was covered by protection seal until just before the setting to the test chamber. However, there was another possibility that the sheet of CR39 had already manufacturing defect before the setting. Further, the CR39 chip could have been exposed by the charged particles from environment before the setting and during relatively longer etching process. Consequently, we conducted another blank test, where a CR39 chip was etched immediately after cutting out from the sheet to search for etch pits attributed to the defects and radioactive source in environment. The diameter distribution appeared in relatively random feature for the blank tests as well as gas permeation tests, even though the diameter for this two kinds of tests ranges 5-10 μ m. One of the diameter distributions obtained from the blank test is shown in Fig. 8, where total 7 etch pits were observed on the whole surface area of the CR39 chip and the measured diameter of these etch pits ranges 7-10 μ m. It is considered that this figure provides the characteristic distribution for the blank test and that these few number of etch pits could be attributed to manufacturing defect and radioactive source in environment. The average of measured diameter ranging

7-10 μ m for blank test is larger than that obtained for the permeation experiment used multi-layer Pd sample with Li deposition. This means that the source of etch pits in high density in the FOREGROUND differ from these observed in these control and blank experiments.

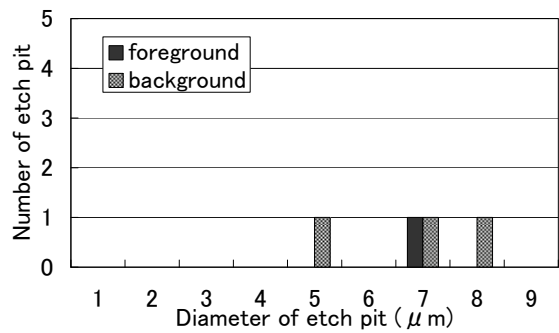


Fig. 7 Diameter distribution of etch pit after H₂ gas permeation used bulk Pd.

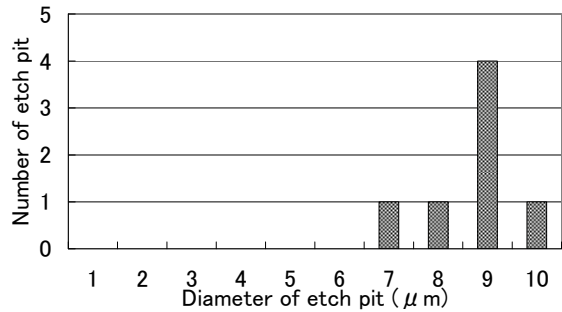


Fig. 8 Diameter distribution of etch pit on the as-received CR39.

In other words, it can be concluded that etch pits observed in the FOREGROUND are not attributed to manufacturing defect or radioactive source in environment. Then It would indicate that a charged particle is emitted from Pd sample during H₂ gas permeation. However, the number of experiment performed

is so few that we need more experiments to have the reproducibility.

The diameter of etch pit of anomalously increasing the number ranges $5\text{-}7 \mu\text{m}$, as mentioned above. Referring the date for calibration by Lipson et al.³⁾, the diameter $5\text{-}7 \mu\text{m}$ correspond to less than 3 MeV of proton and larger than 17 MeV of alpha particle . It should be noticed that both the etching time and the solution density in this study were different from those used by Lipson et al. The former was 8h and the later was 5N in this study, the former 7h and the later 6N in the study of Lipson et al.

When the charged particle is a proton with 3 MeV, there would be following unknown and generally unacceptable process. At the first stage of reactions, a deuterium is produced from two protons in one of the LENRs. Next, the well known d-d reaction

$$d+d \rightarrow p(3.02 \text{ MeV}) + t(1.01 \text{ MeV})$$

takes place at low temperature to produce the proton, which might be detected by the CR39 chip used in the present study.

4. Conclusion

We have performed for H_2 gas permeation experiment using the Pd sample with multi-layers and Li deposition in conjunction with using CR39 to detect of energetic charged particle. We have observed even higher density of etch pits on the area of CR39 facing the Pd sample than these on other area covered by the metal foil. The density of etch pits observed in the FOREGROUND was around 80 times larger than that in the BACKGROUND. The

anomalous increasing in number of etch pit was not observed when Pd samples without multi-layer and deposited element were used. These anomalous etch pits could not be attracted to manufacturing defect or charged particles in environment. All the results would suggest the possibility that a charged particle is emitted from the Pd sample during H_2 gas permeation process and that LENR occurs in the hydrogen system.

References

- 1) R.A.Oriani ; Reproducible Evidence for the Generation of a Nuclear Reaction During Electrolysis(2008)
- 2) H. Yamada et al., Proc. 10th Meeting of Japan CF research Society, p. 41(2010)
- 3) A.G.Lipson and G.H.Miley ; Proceedings of the 10th International Conference on Cold Fusion, pp.539-558(2003)
- 4) H. Yamada et al., Proc. 9th Meeting of Japan CF research Society, p. 46(2008)
- 5) H. Yamada et al., Proc. 8th Meeting of Japan CF research Society, p. 26(2007)
- 6) H. Yamada et al., Proc. 7th Meeting of Japan CF research Society, p. 28(2006)
- 7) H. Yamada et al., Proc. 6th Meeting of Japan CF research Society, p. 48(2005)

Hydrogen Isotope Absorption/Adsorption Characteristics of Pd·Zr Oxide Compounds

Y. Miyoshi^{1*}, H. Sakoh¹, A. Taniike¹, A. Kitamura¹

A. Takahashi², R. Seto², and Y. Fujita²

¹Division of Marine Engineering, Graduate School of Maritime Sciences, Kobe University;

Higashinada-ku, Kobe 6580022, Japan; *101w527w@stu.kobe-u.ac.jp

²Technova Inc., Chiyoda-ku, Tokyo 1000011, Japan

Abstract. In order to confirm heat and ^4He generation by deuterium absorption in nano-sized Pd powders reported by Arata and Zhang, the Pd-Zr oxide composite “PZ” samples supplied by Santoku Corporation were tested using the twin absorption system for simultaneous D_2 and H_2 gas absorption. The observed loading ratios and the specific heat-release-data in the first phase of as-received and oxidized PZ sample runs were both very large, while those for the de-oxidized ones were small and close to data of bulk Pd sample. We observed two sub-phases (1a and 1b) in the first phase for the as-received and the oxidized PZ sample. The 1a-phase, characterized by rapid absorption/adsorption and high heat output, is characteristic of nano particles containing oxygen, probably by the process occurring in the near-surface region. A rather large isotope effect in the differential heat of sorption has been observed in this phase.

Keywords: Pd-Zr nano-powder, Deuterium absorption, Forced oxidation, Forced reduction, Sub-phases, Differential heat of hydrogen uptake, Anomalously large heat and loading ratio, Role of PdO layer

1. Introduction

To replicate the phenomenon of heat and ^4He generation reported by Arata and Zhang [1], Kobe Group, Kobe University and Technova Inc., constructed the D_2/H_2 absorption system composed of two identical set of chambers capable of calorimetry (an A₁-A₂ twin system). In the past work using the samples supplied by Santoku Corporation as well as those purchased from Nilaco Corp. [2-6], we observed the large first-phase heat generation which increases with fineness of the sample surface for as-received samples, but the first-phase heat decreased very

much in repeatedly used samples. Since it is thought that oxygen in the sample contributes to the large heat generation greatly, we examined the effects of oxygen by the forced oxidization and the forced reduction of samples.

2. Experimental apparatus and procedure

The experimental setup is shown schematically in Fig. 1. The system is composed of two identical chambers, each of which contains a reaction chamber equipped with calorimetry system and connected to an independent gas supply system. To start an absorption run, the reservoir tanks are filled with D_2 (H_2) gas at some pressure ranging from 0.4 MPa to 1.0 MPa, and just before the gas is introduced into the reaction chamber through the “Super Needle” valve, the gas cylinder is separated by closing the valve V_0 to make the reservoir-reaction chamber system a closed system. The each gas is purified by passing it through a liquid N_2 cold trap.

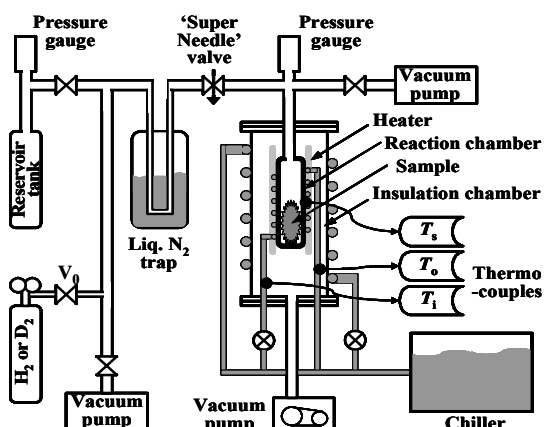
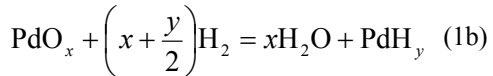
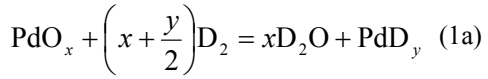


Fig. 1. Schematic of one-part of the twin system.

First, the as-received (virgin) sample is baked to outgas the sample, and subjected to the #1 run. The #2 run is done after the forced deoxidization of sample after the #1 run. And the #3 run follows the forced oxidization of the sample after the #2 run. The forced deoxidization of the samples was done by leaving it in atmospheric deuterium (protium) gas at a temperature of 573 K. It is assumed that the sample was completely reduced to become pure Pd-ZrO₂. On the other hand the forced oxidization of Pd in the PZ sample was done by leaving it in atmospheric oxygen gas at a temperature of 473 K for 30 hours. The oxidization fraction, x of PdO_x, is calculated from the pressure change in the reaction chamber during the oxidization process.

The chemical reactions considered to contribute after the D₂ (H₂) gas introduction is shown below.



The oxygen pickup reaction forming D₂O (or H₂O) with a reduction energy of Q_{red} [eV/atom-Pd] and the “hydridation” reaction forming the hydride atoms PdD(H) and surface adatoms with a reaction energy of $Q_{\text{D(H)}}$ [eV/atom-D(H)] are taken into account. We define the first phase as the “chemical” heat generation period. The specific output energy, E_1 , either in unit of kJ/g-Pd or eV/atom-Pd is expressed as;

$$E_1 = xQ_{\text{red}} + yQ_{\text{D(H)}} \quad (2)$$

We take the value of $Q_{\text{red}} = 1.77$ (1.63) eV/atom-Pd from literatures.

3. Results and discussion

The sample “PZ” used in the present work is a mixed powder of oxides of Pd (31.2 molar %) and Zr (68.8 %). Temporal evolution of the typical absorption runs, D(H)-PZ13(14)#3, is shown in Fig. 2. Heat generation continues till about 100 min, when the pressure begins to increase above several tens of kPa. At the same time, absorption and adsorption are completed. We call this period the first phase, and do the rest the second phase.

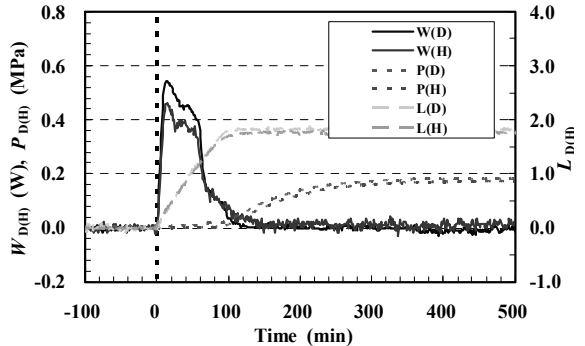


Fig. 2. Evolution of output heat, $W_{\text{D(H)}}$, pressure, $P_{\text{D(H)}}$, and time-dependent loading ratio, $L_{\text{D(H)}}$, in the typical runs D(H)-PZ13(14)#3.

Table 1 and Figs. 3(a) - (c) summarize the 1st-phase parameters for the runs D(H)-PZ11(12)#1 through D(H)-PZ13(14)#3. We have large values for the specific output power E_1 , the loading ratio D(H)/Pd and the hydridation energy $Q_{\text{D(H)}}$ compared to those for the PP (0.1-μmφ Pd powder) and the PB (Pd-black) samples [3]. Here it should be noted that $Q_{\text{D(H)}}$ for the #1 runs is a tentative value, since we do not know the value of x for the as-received samples, and $x = 0$ is assumed to calculate $Q_{\text{D(H)}}$. The #2 runs gave greatly reduced values for E_1 and loading ratio D(H)/Pd. However, the #3 runs significantly recovered the large values, with the

Table 1. Summary of first-phase parameters in PZ11#1~PZ14#3.

Run No.	O/Pd (=x)	Specific energy , E_1		D(H)/Pd (=y)	$Q_{D(H)}$ [eV/H]	xQ_R [eV]	Remarks
		[kJ/g-Pd]	[eV/atom-Pd]				
D-PZ11 #1	unknown	1.68± 0.05	1.86	2.24	0.83	assumed to be 0	As-received
D-PZ11 #2	0	0.14± 0.01	0.16	0.56	0.29	0	Deoxidized
D-PZ11 #3	0.086	1.87± 0.07	2.07	1.96	0.98	0.14	Oxidized
H-PZ12 #1	unknown	1.74± 0.13	1.92	2.25	0.85	assumed to be 0	As-received
H-PZ12 #2	0	0.14± 0.01	0.15	0.45	0.35	0	Deoxidized
H-PZ12 #3	0.054	1.16± 0.05	1.28	1.33	0.88	0.10	Oxidized
D-PZ13#1	Unknown	2.48±0.03	2.73	2.29	1.19	assumed to be 0	As-received
D-PZ13#2	0	0.17±0.06	0.19	0.56	0.33	0	Deoxidized
D-PZ13#3	0.073	1.60±0.17	1.77	1.78	0.93	0.12	Oxidized
H-PZ14#1	unknown	2.20±0.03	2.43	2.34	1.04	assumed to be 0	As-received
H-PZ14#2	0	0.17±0.06	0.19	0.65	0.29	0	Deoxidized
H-PZ14#3	0.061	1.35±0.17	1.50	1.65	0.84	0.11	Oxidized

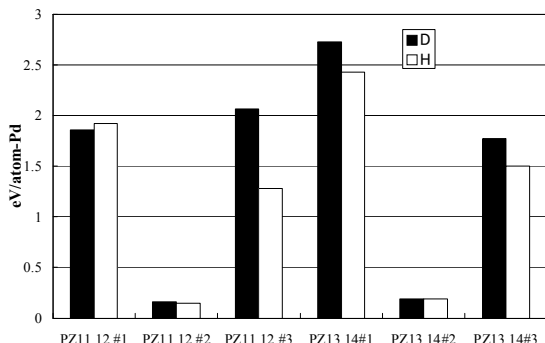


Fig. 3(a). E_1 in D(H)-PZ13,14#3

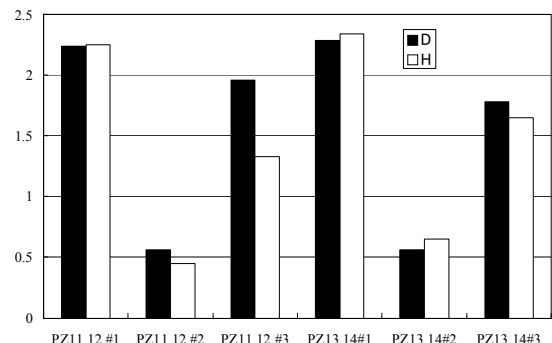


Fig. 3(b). D(H)/Pd in D(H)-PZ13,14#3

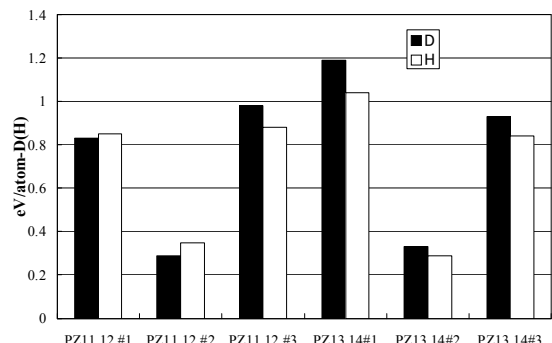


Fig. 3(c). $Q_{D(H)}$ in D(H)-PZ13,14#3

water formation energy xQ_{red} subtracted. These results show that the specific output power and the loading ratio both increase with oxygen content in/on the sample. Moreover, a similar tendency is seen for $Q_{D(H)}$. The averaged values of Q_D and Q_H for the #1 runs are 1.01 eV/D and 0.95 eV/H, respectively, and those for the #2 runs are 0.31 eV/D and 0.32 eV/H, respectively, while those for the #3 runs are 0.96 eV/D and 0.86

eV/H, respectively. It should be noted that the hydridation energy, $Q_{D(H)}$, in the #1 runs are almost the same as those in the #3 runs. This means that the fraction of oxygen atoms contributing to the high E_1 is rather small, since we know from the XRD spectra that the ratio of PdO to Pd is very large in the as-received samples. In other words, only oxygen atoms residing on/near the surface are playing the key role for the $Q_{D(H)}$ increase.

Sub-phases in the first phase

Paying attention to the time-dependent loading ratio, $L_{D(H)}(t)$, expressed as a function of pressure, $P(t)$, we notice a clear difference observed between the oxidized samples and the un-oxidized one as shown in Figs. 4(a) – (c). The 1a-phase, in which both D and H have the same $L_{D(H)}(t)$ - $P(t)$ characteristics, is observed only for the samples containing oxygen. On the other hand, the 1b-phase with the $L_{D(H)}(t)$ - $P(t)$ characteristics reflecting the isotope difference is observed in all samples. The latter is considered to be characteristic of bulk Pd, because such an isotope effect had been already observed in the hydrogen absorption experiments using bulk Pd samples [7]. Rapid absorption/adsorption and the generation of most fraction of the large heat output in the 1st phase are given in the 1a-phase. The 1a-phase is thought to be characteristic of the nano Pd, and is caused by existence of oxygen in/on the sample. A separate paper is provided for explaining this phenomenon by A. Takahashi [8].

η value

To quantitatively examine the exothermic

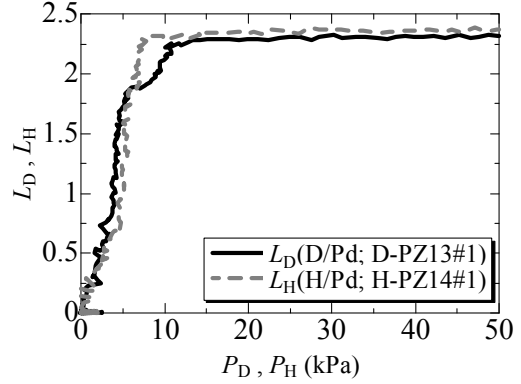


Fig. 4(a). Loading ratio, $L_{D(H)}$, expressed as a function of pressure, $P_{D(H)}$, in the runs D(H)-PZ13,14#3

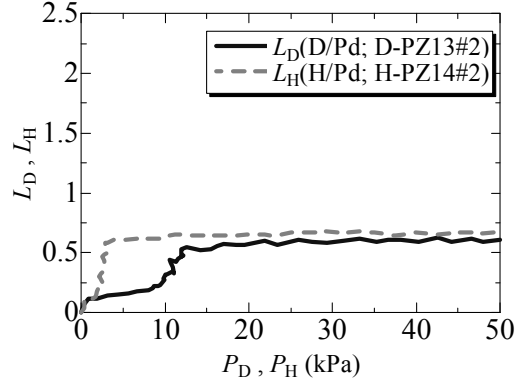


Fig. 4(b). Loading ratio, $L_{D(H)}$, expressed as a function of pressure, $P_{D(H)}$, in the runs D(H)-PZ13,14#2

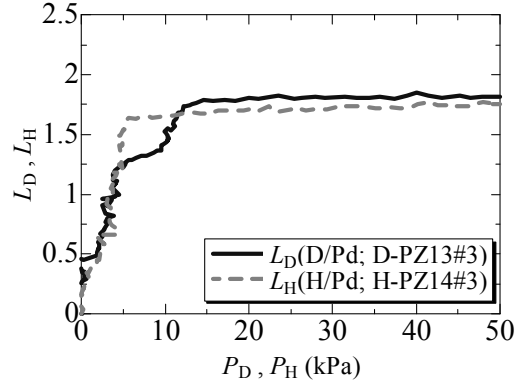


Fig. 4(c). Loading ratio, $L_{D(H)}$, expressed as a function of pressure, $P_{D(H)}$, in the runs D(H)-PZ13,14#3

process by sorption (both or either absorption

and/or adsorption) of the hydrogen isotopes, that changes momentarily in the 1a-phase, the time-resolved specific sorption energy, or the differential heat of hydrogen uptake, “ $\eta(t)$ ”, is defined as the energy released during the time interval Δt divided by the increased number of absorbed/adsorbed D(H) atoms during the same period;

$$\eta(t) \equiv \frac{\int_t^{t+\Delta t} W_{\text{true}}(t) dt}{L(t + \Delta t) - L(t)}, \quad (3)$$

where $L(t)$ is the time-resolved loading ratio. Here the true output power $W_{\text{true}}(t)$ is observed as an indicial response $W_{\text{means}}(t)$ with a delay time constant of τ . It is approximated here by the mean value of $W_{\text{means}}(t)$ during the time interval of τ . In addition, the mean value during the interval Δt is used also for $L(t)$, and Δt is equated with τ being equal to 5.2 min determined in the calibration run of calorimetry system.

$$\eta(t) \approx \frac{\int_t^{t+\Delta t} \overline{W(t, \tau)} dt}{L(t + \Delta t) - L(t)}, \quad (4)$$

where

$$\overline{W(t, \tau)} = \frac{\int_t^{t+\tau} W_{\text{means}}(t) dt}{\tau}. \quad (5)$$

Figures 5(a) – (c) shows the time-dependent heat output $W(t)$ and the time-dependent heat of sorption $\eta(t)$ in the runs PZ13(14)#1, PZ11(12)#2, and PZ13(14)#3. It should be noted that a large value of $\eta(t)$ of about 1.3 eV/D(H) greatly exceeding the bulk value of 0.3 eV/D(H) [9] is observed in the 1a-phase, though it is of the same level in the 1b-phase as the bulk value. Moreover, a rather large isotopic effect in η , $\eta_D/\eta_H \sim 1.2$, is

recognized in the 1a-phase. There was a slight indication that η_D/η_H in some instances goes up above 2 or more, although reproducibility should be confirmed. To clarify the phenomena taking

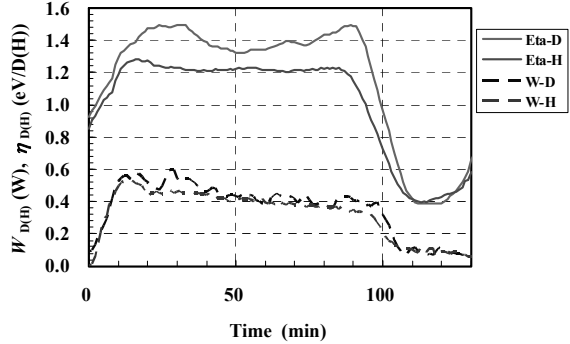


Fig. 5(a). Comparison of η in D(H)-PZ13,(14)#1

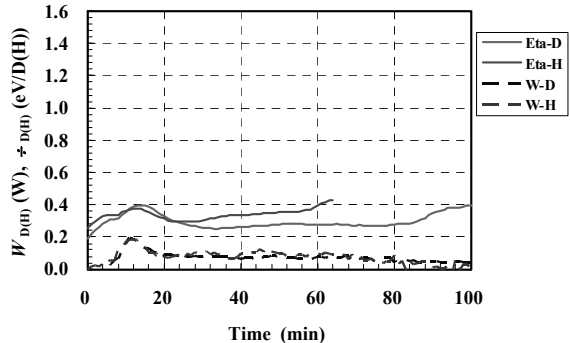


Fig. 5(b). Comparison of η in D(H)-PZ11,(12)#2

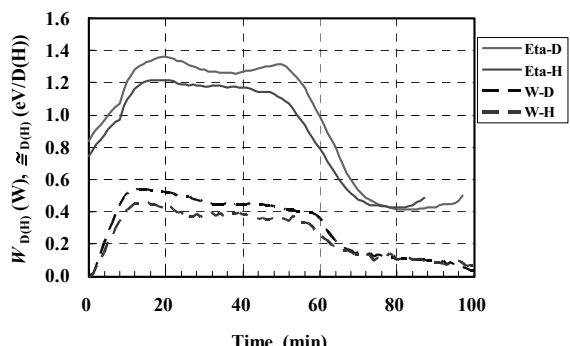


Fig. 5(c). Comparison of η in D(H)-PZ13,(14)#3

place in the 1a-phase is of the key issue not only from the CMNS point of view but also for the

nano-material science view-point.

4. Summary

The results obtained in the present study are summarized as follows.

- (1) The **as-received** sample has very large 1st-phase parameters; specific output energy $E_{1D(H)}$, the loading ratio D(H)/Pd, and the hydridation energy $Q_{D(H)}$.
- (2) The **de-oxidized** sample has given the significantly smaller 1st-phase parameters which are close to those for bulk Pd samples.
- (3) The **oxidized** sample has substantially recovered the large values of the 1st-phase parameters given for the virgin sample.
- (4) The 1st-phase is found to be divided into two sub-phases (1a and 1b). The 1a-phase was observed only for the as-received and the oxidized samples.
- (5) The **1a-phase** is characterized by rapid absorption/adsorption and high heat output. Most of the specific output power E_1 and the loading ratio D(H)/Pd can be observed in the 1a-phase. This phase is characteristic of nano particles, probably by the process occurring in the near-surface region. Oxygen incorporation is necessary for this 1a-phase to appear. The differential heat of sorption η_D is larger than η_H , several times in some instances, during the 1a-phase. It might be the indication of nuclear-origin heat release.
- (6) The **1b-phase** is characterized by a lower heat output nearly equal to the bulk-Pd value. The isotope effect in the 1b-phase is seen only in the relation between the pressure $P(t)$ and the loading ratio D(H)/Pd.

References

- [1] Y. Arata, *et al.*; The special report on research project for creation of new energy, J. High Temperature Society, No. 1. 2008.
- [2] T. Nohmi, Y. Sasaki, T. Yamaguchi, A. Taniike, A. Kitamura, A. Takahashi, R. Seto, and Y. Fujita: <http://www.ler-canr.org>; to be published in Proc. 14th Int. Conf. Condensed Matter Nuclear Science (ICCF14), Washington DC, 2008.
- [3] A. Kitamura, T. Nohmi, Y. Sasaki, A. Taniike, A. Takahashi, R. Seto and Y. Fujita; Anomalous effects in charging of Pd powders with high density hydrogen isotopes; *Phys. Lett. A* **373** (2009) 3109–3112.
- [4] Y. Sasaki, Y. Miyoshi, A. Taniike, A. Kitamura, A. Takahashi, R. Seto, and Y. Fujita: Proc. 10th Meeting of Japan CF-Research Society (2010) 14-19.
- [5] Y. Miyoshi, Y. Sasaki, A. Taniike, A. Kitamura, A. Takahashi, R. Seto, and Y. Fujita: Proc. 10th Meeting of Japan CF-Research Society (2010) 20-25.
- [6] A. Kitamura, Y. Sasaki, Y. Miyoshi, A. Taniike, A. Takahashi, R. Seto and Y. Fujita; Heat Evolution from Pd Nano-powders Exposed to High-pressure Hydrogen Isotopes and Associated Radiation Measurements; *J. Condensed Matter Nucl. Sci.* **4** (2011) 56-68.
- [7] Laesser, R., Klatt, K.-H.; *Phys. Rev. B*, **28** (1983) 748-758.
- [8] A. Takahashi, A. Kitamura, Y. Miyoshi, H. Sakoh, A. Taniike, R. Seto and Y. Fujita; paper JCF 11-5 in this meeting.
- [9] Fukai, K. Tanaka, and H. Uchida: *Hydrogen and Metals* (Uchida Rokakuho, Tokyo, 1998) [in Japanese]

Hydrogen isotope absorption/adsorption characteristics of Ni·Pd binary nano-particles

H. Sakoh¹, Y. Miyoshi¹, A. Taniike¹, A. Kitamura¹,
A. Takahashi², R. Seto², and Y. Fujita²

¹Graduate School of Maritime Sciences, Kobe University

Higashinada-ku, Kobe 6580022, Japan

²Technova Inc, Chiyoda-ku, Tokyo 1000011, Japan

Abstract. A twin absorption system has been used for experiments on D₂ and H₂ gas absorption of the oxide nano-composites of Pd, Ni and Zr. The sample powders used in the present work are Ni-Pd binary nanoparticles dispersed in ZrO₂ holder-flakes (PNZ2B) which were provided by B. Ahern. The observed loading ratio and the specific heat release in the first phase of as-received PNZ2B sample runs were both very large. The large heat release could include energy of oxygen pickup reaction as well as that of hydrogen isotope absorption. To investigate the effect of oxidation on absorption rate and heat release rate, we compared runs with the sample after forced deoxidization and the sample after forced oxidization to control oxygen amount. We have observed the time-dependent absorption energy per a D atom, η_D , showing sometimes much larger values than η_H , which could suggest existence of heat component of nuclear origin.

Keywords:Pd-Ni-Zr nano-powder, Deuterium absorption, D/Pd·Ni

1. Introduction

Arata and Zhang reported heat and ⁴He generation by deuterium (D) absorption in nano-sized Pd·Ni·Zr powders [1]. To investigate this phenomenon quantitatively, we constructed a twin absorption system for D₂ or H₂ gas absorption which can make mass-flow-calorimetry [2]. We used commercially available samples and those supplied by Santoku Corporation [3,4].

On the other hand, B. Ahern (B.A.) fabricated his own samples and measured temperature and pressure during gas absorption experiment. He reported very large loading ratio of hydrogen and heat evolution [5]. We offered him to examine the heat release and absorption characteristics with our twin-absorption system. This report describes the results of time-dependent measurements of hydrogen isotope gas absorption / adsorption and associated heat evolution from the Pd·Ni·Zr oxide nano-compounds supplied by B.A.

2. Experimental apparatus

Composition of the PNZ2B sample is Pd

(4%), Ni (29%) and Zr (67%). We used a twin absorption system consisting of two equivalent chambers for hydrogen isotope gas absorption / adsorption experiments, one of which is shown schematically in Fig. 1. Pd nano-particles are put in the reaction chamber, and the outer chamber is evacuated for thermal insulation during hydrogen isotope absorption / adsorption. The reservoir tank is filled with D₂ (H₂) gas at a pressure of 0.4 MPa, typically, before an absorption run starts. The flow rate of D₂ (or H₂) gas is adjusted and regulated with a "Super Needle" valve.

Sheath heaters with resistance of 110.0 Ω in A1 and 36.1 Ω in A2 are used for sample baking,

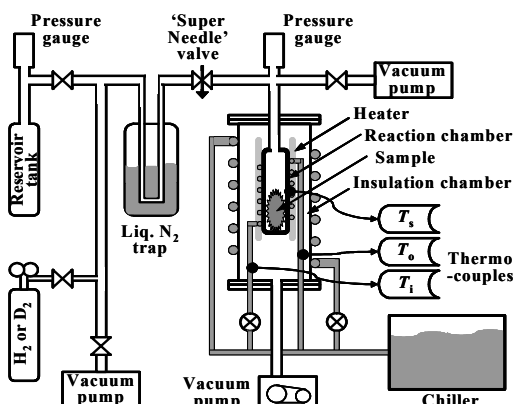


Fig. 1. Schematic of one-part of the twin system.

and also for sample heating in the cases of forced deoxidization and forced oxidization. Alumel-chromel thermo-couples are used to measure temperatures.

For calorimetry, the coolant water is maintained constant (± 0.1 °C) at near-room temperature with a chiller, and the flow rate is controlled with a digital coolant transmitter at a rate of 6 cc/min, which recovers heat with an efficiency of 63.1 ± 5.8 %. There is a delay in the response of the temperature difference due to the initial response with a time constant of 5.2 minutes. Calorific power is calculated from temperature difference between the exit and the entrance of water-coolant. The calibrated conversion factor is 0.67 W/K.

3. Experimental procedure

Figure 2 shows the experimental procedure. The run number expresses the conditions of the sample used in the run, using the letters defined in Table 1. The as-received sample is baked at 440 K for 2 hours in vacuum, and subjected to the D₂ (H₂) absorption run (#1 run). The sample is reused either without any treatment (A or B run) or after the specified treatment; forced deoxidization (#2 run) or forced oxidization (#3 run).

In the case of forced deoxidization, the sample is heated after filling the reaction chamber with the hydrogen isotope gas at a pressure of 0.3 MPa, and kept at 570 K for 24 hours. On the other hand, in the case of forced oxidization, the sample is treated in the similar manner using oxygen gas at a pressure of 0.4 MPa kept at 470 K or 570 K for 30 hours. The fraction of oxidized atoms, PdO and NiO, is calculated from the

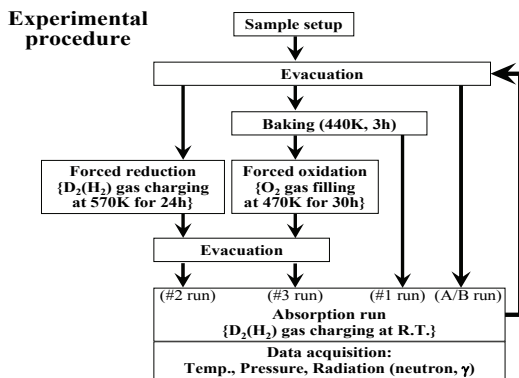


Fig.2. Flow-chart of the experimental procedure.

Table 1. Nomenclature for the run number.

#1	absorption run using a virgin sample
#2	absorption run after forced de-oxidization
#3	absorption run after forced oxidization
#nA	absorption run following #n without baking
#nB	absorption run following #nA without baking
#n(N)d	desorption run by evacuation after the absorption run #n(N)

pressure drop during this procedure.

In the #3 run of the oxidized sample, the released heat includes energy of oxygen pickup reaction, Q_{red} eV/atom-O, and that of hydrogen isotope absorption / adsorption, the 'hydridation' energy, $Q_{\text{D(H)}}$ eV/atom-D(H);

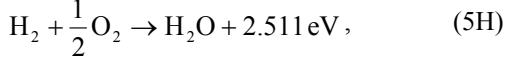
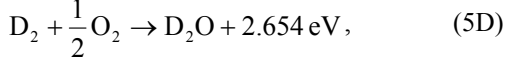
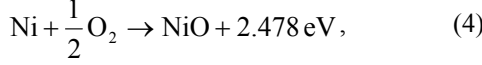
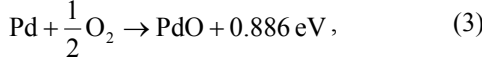
$$\text{Pd}(\text{Ni})\text{O}_x + \left(x + \frac{y}{2}\right)\text{D}_2 = x\text{D}_2\text{O} + \text{Pd}(\text{Ni})\text{D}_y, \\ + xQ_{\text{red}} + yQ_{\text{D}}$$

$$\text{Pd}(\text{Ni})\text{O}_x + \left(x + \frac{y}{2}\right)\text{H}_2 = x\text{H}_2\text{O} + \text{Pd}(\text{Ni})\text{H}_y, \\ + xQ_{\text{red}} + yQ_{\text{H}} \quad (1\text{D},1\text{H})$$

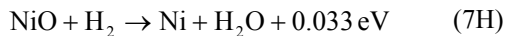
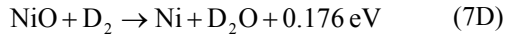
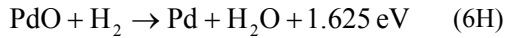
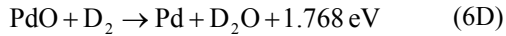
where x is the fraction of Pd (Ni) atoms oxidized, and y is the fraction of Pd (Ni) atoms hydrided. The total energy released is expressed as E_1 ;

$$E_1 = xQ_{\text{red}} + yQ_{\text{D(H)}} \quad (2)$$

The energies of formation of oxides associated in the present phenomena are as follows;



The energies of the oxygen pickup reactions, Q_{red} , are calculated by combining the above equations;



The energies of the oxygen pickup reactions for PdO, Eqs. (6D) and (6H), are much larger than those for NiO, eqs. (7D) and (7H).

We use Eq. (2) to know the value of $Q_{\text{D(H)}}$ by subtracting the first term xQ_{red} from the experimentally obtained value of E_1 . However, we don't know the fractions of PdO and NiO. The purpose of the present study is to show that $Q_{\text{D(H)}}$ is much larger than the value obtained so far for the bulk samples. Therefore, underestimation of Q_{red} must be avoided not to overestimate $Q_{\text{D(H)}}$. We then assumed here that there were no NiO having the smaller Q_{red} , and that $Q_{\text{red}} = 1.77 \text{ eV}$ for D₂ and $Q_{\text{red}} = 1.63 \text{ eV}$ for H₂ for conservative estimation.

4. Results of experiments

Figure 3 shows typical variation of the heat output, W_D and W_H , pressure in the reaction chamber, P_D and P_H , and the loading ratio, L_D and L_H , in the hydrogen isotope absorption run for as-received samples, PNZ2B1 and PNZ2B2. The maximum output powers of 0.4 W and 0.2 W,

respectively, are modest, but the heat release lasts for more than 1000 minutes.

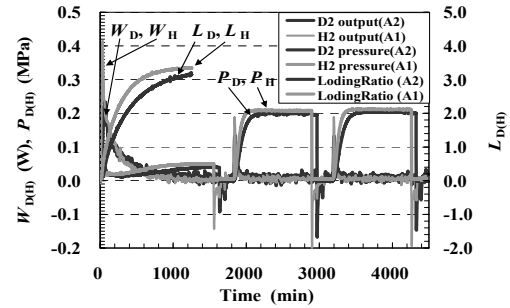


Fig. 3. Evolution of heat, pressure in the reaction chamber after introduction of D₂ (or H₂) gas and the time-dependent loading ratio (H-PNZ2B1#1 and D-PNZ2B2#1).

The samples show peculiar pressure changes in the early stage of the #1 run. Figure 4 shows the relation between the pressure and the loading ratio for the PNZ2B1 and PNZ2B2 samples. The gas absorption / adsorption does not start until the pressure is increased to some value. This behavior of the pressure was never observed for samples containing no NiO [4].

It seems to suggest the following mechanism: The surface NiO layer is relatively hard to deoxidize. However, once the deoxidization reaction (7D) or (7H) is initiated at a point to expose metallic Ni to D₂ / H₂ atmosphere, rapid dissociation to D / H atoms and adsorption followed by rushing into the bulk begin at the pit.

The finally saturated value of the loading

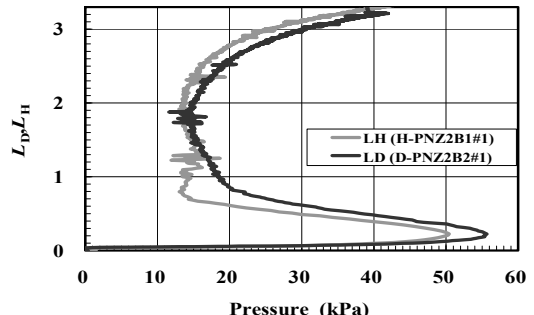


Fig. 4. Relation between the loading ratio and the pressure for the PNZ2B sample.

ratio, $D(H)/[Pd\cdot Ni]$, is extraordinarily large; 3.3 both for D and H absorption. The specific heat release, $E_1 \approx 2.0$ (1.8) eV/atom-[Pd·Ni], in the first phase of the as-received PNZ2B1 and PNZ2B2 runs is also very large. These values of E_1 are divided by the final values of the loading ratio to give tentative value of the hydridation energy, $Q_{D(H)} \approx 0.55$ (0.50) eV/atom-D(H). This is tentative because the energy of oxygen pickup is not subtracted from E_1 , since the oxidization fraction x is not known.

After finishing the #1 run, we evacuated the reaction chamber and made absorption runs without baking beforehand, which we call the #1A, and #1B runs. The final loading ratio was about 0.3 with the first-phase duration of about 120 minutes both in the #1A and the #1B. The first-phase energy E_1 as well as the above value of the loading ratio is smaller than those in the #1 run. However, the tentative values of $Q_{D(H)}$ are of the same order of magnitude as those in the #1 run.

After finishing the #1B run, we made forced deoxidization at 573 K. Figure 5 shows the #2 absorption runs using these samples. The first-phase duration is about 500 minutes, with peaks of power being 0.2 W for the H-run and 0.3 W for the D-run. In contrast to the #1 run, the pressure

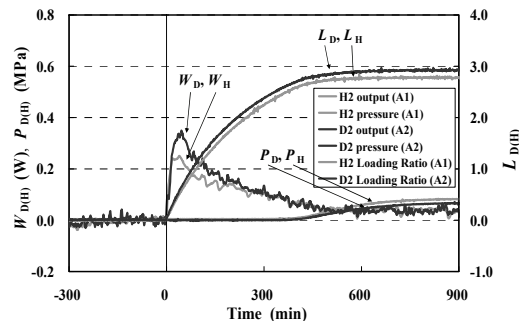


Fig. 5. The run after forced deoxidization

does not show the peculiar change. The values of $D(H)/[Pd\cdot Ni]$, E_1 and $Q_{D(H)}$ exceeded 2.0 (2.0), 1.5 eV/atom-[Pd·Ni] and 0.5 eV/atom-D(H), respectively, which are astonishingly large compared with those using the de-oxidized PZ samples [4,6].

The forced oxidization of the samples was performed by keeping them in the O_2 atmosphere at a temperature of 470 K or 570 K for 30 hours. The degree of oxidization, x , is calculated from the pressure difference between the beginning (0.3 MPa) and the end of the exposure to O_2 in the closed system. The values of x ranged from 0.000767 to 0.000732 in 470 K operation, and from 0.000921 to 0.000917 in 570 K operation.

Figure 6 shows the traces in the #3 absorption runs using the oxidized samples. We first notice that the peculiar pressure change observed in the #1 run has appeared again in the early stage of the first phase lasting for 500 minutes. The oxidized samples has almost recovered the large values of E_1 , $D(H)/[Pd\cdot Ni]$ and $Q_{D(H)}$ of the as-received samples. There is recognized a trace of endothermic variation of the output power at the beginning of the deuterium run. However, the reproducibility of this variation should be examined.

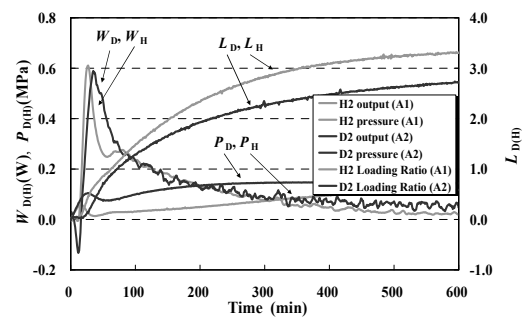


Fig. 6. The absorption run after forced oxidation (H-PNZ2B3#3 and D-PNZ2B4#3)

We reused the PNZ2B samples; the mixture of the PNZ2B1 and the PNZ2B3 samples is the PNZ2B5, while the PNZ2B2 and PNZ2B4 sample mixture is the PNZ2B6. Figure 7 shows the #1 absorption run of the reuse samples. The absorption parameters are $D(H)/[Pd\cdot Ni] \approx 2.0$ (2.0), $E_1 \approx 1.7$ (1.3) eV/atom-[Pd\cdot Ni], and $Q_{D(H)} \approx 0.60$ (0.50)eV/atom-D(H). The #2 and #3 runs of the reused samples also showed that $D(H)/[Pd\cdot Ni]$, E_1 and $Q_{D(H)}$ are of the same order of magnitude as those in the #1 run.

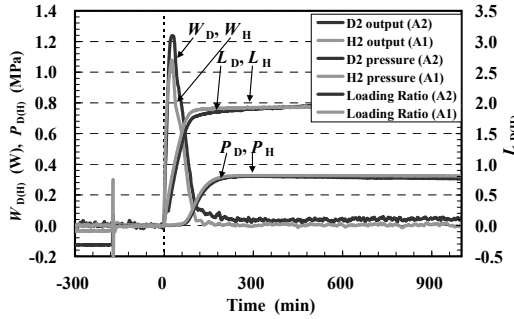


Fig. 7. Runs for the reused sample (H-PNZ2B5#1 and D-PNZ2B6#1).

Figures 8, 9 and 10 show the parameters E_1 , $D(H)/[Pd\cdot Ni]$ and $Q_{D(H)}$ as histograms. The first-phase specific energy E_1 for deuterium is larger than that for hydrogen. The hydridation energy Q_D for deuterium is also greater than that for hydrogen. The ratio Q_D/Q_H is almost constant in the runs using PNZ2B1 through PNZ2B4, and the averaged value is about 1.22 ± 0.13 , which appears to be a little larger than that expected for a chemical isotope effect.

Next, we discuss time resolved parameters. The time-resolved specific sorption energy, or differential heat of hydrogen uptake, $\eta_{D(H)}$, defined as the output energy per one hydrogen isotope atom absorbed/adsorbed [4,6], are shown in Fig. 11 together with the heat evolution in the PNZ2B3#1 and PNZ2B4#1 runs. We notice that

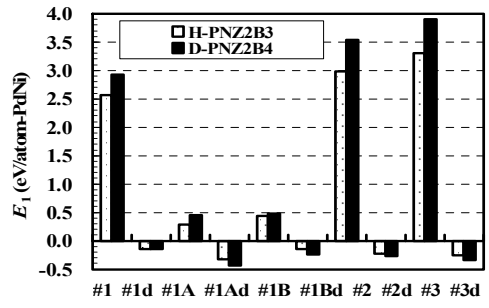


Fig. 8. E_1 for the samples H-PNZ2B3 and D-PNZ2B4.

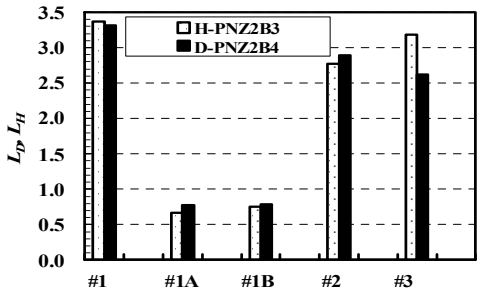


Fig. 9. $D(H)/[Pd\cdot Ni]$ for the samples H-PNZ2B3 and D-PNZ2B4.

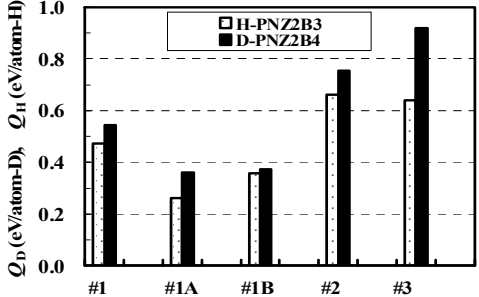


Fig. 10. Hydrydation energy, $Q_{D(H)}$, for the samples PNZ2B3, and PNZ2B4.

η_D (η_H) is relatively constant in contrast to the PZ samples whose first phase is divided into 1a and 1b phases [4,6]. The averaged value is 0.53 (0.47) for the first phase of these runs, which is averaged again over all runs to give $\bar{\eta}_{D(H)} = 0.60$ (0.53). In every cases of #1, #2 and #3 runs, the averaged value of η_D is larger than that of η_H , and these values are rather modest compared with those for the PZ samples.

Figure 12 shows the ratio of η_D to η_H . The value of η_D/η_H in the early stage of the first phase

is about 1.5, and is significantly larger than the ratio $\bar{\eta}_D/\bar{\eta}_H = 1.12 \pm 0.16$ using the averaged values mentioned above. This is one of the reason why Q_D/Q_H is a little larger than $\bar{\eta}_D/\bar{\eta}_H$, since the early stage heat evolution has larger weight in

calculating the former. This might indicate that some nuclear effects including nuclear reactions could contribute to the heat evolution in the early stage of PNZ2B4#1 run.

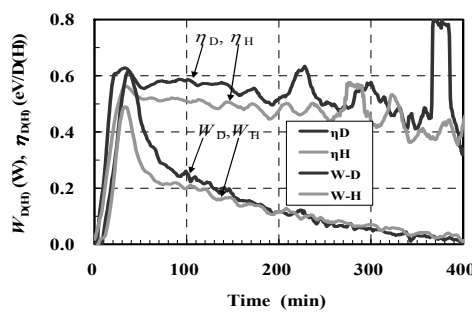


Fig. 11. Evolution of heat, W , and the time-dependent absorption energy, η , for D_2 gas and H_2 gas(H-PNZ2B3#1 and D-PNZ2B4#1).

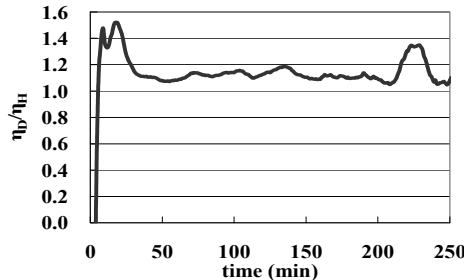


Fig. 12. Comparison of η_D with η_H .

5. conclusion

The PNZ2B sample, the $Pd(0.04)Ni(0.29)Zr(0.67)$ oxide composite, has unique properties, and the results of the absorption experiments are summarized as follows;

- (1) Observed loading ratio, $D(H)/[Pd\cdot Ni] \approx 3.0$, and specific heat release, $E_1 \approx 2.0$ eV/atom-[Pd-Ni], in the first phase of the absorption runs

using as-received PNZ2B samples are both very large.

(2) It is deduced that Ni as well as Pd contributes to the first phase heat by hydrogen isotope absorption / adsorption at room temperature. It is inferred that the Pd atoms act as a catalyst for the hydrogen isotope absorption / adsorption of Ni.

(3) The hydridation energy $Q_{D(H)} \approx 0.60(0.49)$ eV/atom-D(H) is about twice as large as that for the bulk Pd [7], and Q_D/Q_H is about 1.22 ± 0.13 , which appears to be suggesting the existence of heat component of nuclear origin.

(4) For samples after forced oxidization the loading ratio and the heat release were as large as those for the as-received samples. This result is similar to those for the #1 and #3 runs of the PZ samples [4,6].

(5) The PNZ2B samples, however, showed that heat release of the #2 run after the forced deoxidization is as large as that of the #1 run.

(6) The PNZ2B samples show anomalous change of gas pressure in the beginning of the first phase.

(7) There is no sub-phase transition, 1a / 1b. The time dependent sorption energy, $\eta_{D(H)}$, is rather constant, and averaging over the first phase gives 0.60 (0.53) eV/atom-D(H).

REFERENCES

- [1] Y. Arata and Y. Zhang; The special report on research project for creation of new energy; J. High Temperature Society, 2008, No. 1.
- [2] A. Kitamura, T. Nohmi, Y. Sasaki, A. Taniike, A. Takahashi, R. Seto and Y. Fujita; Anomalous effects in charging of Pd powders with high density hydrogen isotopes; Phys. Lett. A **373** (2009) 3109–3112.
- [3] A. Kitamura, Y. Sasaki, Y. Miyoshi, A. Taniike, A. Takahashi, R. Seto and Y. Fujita; Heat Evolution from Pd Nano-powders Exposed to High-pressure Hydrogen Isotopes and Associated Radiation Measurements; J. Condensed Matter Nucl. Sci. **4** (2011) 56-68.

- [4] A. Kitamura, Y. Miyoshi, H. Sakoh, A. Taniike, A. Takahashi, R. Seto and Y. Fujita; Time resolved measurements of loading ratios and heat evolution in D₂ (and H₂)-Pd-Zr mixed oxide systems; to be published in J. Condensed Matter Nucl. Sci.
- [5] B. Ahern; Private communication.
- [6] Y. Miyoshi, H. Sakoh, A. Kitamura, A. Taniike, T. Takahashi R. Seto and Y. Fujita; Hydrogen Isotope Absorption / Adsorption Characteristics of Pd-Zr Oxide Compounds; paper JCF11-3 in this meeting.
- [7] F. Fukai, K. Tanaka, and H. Utida; Hydrogen and Metals (Utida Roukakuho, Tokyo, 2002.p115)

Search for Nuclear Phenomena in Deuterium Irradiation to Nano-Structured Metal under Glow Discharge

H.Ougida*, H.Sasaki, A.Tamura, S.Narita, H.Yamada

Department of Electrical Engineering and Computer Science, Iwate University
Morioka, Iwate, 020-8551

[*t2310004@iwate-u.ac.jp](mailto:t2310004@iwate-u.ac.jp)

ABSTRACT

It has been reported that the selective transmutation (e.g. ^{133}Cs to ^{141}Pr) occurred in deuterium permeation with Pd/CaO multi-layered sample. Also, anomalous heat evolution and ^4He generation were observed in deuterium absorption and desorption with the nano-structured metal sample. Considering such experimental results, we have performed the discharge experiment in deuterium atmosphere using nano-structured film cathode such as Pd/CaO multi-layered sample and Pd membrane deposited onto Cu foil. As the results, we observed possible particle emission and possibly newly produced elements on the cathode in the elemental analysis by TOF-SIMS.

Keywords : Glow discharge, Multi-layered sample, Pd/Cu, Selective transmutation, CR-39

1. Introduction

We have performed the discharge experiment in deuterium atmosphere, and observed transmutation and particle emission. It is suggested that the low energy nuclear reaction (LENR) can occur on the surface of the cathode metal by irradiating deuterium atoms with electric field. Besides the discharge method, it is well known that the selective nuclear transformation (e.g. ^{133}Cs to ^{141}Pr) can be induced by permeation of deuterium through multi-layered thin Pd/CaO films [1]. In addition, it has been recently claimed that the LENR can be induced effectively in the deuterium absorption and desorption for the nano-size Pd particles [2]. These results suggest that the properties of nano-structured metal help the trigger efficiency of LENR enhance and it is important to understand the deuterium behavior in such materials for clarifying the mechanism of LENR. In this study, we conducted the DC glow discharge in deuterium atmosphere using nano-structured film cathode, and searched for the nuclear phenomena.

In this study, we have performed discharge experiment using two types of sample; the Cs deposited Pd/CaO sample and Pd membrane deposited onto Cu foil in cathode. Then, we investigated the nuclear phenomenon such as the selective nuclear transformation observed by MHI experiment (e.g. ^{133}Cs to ^{141}Pr), charged particle

emission, and search for nuclear products.

2. Experiment

2.1 Sample preparation

The structure of samples in this experiment is shown in Fig.1. The samples were prepared by the following procedure.

(i) Sample-1: Cs deposited multi-layered Pd/CaO

The Pd foil with the size of 10 mm x 10 mm x 0.1 mm and the purity of 99.95% was washed by acetone for 20 minutes, and the ultrasonic cleansing was done with ultra pure water for 20 minutes. Afterwards, to make the crystallographic structure uniform, the sample was annealed for 10 hours at 900°C. Then, it was washed by aqua regia to remove metallic impurities and the ultrasonic cleaning was done with ultra pure water for 20 minutes. The layers of 40 nm Pd, 5 nm CaO and 40 nm Pd were deposited to the surface of the Pd foil with Ar beam sputtering. Then, cesium was deposited to the sample by the electrochemical method with Cs_2CO_3 solution. Finally, 60 nm Pd layer was deposited. The aim of putting the outermost Pd layer was to prevent cesium deposited flown away by the sputtering effect.

(ii) Sample-2: Pd membrane deposited on Cu foil

The Cu foil with the size of 10 mm x 10 mm x

0.1 mm and the purity of 99.95% was washed by acetone for 20 minutes, and the ultrasonic cleansing was done with ultra pure water for 20 minutes. Afterwards, the sample was annealed for 10 hours at 900°C. Then, it was washed by aqua regia to remove metallic impurities and the ultrasonic cleaning was done with ultra pure water for 20 minutes. Pd membrane was deposited to the surface of Cu foil. Thickness of Pd foil is ~500 nm. Since the hydrogen solubility and the diffusion coefficient of Cu are smaller comparing to that of Pd, the deuterium atoms irradiated to the cathode concentrate in the Pd layer.

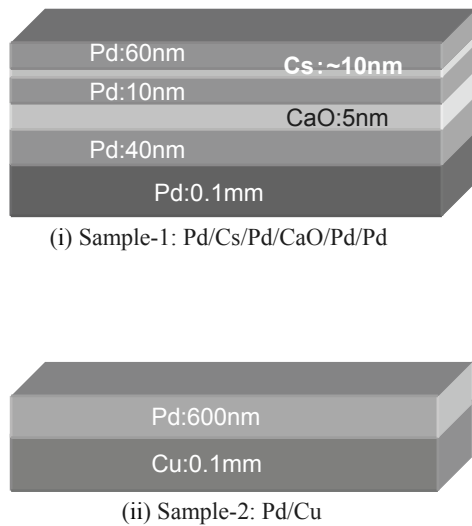


Figure 1. Sample Structure

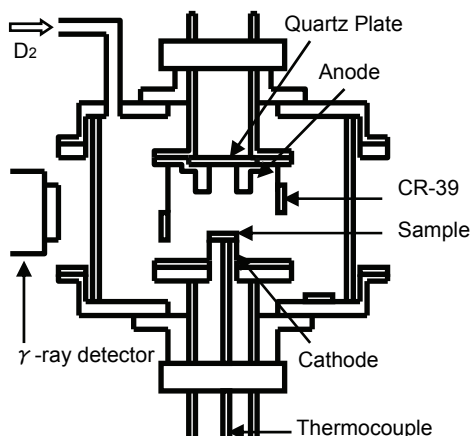


Figure 2. Discharge Cell

2.2 Discharge experiment

Figure 2 shows the discharge cell used in this experiment. The anode and the cathode support are made of the stainless steel (SUS304). The side surface is covered with quartz cylinder, so we can easily observe discharge condition. Four pieces CR-39 were placed surrounding the cathode sample to aim at detecting charged particles. The detection area for each piece was 1 x 1 cm². In addition, we placed CR-39 at the bottom of the cell for the reference. We used an NaI(Tl) scintillation counter to detect γ -rays and a thermocouple to measure the sample temperature.

After setting the sample on the cathode and sealing off the cell, we evacuated the cell to 10⁻³ Torr, and supplied deuterium gas until the inside pressure became ~1 Torr. Then, we applied DC voltage and expose the sample to the discharge. For both type of samples, the Pd membrane faced on the discharge. The discharge continued for three hours. We tried to detect possibly emitted prompt γ -rays from nuclear reactions. In addition, it is possible to emit γ -rays if short-lived radioisotopes were produced during experiment. In order to identify such radioisotopes, the γ -ray measurement was kept conducting for two hours after the discharge. Then, the sample was taken out from the cell and the newly produced elements were analyzed by TOF-SIMS.

CR-39 is a kind of plastic detector and the track pit made along the trajectory of a charged particle appears after chemical etching. The charged particle detection can be a direct evidence of the occurrence of nuclear reaction. The etching conditions for this study were of 5 N NaOH solutions at 70 °C for 8 hours. After etching, we surveyed the surface of the CR-39 with the digital microscope to observe the pit tracks. The energy of charged particles can be estimated according to the diameter with assumption of particle type.

TOF-SIMS (ULVAC-PHI PHI TRIFT V nanoTOF) was used to examine the foreign (nuclear?) products. The Bi⁺ beam was utilized as primary bombarding ions and 40 x 40 μm^2 area was analyzed on the sample. In prior to the data acquisition, the contaminants on the most surface were removed by the sputtering for 10 s.

We also performed discharge experiment in nitrogen atmosphere as a blank run to be compared with the possible anomalous events for deuterium discharge run. We prepared another “Blank” sample which was not exposed to discharge for the reference in the elemental analysis.

3. Results and Discussions

3.1 Charged particle measurement

Figure 3 shows the number of tracks recorded on four pieces of CR-39 in the cell for each sample condition. The closed and open symbols show the results in the D₂ and the N₂ discharge, respectively. Note that the number of tracks here is totals in four pieces CR-39 set in the cell.

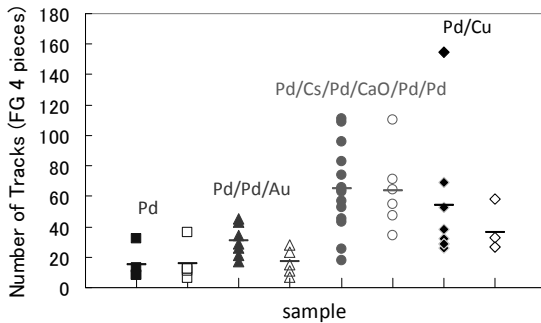


Figure 3. Number of tracks recorded on CR-39. Blank points ($\square, \triangle, \circ, \diamond$) stand for N₂ discharge.

In comparison to the results of the previous experiments using Pd foil and Pd/Pd/Au foil [3], the sample-1 shows significant number of tracks in both D₂ discharge and N₂ discharge. On the other hand, the sample-2 shows that the averaged number of tracks in D₂ discharge is more than that in N₂ discharge. These results may indicate effectiveness to charged particle emission of the nano-structured membrane sample.

Figure 4 shows the total number of tracks on four pieces of CR-39. The averaged number is 16.0 /cm² for D₂ discharge and 15.9 /cm² for N₂ discharge, respectively. Considering these values and the standard deviation of each distribution, we regarded the events with the number of tracks above 31/cm² as anomalous ones, which were regarded to be observed for 5 cases out of 14 total runs.

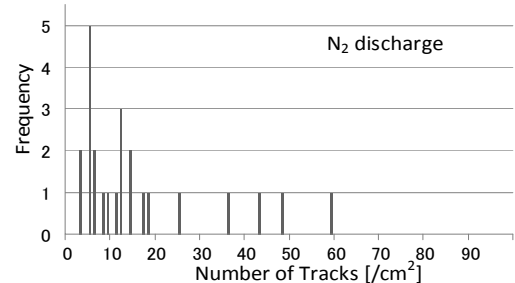
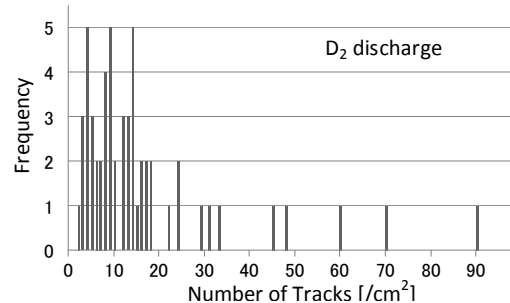


Figure 4. Number of tracks on CR-39 for D₂ discharge (top) and N₂ discharge (bottom).

Figure 5 shows the track-diameter distribution data of such runs. For comparison, the diameter of tracks recorded in N₂ discharge is also shown in the figure.

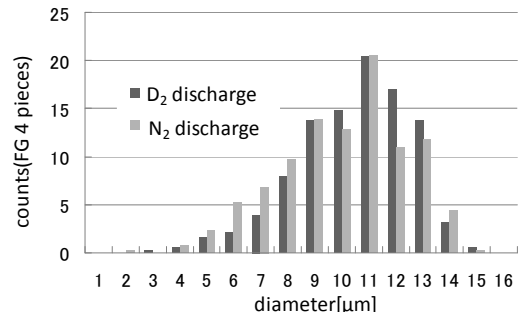


Figure 5. Track-diameter distribution for the events with significant number of tracks. The diameters for the tracks recorded in N₂ discharge are also shown.

The averaged diameters of D₂ and N₂ discharge were 11.0 μm and 10.6 μm, respectively. No clear difference was observed between these two distributions.

Figure 6 shows the total number of tracks on four pieces of CR-39. The averaged number is 13.0 /cm² for D₂ discharge and 9.1 /cm² for N₂ discharge, respectively. Considering these values and the standard deviation of each distribution, we regarded the events with the number of tracks above 14/cm² as anomalous ones, which were observed 4 cases out of 8 total runs).

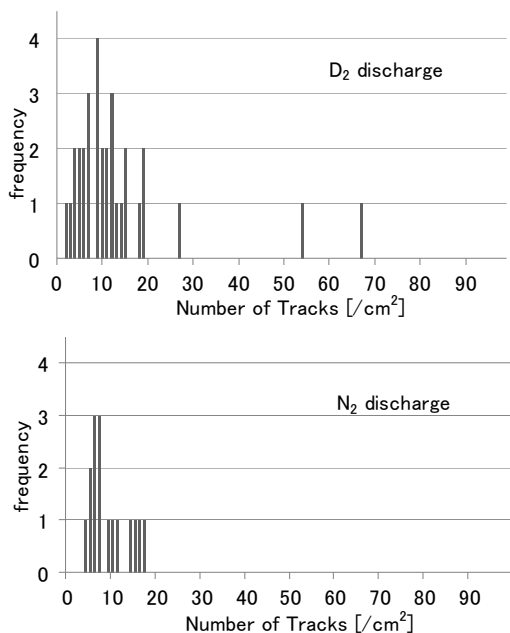


Figure 6. Number of tracks on CR-39 for D₂ discharge (top) and N₂ discharge (bottom).

Figure 7 shows the track-diameter distribution of such runs. For comparison, the diameter-data of tracks recorded in N₂ discharge are also shown in the figure.

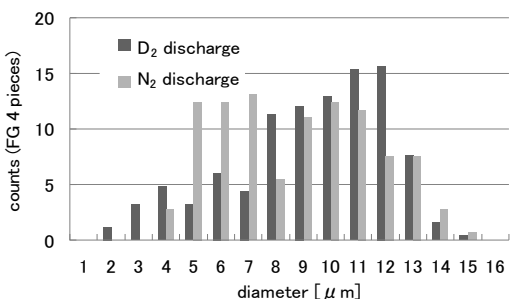


Figure 7. Diameter distribution for the events with significant number of tracks. The diameters for the tracks recorded in N₂ discharge are also shown.

It is shown that the diameter distribution is different between D₂ discharge (excess) and N₂ discharge (total). The peak around 11-12 μm stands out in the distribution for D₂ discharge. These differences suggest the possibility of the charged particle emission in the D₂ discharge.

3.2 Elemental analysis

(i) Sample-1 : Cs deposited Pd/CaO sample

In order to investigate the selective transmutation from ¹³³Cs, we looked at the signal

on mass 137 and 141 in the mass spectrum measured in TOF-SIMS analysis. Figure 8 shows the spectra around mass 141 for the sample subjected to D₂ and N₂ discharge

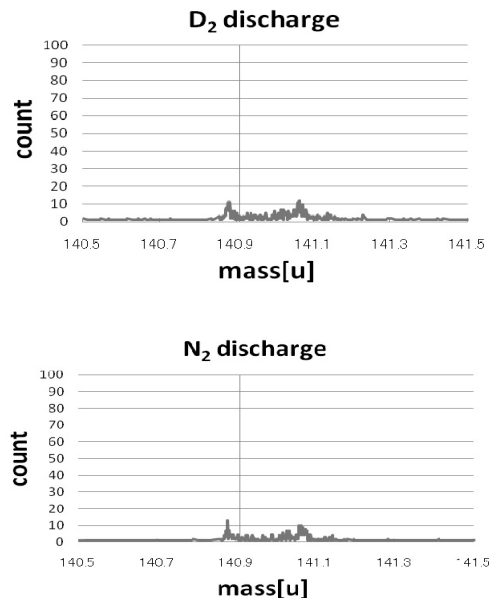


Figure 8. TOF-SIMS spectra of the mass around 141 for the sample exposed to D₂ (top) and N₂ (bottom) discharges.

No significant signals at mass 140.9 were found on D₂ or N₂ discharge, so that the production of ¹⁴¹Pr was not confirmed in this experiment. We did not find the signal on the elements with mass 137 either.

Now we think about the reasons why the transmutation was not observed in this experiment. There are possibly at least two reasons.

One reason may be insufficient deuterium flux irradiated to the sample in the discharge. Iwamura has shown that the conversion efficiency of ¹³³Cs to ¹⁴¹Pr was approximately 30 % when the amounts of deuterium by 3×10^{23} were permeated through his Pd/CaO multi layered sample [7]. If the amount of the current is 1mA, irradiation area is 1 cm², and deuterium take on the flowing current, we assume that the amount of deuterium irradiation in this study is $\sim 10^{20} / \text{cm}^2$. Assuming that permeation and irradiation is the same condition, deuterium irradiation rate in this study can't be high enough.

Another reason may be that the sample used in this experiment does not have a proper structure for inducing the transmutation effectively. It has been reported that, in the permeation experiment

with multi-layered Pd/CaO, ^{141}Pr was found to make peak at 10 nm deep layer from the surface [7]. In comparison, we deposited Pd 60 nm layer above Cs-contained layer. Even if the transmutation were occurred in the region specified in the permeation experiment, the products could not be detected. Otherwise, it is possible that the products on the cathode were diffused by sputtering in the discharge, so that they could be flown away.

(ii)Pd/Cu sample

The possible transmutation products were surveyed by qualitative analysis. The mass numbers and the corresponding elements observed in the TOF-SIMS analysis are shown in Table 1. The signal intensity is more than twice of that for the sample subjected to N_2 discharge or the “Blank” sample which was not exposed to the discharge.

sample number	elements corresponding to mass
1	64(Ni,Zn),94(Zr,Mo),
2	97(Mo)
3	64(Ni,Zn),119Sn
4	18(O),64(Ni,Zn),94(Zr,Mo)
5	(no outstanding signal)
6	(no outstanding signal)
7	16(O),18(O),
8	14(N),77(Se),94(Zr,Mo),119(Sn)

Table 1 Foreign elements identified by TOF-SIMS

In the past experiments, we often observed the anomalous signals in the mass region of 50-70. Then, we pay attention to the signal with mass 64 (Ni or Zn), here.

Figure 9 shows the spectra around mass 64.

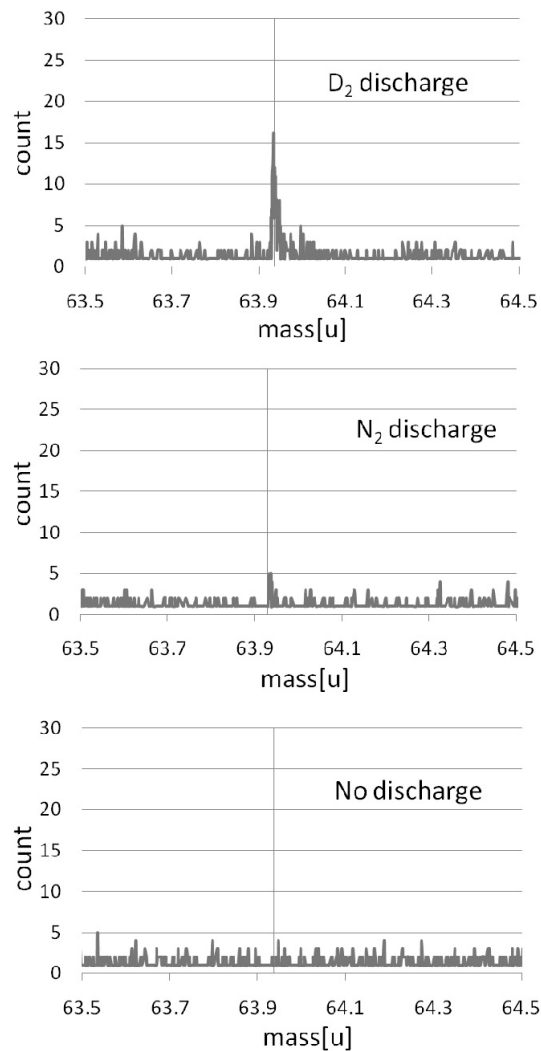


Figure 9. TOF-SIMS spectra of the mass around 64 for the sample exposed to D_2 discharge (top), N_2 discharge (middle), and blank sample (bottom).

We found that the signal intensity for the D_2 discharge sample was more than three times as that for N_2 discharge sample or blank sample. The signal observed for D_2 discharge sample may indicate transmutation products. The possible nuclear products and the detection frequency for each type of sample are summarized in Fig.10. In the figure, the results of our past experiments using Pd/Pd/Au sample are also shown. For the sample Pd/Cu and Pd/Pd/Au, the elements of mass 50-70 are likely to be detected. Although the systematic study is still necessary, such tendency is also shown in the present experiment, so far.

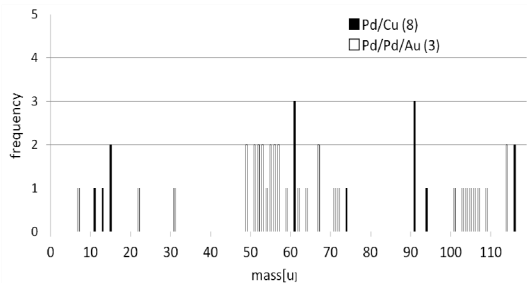


Figure 10. The mass number identified as possible transmutation products for the sample Pd/Cu and Pd/Pd/Au.

4. Conclusion

In this study, we have performed discharge experiment using the Cs deposited Pd/CaO sample and Pd membrane deposited onto Cu foil in cathode. Then, we investigated the nuclear phenomenon such as the selective nuclear transmutation observed by MHI experiment (e.g. ^{133}Cs to ^{141}Pr) and charged particle emission. We have not confirmed the selective transmutation. In the discharge with the sample of Pd membrane deposited onto Cu foil, various candidates of possible nuclear products were found.

We need to confirm the results of elemental analysis by using other methods than TOF-SIMS. Moreover, it is quite interesting to investigate the correlation between variety of the foreign elements detected and the sample type. Such systematic study may bring us progress in understanding the mechanism of low-energy transmutation reactions, if any, in condensed matter.

Reference

1. Y. Iwamura, et al. : JJAP, 41(2002)4642
2. Y.Arata,et al.JJAP, Vol.38,No.7A(1999)L774
3. H. Sasaki, et al. Proc. of JCF10 (2010) 33.
4. A. Arapi et al., Jpn. J. Appl. Phys. (2002) L1181.
5. S. Narita et al., Proc. of JCF5 (2004) 14.
6. S. Narita et al., Proc. of ICCF12 (2006) 188.
7. S. Narita et al., Proc. of JCF6 (2005) 43.
8. Y. Iwamura, et al :Proc. ICCF10, see Ref-3

Search for Nuclear Phenomena in Deuterium Desorption Process with Multi-layered Metal Complex

M.Kawashima[†], A.Taguchi, N.Oikawa, H.Yamada, and S.Narita

Department of Electrical Engineering and Computer Science, Iwate University
Morioka, Iwate, 020-8551, Japan
[†]t2310010@iwate-u.ac.jp

ABSTRACT

Charged particle emission and anomalous heat evolution have been observed in deuterium loading/unloading process with multi-layered metal sample. These phenomena were supposed to be attributed to a low energy nuclear reaction in condensed matter. MHI group has demonstrated that the selective transmutation can be induced effectively in deuterium permeation with multi-layered Pd/CaO complex. Considering these results, in this study, we performed deuterium desorption experiment with MHI-type Pd/CaO sample, and investigated the nuclear phenomena induced. In several experiments, numerous tracks were recorded on the CR39 detectors and the track diameter distributions were apparently different from background ones. This might suggest that the low energy nuclear reaction in condensed matter has been induced in the deuterium desorption process.

Keywords: Multi-layered metal, Desorption, CR-39

1. Introduction

In the research of the nuclear fusion at low temperature, the observation of nuclear phenomena such as charged particle emission, anomalous heat evolution and nuclear products in deuterium loading/unloading process with multi-layered metal sample have been reported. Yamaguchi et al. have observed excess heat and ${}^4\text{He}$ production in controlled out-diffusion of deuterium from Au/Pd/MnO [1]. Lipson et al. have observed charged particle emission in deuterium desorption from Pd/PdO [2]. Iwamura et al. (MHI group) have reported that the selective transmutation can be induced effectively in deuterium permeation with multi-layered Pd/CaO complex [3]. We also have observed possible excess heat and charged particle

emission in deuterium out-diffusion from Au/Pd/CaO and Pd/CaO/Pd/Au multi-layered samples [4,5]. Considering these results, in this experiment, we examined the MHI type Pd/CaO sample in deuterium desorption experiment and investigated the nuclear reaction in terms of the anomalous heat evolution and the charged particle emission.

2. Experimental

The multi-layered Pd/CaO sample (MHI type sample) was prepared by the following procedure. The Pd foil (10 mm x 10 mm x 0.1 mm) was washed by acetone followed by being annealed at 900 °C for 10 hours. After annealing, the surface contaminants were removed by aqua regia again. Then, the 5

alternate Pd and CaO layers were deposited onto the surface of the foil by Ar ion beam sputtering. It has the same structure as that used in the permeation experiment by Iwamura et al [3]. Figure 1 shows the sample structure.

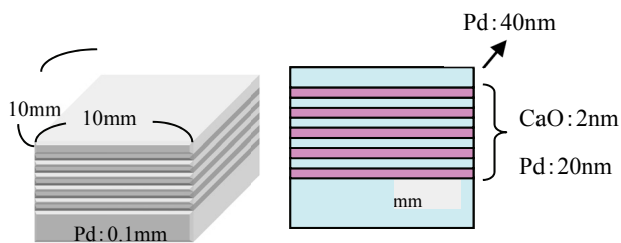


Fig. 1. The sample structure.

Then, the sample was loaded with deuterium being exposed to 5 atm D₂ gas for 20 hours. The weight of the sample was measured before and after loading, and the loading ratio (D/Pd) was calculated from the weight difference. Note that the loading ratio of complex sample was calculated assuming to be composed of Pd only. After loading, the sample was set into the chamber which has a cylindrical shape with volume of 880 cm³ equipped with a turbo-molecular pump to be evacuated. The pressure in the chamber was measured by an ionization vacuum gauge. And the sample temperature was measured by a thermocouple. A DC power supplier supplied the constant current to the sample through gold needles which made the point contacts to the foil Pd side. In this configuration, the electric current is supposed to flow on the surface of the Pd foil. These clips were also utilized for fixing the sample. Figure 2 shows the experimental apparatus. After evacuating the chamber to a pressure below ~10⁻³ Pa, the temperature and pressure in the chamber were measured. Then, the sample was supplied with an

electric current of 8 A. The experiment continued for about 24 h. In the desorption process, we examined for charged particle emission by CR-39 track detector and Si solid state detector (Si-SSD).

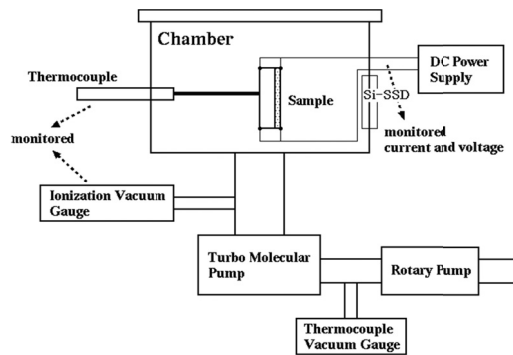


Fig. 2. The experimental apparatus.

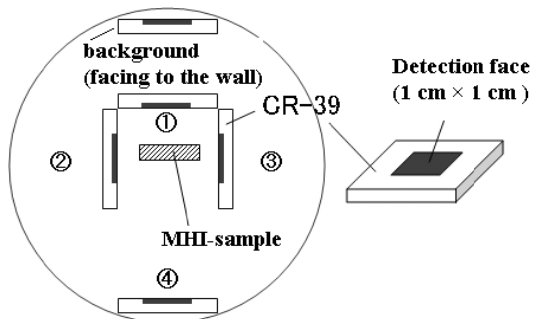


Fig. 3. CR-39 layouts in the vacuum chamber in desorption experiment.

The CR-39 track detector (Fukuchi Chemical Industry) was used for detecting charged particles which can be emitted during the desorption test. The detector is made of diethyleneglycol bis allylcarbonate with a thickness of ~0.9 mm. When a charged particle crosses the CR-39, a part of the energy of the particle is deposited. As the result, chemical composition of the material is changed along the particle trajectory. If we make etching process for the detector in the chemical reagent, a track pit appears because the etching rate for the region which contains the track is

larger than other regions. The etching conditions for this study were 5 N NaOH solutions at 70 °C for 8 hours. The 4 pieces of CR-39 was placed surrounding the sample. A piece of CR-39 was also set in the chamber facing the chamber wall for the background evaluation. Figure 3 shows the layouts of the CR-39 in the vacuum chamber in desorption experiment.

The Si-SSD (EG&G ORTEC BU-020-450-300) was complementarily used for detecting charged particles in this experiment. Figure 4 shows the readout logic of the signal from Si-SSD. The signal from Si-SSD is divided after being amplified. One is fed into ADC gate via the discriminator and the gate generator. The other goes into the shaper amplifier, and then to the ADC.

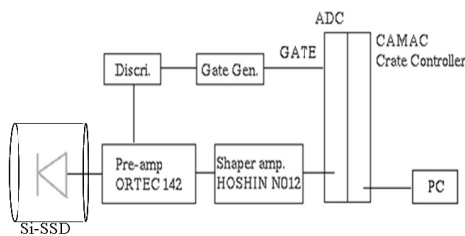


Fig. 4. The readout logic of the signal from Si-SSD.

3. Results and Discussion

3.1 D loading

Figure 5 shows the D/Pd for various multi-layered samples. The averaged values are shown on top of the plot for each sample type. It is found that the D/Pd ratio for MHI-sample is higher than that for bulk Pd and other multi-layered samples tested in our past researches.

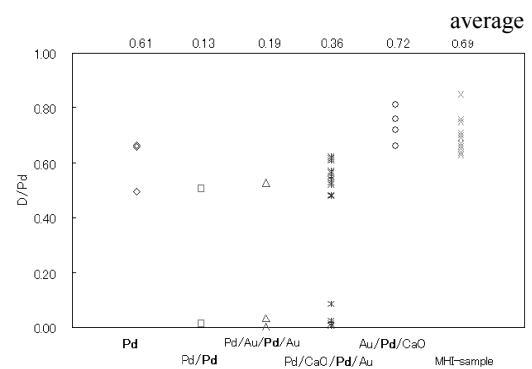


Fig. 5. D/Pd ratio for various multi-layered samples.
 (◇:Pd, □:Pd/Pd, △:Pd/Au/Pd/Au, *:Pd/CaO/Pd/Au,
 ○:Au/Pd/CaO, ×:MHI-sample)

3.2 Desorption test

Figure 6 shows the D/Pd ratio before and after desorption test. It is found that the most of D atoms remained in the sample for the runs without applying the electric current. When the samples were supplied with an electric current, it is found that desorption of deuterium was stimulated by Joule heat.

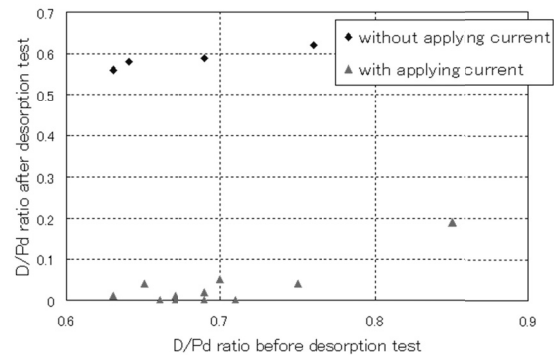


Fig. 6. The change of D/Pd ratio for before and after desorption test.

Figure 7(a) and (b) show the time evolution of the sample temperature and the pressure in the chamber

for the runs without and with applying the electric current, respectively. In this case, we have not observed unexpected heat evolution or explosive gas out-diffusion as observed in our past researches [5].

While, just after applying the current, the temperature and the pressure increased as shown in Fig. 7(b). Now, details of the behavior were investigated at this stage.

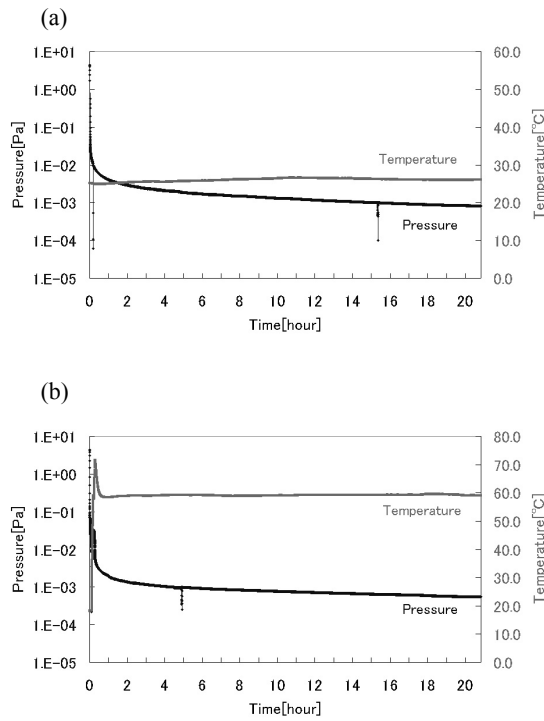


Fig. 7. Time dependence of the sample temperature and the pressure in the chamber (a) without applying current (b) with applying current.

In principle, the sample temperature depends on the heat balance of the joule heating by the applied current and the endothermic reaction in deuterium desorption if we consider the chemical processes. The quantity of the joule heat is basically determined by the electric resistance of the sample, which is the function of the temperature and the D/Pd ratio. If we consider the supplied current to be constant, the

change of the electric resistance can be interpreted by the bias applied to the sample. So we investigated the correlations of the temperature, the pressure (D/Pd), and the bias voltage then, tried to explain the behavior systematically.

We divided the initial time period into 4 stages and tried to explain qualitatively what happened in each stage.

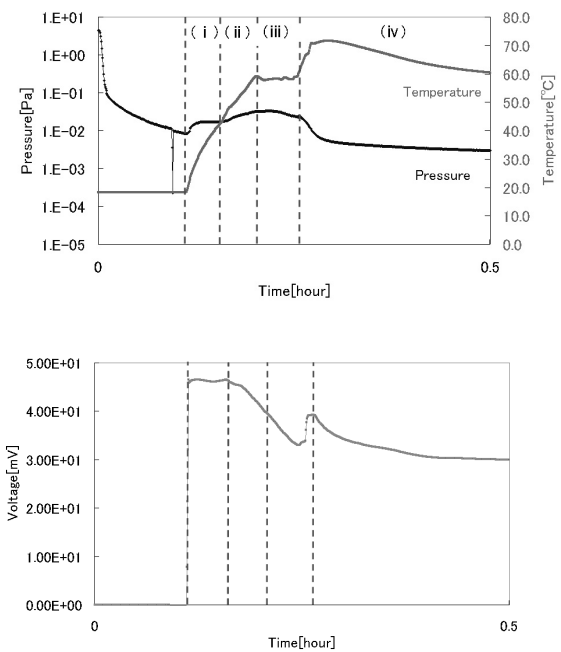


Fig. 8. Time dependence of the sample temperature and the pressure in the chamber and the voltage.

(i) The sample was supplied with an electric current, then the temperature rise by joule heat, so that deuterium diffusion was stimulated. The temperature increase made the resistance higher and the D/Pd decrease caused lowering it, then these effects were supposed to be balanced. As the result, the resistance kept constant. And the observed rise of temperature also related with endothermic reaction

due to deuterium desorption and joule heating.

(ii) The sample resistance increased due to rise of the temperature. In contrast, the decrease of D/Pd by gas diffusion made the resistance lower. The deuterium desorbed more actively comparing with the pressure behavior of the region (i). Therefore the resistance decreased more significantly and it resulted in the drop of the voltage

(iii) Similarly, the sample resistance decreased by deuterium out-diffusion. The endothermic reaction suppressed the temperature increase.

(iv) At the end of the stage (iii), most of deuterium desorbed and the temperature and the voltage got to the equilibrium state.

Thus, the behavior of the temperature, the pressure and the voltage supplied are reasonably explained by known processes, and it did not seem to happen an anomalous reaction in the period.

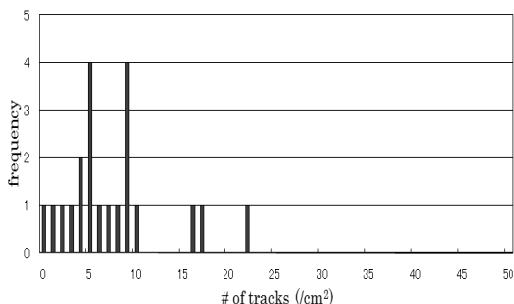


Fig. 9. The number of tracks for the background measurement.

The CR-39 analysis was performed for detecting particle emission in parallel with the measurement of heat evolution. Figure 9 shows the number of tracks recorded on the CR-39 for the background measurement (see Fig. 3). The averaged number of tracks over 20 runs was 7.0 /cm^2 . Considering the standard deviation in the distribution, we took the

events with the number of tracks more than 30 /cm^2 as anomalous ones in the foreground. We observed such anomalous events in 2 out of 4 runs under applying the electric current and 4 out of 14 runs without electric currents.

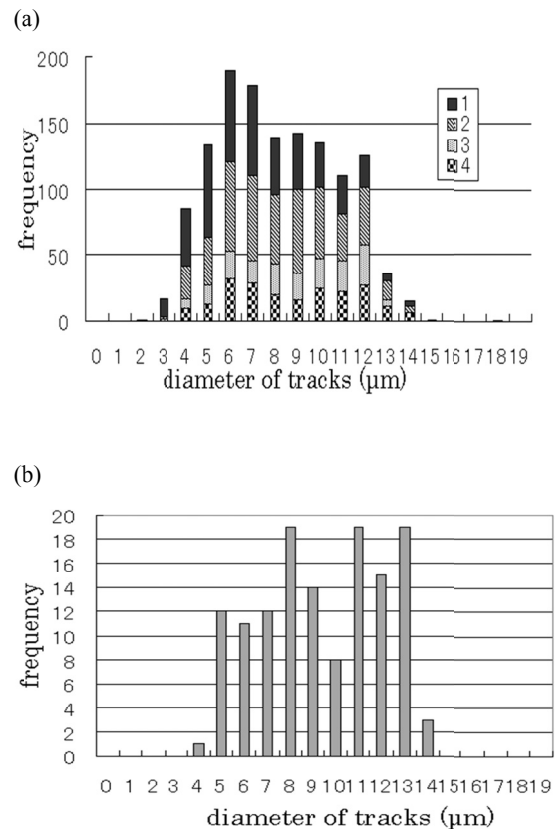


Fig. 10. Diameter distribution of the tracks on CR-39 for (a) foreground and (b)background. The number in (a) express the position of the foreground detector (see Fig. 3).

Figure 10 (a) and (b) show the diameter distribution for the foreground and the background detectors, respectively. The mean diameters of the foreground and the background tracks were $9.6 \mu\text{m}$ and $8.4 \mu\text{m}$, respectively. We did not find a significant difference between these values.

Figure 11 shows the number of tracks recorded on a CR-39 and the mean diameter of tracks for the

foreground and the background events. The distribution of mean diameters of the tracks for foreground events appears to have a peak around 8-10 μm , while the background ones are randomly distributed. And a larger number of tracks tend to be observed for the foreground events.

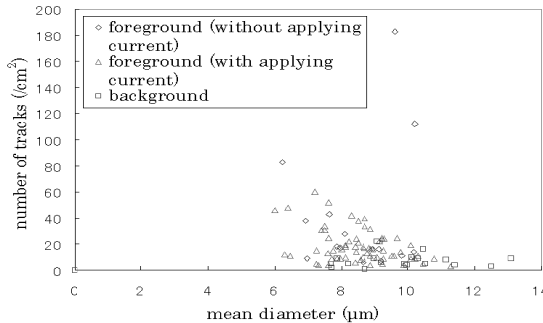


Fig. 11. Number of tracks vs. mean diameter in comparison with the foreground events with the background ones.

As shown in Fig. 11, we have observed the events with the number of tracks of $N = 183 / \text{cm}^2$ at the maximum. Now we pay attention to this anomalous event. Figure 12(a) and (b) show the track diameter distributions of the anomalous event (i.e. $N = 183 / \text{cm}^2$) and other events, respectively. The distribution of the tracks in the anomalous event seems to have clear peak and the mean diameter was larger than that of background. The characteristics of tracks registered on the detector for these runs are definitely different from background one. If the particle is generated by a specific reaction, it has a monochromatic energy. The track diameter should have a peak in that case. It could be suggested that the charged particles were emitted. In addition, a large number of tracks were observed on the CR-39 placed at the position 2 and 3. This may show that the

charged particles were emitted from the edge of the sample.

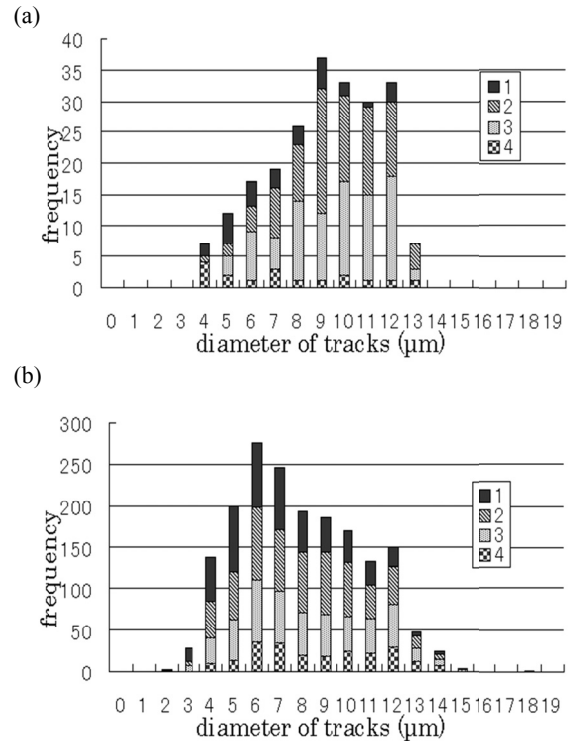


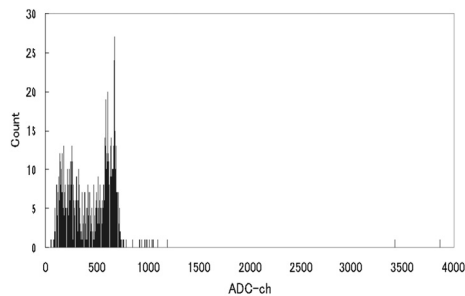
Fig. 12. Diameter distribution of the tracks for the event with (a) $N = 183 / \text{cm}^2$ and (b) other events.

Figure 13(a) shows the ADC distribution of Si-SSD signal for the event with significant number of tracks recorded on CR-39. In order to obtain the data to be referred, we performed additional experiments with the same conditions as that in the desorption test but without setting the sample (This is called “blank runs”). Figure 13(b) shows the ADC distribution for the blank runs.

In the ADC distribution, the signals below 600 ch were observed even in blank run. This signal was thought of noise from outside and dark current. A few signals with larger charge (> 2000 ch in the ADC distributions) were found. However, such large signals were still found in the blank run. Therefore,

such signals could not be the evidence of charged particle emission. Considering the arrangement and the detection efficiency of CR-39 and Si-SSD in the chamber and detection efficiency of Si-SSD, it is possible that the charged particle signal is observed only in CR-39. Thus, we cannot deny the particle emission with this result.

(a)



(b)

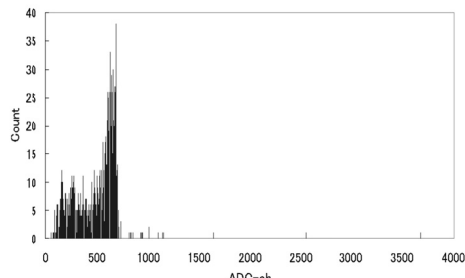


Fig. 13. The ADC distribution of Si-SSD (a) for the event with significant of tracks detected and (b)for blank runs.

4. Summary

We have investigated the behavior of deuterium absorption and desorption followed by possible nuclear phenomena with MHI type Pd/CaO multi-layered sample. We found that this type of sample is capable containing deuterium with higher density for longer term. In the desorption test, the CR-39 was utilized for detecting charged particle

emission as the evidence of occurrence of nuclear events. We observed numerous tracks on the CR-39. Although the background evaluation should be done more carefully, this result may indicate that a low energy nuclear reaction has been induced in deuterium desorption process. We will keep studying the track formation process including the background behavior to find out the origin of anomalous tracks on the CR-39.

References

1. E. Yamaguchi *et al.*, Jpn. J. Appl. Phys. 29 (1990) L666
2. A. G. Lipson *et al.*, Proc. of ICCF12 (2006) 293
3. Y. Iwamura *et al.*, Jpn. J. Appl. Phys. 41 (2002) 4642.
4. S. Narita *et al.*, Proc. of JCF10 (2010) 36.
5. S. Narita *et al.*, Proc. of JCF8 (2007) 5.

Systematic Uncertainties of Isotopic Abundance Measured by TOF-SIMS

S. Narita*, H. Yamada, H. Sasaki, H. Ougida, S. Sato, Y. Suzuki

Department of Electrical Engineering and Computer Science, Iwate University

Morioka, Iwate, 020-8551, JAPAN

* narita@iwate-u.ac.jp

ABSTRACT

In the condensed matter nuclear science, the anomaly in the isotopic abundances of the sample components is often referred as the evidence of nuclear transmutation. TOF-SIMS is popularly used to measure the abundances, and it is known that appreciable changes from natural isotopic composition can occur due to various effects in the measurement. In this study, we measured the isotopic abundance for some types of metal bulk and multi-layered sample with various surface conditions by the semi-quantitative analysis with TOF-SIMS, and the uncertainties were evaluated. As the results, we found that the abundance can be observed with the variety up to 20 % in our typical analysis condition.

Keywords: Isotopic abundance, Transmutation, TOF-SIMS

1. Introduction

In the condensed matter nuclear science (CMNS), the anomaly in the isotopic abundances on the sample components is often referred as the evidence of nuclear transmutation. The time-of-flight secondary ion mass spectrometry (TOF-SIMS) is one of the popular methods to measure the isotope composition and it is often used in the CMNS experiments. In deuterium permeation experiment performed by MHI group, the transmutation from Sr to Mo isotopes was observed. They found that the ratios of the signals on the masses corresponding to Mo isotopes were quite similar to natural abundances of Sr isotopes which were deposited onto the sample surface. This result was considered to be an evidence of the selective transmutation from Sr to Mo [1]. Omori et al. has found that the abundance of Pd isotopes on the surface layers of Pd cathode can change from natural abundance in the light water critical electrolysis [2]. This may also indicate the occurrence of nuclear transmutation. In these experiments, TOF-SIMS was used to analyze the isotope compositions.

In general, TOF-SIMS is capable of analyzing all the elements including their isotopes as well as good sensitivity for detecting a small amount of elements on the sample with a high mass resolution. However, it is known that appreciable changes from natural isotopic composition can occur at near-surface layer of the sample due to various effects such as surface sputtering, surface scattering, thermo diffusion by

external source, and so on [3]. Thus, it is quite important to make out the uncertainties in the TOF-SIMS measurement for the signal intensity of specified isotopes to justify the results of the low energy nuclear transmutation.

In this study, we measured the isotopic abundance for some types of metal foil with various surface conditions by the semi-quantitative analysis with TOF-SIMS. We also prepared the Pd sample loaded and unloaded with deuterium, and analyzed the surface isotopic composition. Then, the varieties of the isotopic abundances were evaluated for those samples and the uncertainties in the measurements were discussed quantitatively.

2. Experiment

2.1 Sample

We examined the isotopic abundance for the following samples; surface processed Ni, Cu and Pd, Pd foil loaded and unloaded deuterium, and multi-layered Pd/CaO complex permeated with D₂ for two weeks. The Pd/CaO complex has the same structure of the sample used in the experiment by Iwamura et al. (so called "MHI-sample") [2]. In the most of experiments for CMNS study, the metal sample is washed with acetone and/or aqua regia in the preprocessing, so that the surface condition can be affected. In order to evaluate the effects, we

prepared Ni, Cu, and Pd foil samples subjected to the following processes; washing process by acetone, etching by soaking into aqua regia for 300s, and scraping the surface by glass paper (#1000). Then, we investigated how much the isotopic abundance changed. The surface morphology of these samples was analyzed by the SEM and the AFM and the observed roughness are shown in Table 1. Even in the case of showing almost same roughness values, the morphology is indeed different in sample by sample. For example, the mesh pattern on the surface of the sample scraped with glass paper is finer and shallower in comparison with that of the sample soaked into aqua regia.

	Ni	Cu	Pd
Washing by acetone	-	-	-
Soak in aqua regia	1 μm	50 nm	0.5 μm
Scraping by glass paper	1.5 μm	1 μm	0.5 μm

Table 1. Roughness of the sample measured by the AFM

In addition, we measured the isotopic abundance of Pd for the bulk Pd foil absorbed and desorbed deuterium and Pd/CaO complex permeated deuterium for two weeks. The surface morphology was also analyzed for these samples. For the sample exposed to deuterium gas, formation of many small protrusions and change in the surface pattern were observed. These changes are supposed to be due to hydrogen embrittlement.

2.2 TOF-SIMS measurement

The TRIFT V nano-ToF (ULVAC Phi) equipped with Bi liquid metal ion source was employed in this study. The primary ion beam was 30 keV Bi⁺ with a 8400 Hz repetition rate and a pulse width of 10 ns. The current on the target surface was 1-2 nA. The analysis area was 40 $\mu\text{m} \times 40 \mu\text{m}$. Mass resolution, $m/\Delta m$, was typically ~ 5000 at $m/z=27$. These conditions are the same in our typical analysis for CMNS study. The depth profile of the abundance was obtained by sputtering with DC Bi⁺ for 0, 30, 60, 180, 300 s. The raster size of the sputtering beam was 200 $\mu\text{m} \times 200 \mu\text{m}$ which covers the analysis area. In our typical measurements, we have not seen the significant variation in the measured mass spectra for the different areas on a sample, so far. Then, we only analyzed the area selected randomly for each sample in this study.

Cu	Mass	63	65				
	Abundance (%)	69.2	30.8				
Ni	Mass	58	60	61	62	64	
	Abundance (%)	68.1	26.2	1.1	3.6	0.9	
Pd	Mass	102	104	105	106	108	110
	Abundance (%)	1.0	11.1	22.3	27.3	26.5	11.7

Table 2. Natural isotopic abundance of Cu, Ni, and Pd.

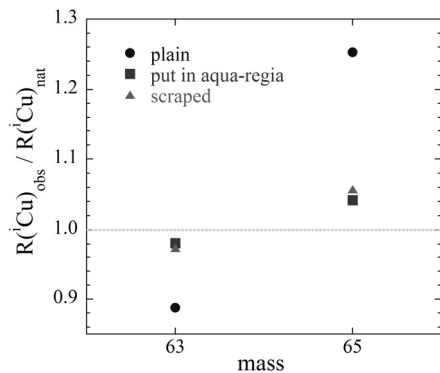


Figure 1. Ratio of observed and natural abundances of Cu isotopes.

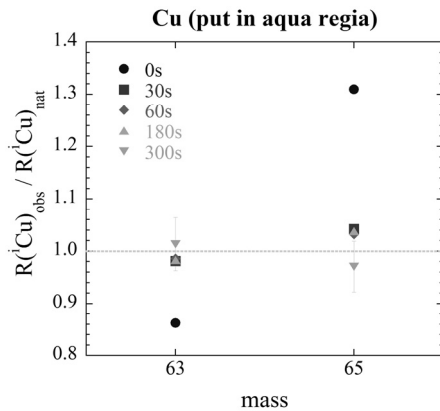


Figure 2. Ratio of observed and natural abundances of Cu soaked in aqua regia. The time variation of surface sputtering is also shown.

3. Results and Discussion

In the evaluation of the change in the abundance, we took into account for the ratio of observed abundance to natural one with the following equation,

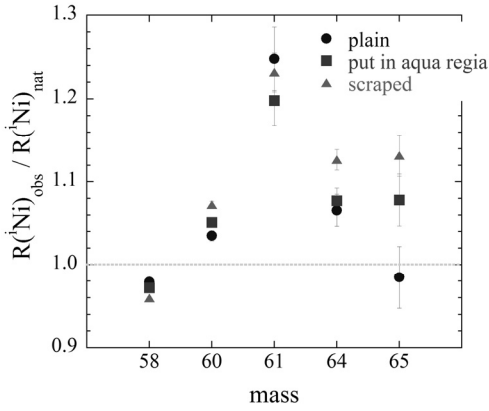


Figure 3. Ratio of observed and natural abundances of Ni isotopes.

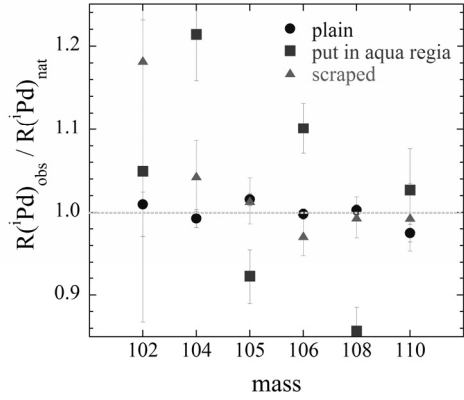


Figure 5. Ratio of observed and natural abundances of Ni isotopes.

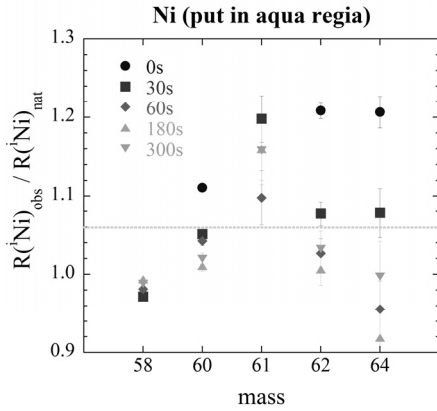


Figure 4. Ratio of observed and natural abundances of Ni soaked in aqua regia. The time variation of surface sputtering is also shown.

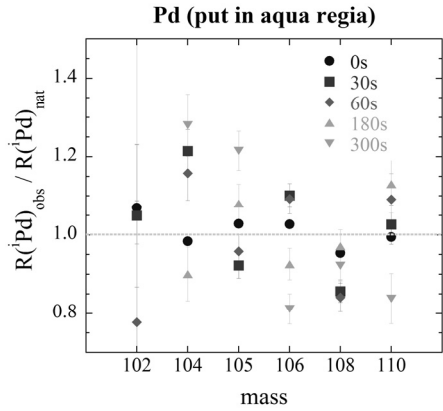


Figure 6. Ratio of observed and natural abundances of Ni soaked in aqua regia. The time variation of surface sputtering is also shown.

$$\frac{\left(\sum_{M_i} N_{M_i} \right)_{\text{observed}}}{\left(\sum_{M_i} N_{M_i} \right)_{\text{natural}}} = \frac{R(M_i)_{\text{obs}}}{R(M_i)_{\text{nat}}}$$

Here, N_{M_i} is the intensity of the TOF-SIMS on the mass of i -th isotope of metal M . The sets of natural abundance for the metals examined in this study are shown in Table 2 [4].

Figure 1 shows the ratios of observed and natural abundances of the Cu isotopes for the samples just washed by acetone (plain sample), soaked in aqua regia for 300 s and scraped the surface. These data were taken after 30 s surface sputtering. Even for the plain sample, the observed abundance is more than 20 % difference from natural one. In general, the relative yield of light isotope in comparison to the heavy one is greater than the natural isotope ratio [5]. However, our result showed the larger ratio in the heavier isotope. This shift is not due to a mass effect,

but supposed to be a kind of systematic uncertainty in our analysis conditions. Figure 2 shows the comparison for the data taken with different sputtering time for the sample soaked in aqua regia. The difference is less than 10 % except for the most surface layer. For the most surface layer (no sputtering), more than 30% difference was observed. Since there is much contaminant on the layer such as molecular ion of hydro-carbon so that the secondary ion signal may overlap the original signal and its intensity becomes larger. We should take really care for this effect on estimating the abundance.

Figure 3 and 4 show the ratios of observed and the natural abundances with the same condition as Cu ones. We found up to 20 % uncertainties. The statistic errors of the isotopes with small abundance stand out rather than the systematic variations.

Figure 5 and 6 show the results for the Pd isotopes. Since the yields of secondary ions for Pd isotopes are relatively low, the statistic errors are

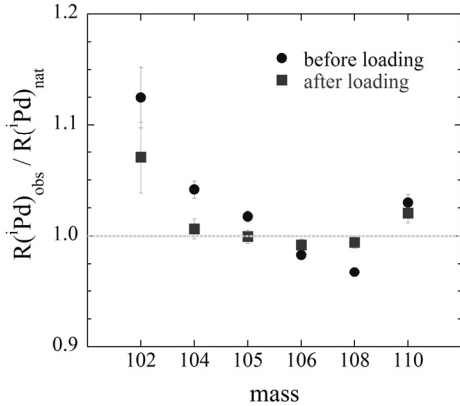


Figure 7. Ratio of observed and natural abundances for Pd before and after deuterium loading.

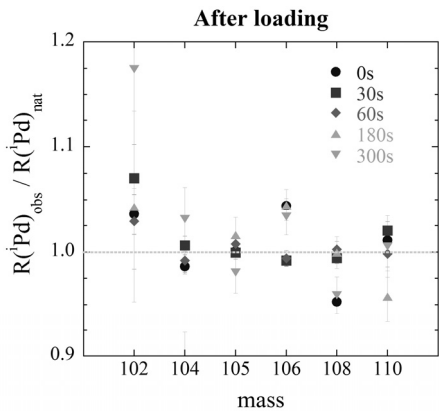


Figure 8. Ratio of observed and natural abundances of Pd after loading deuterium. The time variation of surface sputtering is also shown.

found to be dominant. The difference of the observed abundance is likely to be larger for the sample processed with aqua regia. Also, the difference becomes larger with increasing the sputtering time. For the material with low sputtering and detection efficiency such as Pd, the yields of the secondary ion can be much affected by the surface condition.

Figure 7 and 8 show the results for the Pd sample before and after loading the deuterium. The difference of abundance in each isotope was less than 10 %. According to the AFM and the SEM images, the surface roughness of the sample exposed to deuterium was smaller than that of the plain sample, and much finer pattern was observed on the surface. The yields of the secondary ions are larger comparing with the surface processed sample. In the case of analyzing the metal sample (X) exposed to the hydrogen isotopes, we should be careful about the interference of the molecular ion of XH(D). The signal of the molecular ions can overlap the one for

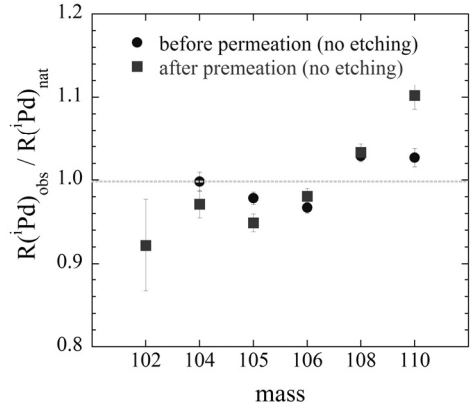


Figure 9. Ratio of observed and natural abundances for Pd/CaO multi-layered complex before and after deuterium permeation.

the element with corresponding mass. Now we consider the effect in the analysis of the Pd sample exposed to deuterium. Assuming that the probabilities of the formation of PdD molecule for every Pd isotopes are same, the signal intensity of the mass corresponding to the Pd isotopes are determined as follows;

$$\text{Mass 102: } N(^{102}\text{Pd}) - N(\text{PdD}) \times R(^{102}\text{Pd})$$

$$\text{Mass 104: } N(^{104}\text{Pd}) - N(\text{PdD}) \times \{R(^{104}\text{Pd}) - R(^{102}\text{Pd})\}$$

$$\text{Mass 105: } N(^{105}\text{Pd}) - N(\text{PdD}) \times R(^{105}\text{Pd})$$

$$\text{Mass 106: } N(^{106}\text{Pd}) - N(\text{PdD}) \times \{R(^{106}\text{Pd}) - R(^{104}\text{Pd})\}$$

$$\text{Mass 108: } N(^{108}\text{Pd}) - N(\text{PdD}) \times \{R(^{108}\text{Pd}) - R(^{106}\text{Pd})\}$$

$$\text{Mass 110: } N(^{110}\text{Pd}) - N(\text{PdD}) \times \{R(^{110}\text{Pd}) - R(^{108}\text{Pd})\}$$

where $N(^i\text{Pd})$ and $N(\text{PdD})$ is the number of the ^iPd isotope and the PdD compound, respectively, and $R(^i\text{Pd})$ is the natural abundance of ^iPd isotope. Substituting the value of the natural abundance (see Table 2) for the equations above, the abundances of ^{102}Pd , ^{104}Pd and ^{105}Pd get smaller, while the abundances of ^{106}Pd , ^{108}Pd and ^{110}Pd get larger. We have not seen such tendency clearly in our results. Thus, the effect of the PdD compound is smaller than that of other effects.

Finally, the differences in abundance of each isotope for Pd/CaO multi-layered complex are shown in Fig. 9. Although the difference seems to become larger sample subjected to deuterium permeation, it is still less than 10 %.

4. Summary

We have measured the isotopic abundance for the samples with various surface conditions with semi-quantitative analysis by TOF-SIMS. We found the uncertainty in determining the abundance is up to

20 %, and no clear dependence on the surface morphology. For the isotopes with lower yields of secondary ions, the statistic error is dominant in the uncertainties. We should consider these results when we discuss the anomaly in isotopic abundance in CMNS study.

References

1. Y. Iwamura *et al.*, Jpn. J. Appl. Phys. 41 (2002) 4642.
2. T. Ohmori *et al.*, Proc. of JCF5 (2004) 36.
3. N. N. Nikitenkov *et al.*, Vacuum 81 (2006) 202.
4. K. J. R. Rosman and P. D. P. Taylor, Pure & Appl. Chem., 70, (1998) 217.
5. "Secondary Ion Mass Spectrometry" The Surface Science Society of Japan (1999) (in Japanese).

Detection of Energetic Charged Particles from Thin Metal Cathodes in Heavy and Light Water Electrolysis Using CR39

H. Yamada, S. Narita, S. Sato, H. Aizawa, K. Mita, Y. Takahashi, Y. Abe, Y. Shida
and H. Nanao*

Department of Electrical and Electronic Engineering, Iwate University, Ueda 4-3-5, Morioka,
020-8551 Japan *yamadahi@iwate-u.ac.jp*

* Department of Chemical Engineering, Iwate University, Ueda 4-3-5, Morioka, 020-8551
Japan

Abstract: Heavy and light water electrolysis of Li₂SO₄ solution were performed using CR-39 track detector in conjunction with the 5-μm thick Ni and 2.5-μm thick Au cathodes, which form the inner bottom of the test cell. The CR-39 track detector was positioned just under the metal film cathodes as being in close contact with the metal film. This construction can minimize the energy loss of charged particles penetrating through the thin cathode and maximize the detecting efficiency of emitted particle. The results of electrolysis experiments were compared with those of control experiments to investigate low energy nuclear reaction generated in the course of electrolysis.

Keywords: Heavy water electrolysis, Light water electrolysis, CR-39, Thin metal cathode,
Low energy nuclear reaction

1. Introduction

The plastic track detector has become a popular method to detect charged particles in low energy nuclear reaction (LENR) studies especially in electrolysis experiments. In these studies, the evidence of the reaction is in the form of nuclear damage trails made visible by etching of the plastic chips. The sophisticated experimental techniques have been developed by Lipson et al.¹⁾, Roussetski²⁾ and Oriani et al.³⁾ to show the generation of nuclear particles during electrolysis. However, there still exist technical complexities in using plastic track detector chips in electrolysis experiments, which might cause unreliable analytical results.

The primary purpose of this study is to establish a simple technique producing new convincing evidence that a nuclear reaction as LENR could accompany both heavy and light water electrolysis.

The present technique is simple but capable of detecting energetic charged particles produced on the cathode during electrolysis with relatively high efficiency. In the present investigation, the plastic chip of the CR-39 track detector is positioned just under the thin metal film cathode; the film is

sandwiched between the electrolyte and the CR-39 chip. This construction avoids chemical attack on the chip by ions generated by the electrochemical reactions on the metal film cathode. The simplicity of this construction is expected to shorten the experimental time to the order of ten min and to minimize the noise particles from environment during the electrolysis. Using the present technique, we have studied energetic charged particle emission from the thin Ni cathode in heavy water electrolysis and from the thin Au cathode in light water electrolysis⁴⁾.

2. Experimental

Electrolysis was carried out in a small plastic cell shown schematically in Fig. 1. It consists of a vertical plastic cylinder with 105 mm long and 10 mm inside diameter, a plastic cap, a lower portion of plastic base and electrodes. The vertical cross section of the lower portion is shown in the lower part of Fig. 1. The diameters of the upper and the lower disc of the portion are 62 and 100 mm, respectively. The left side and right side of Fig. 2 display the components of the cell and the cell assembled, respectively. The top end of cylindrical portion of the cell is covered by

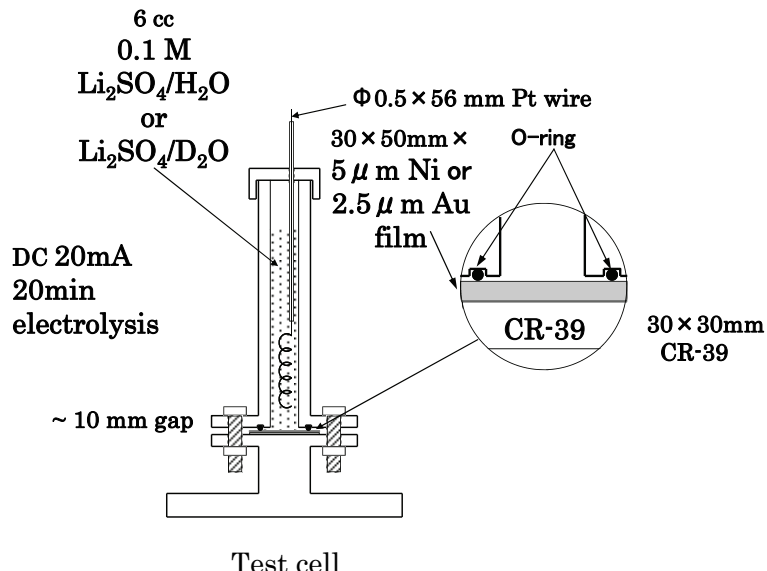


Fig. 1 The vertical cross section of the test cell.

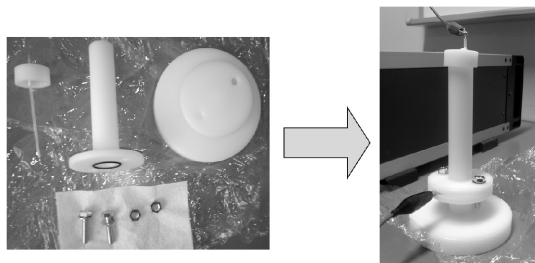


Fig. 2 The view of the test cell, (left) its components and (right) assembled

a plastic cap with loose contact, which permits the escape of the gas produced by electrolysis. A 5- μm thick Ni film and a 2.5- μm thick Au film were used as metal cathodes for heavy and light water electrolysis, respectively. These films form the inner bottom of the test cell and serves as cathodes: the diameter of the cathodes is 10 mm. The anode is a part of $\phi 0.5$ mm Pt wire and the upper portion of it is sheathed by heat-shrinkable PTFE tube. The anode is the lower portion (56 mm long) of the Pt wire forming a crude spiral with the diameter and length of ~ 5 mm and 27 mm, respectively. The anode spiral is terminated above the metal film cathode with a gap distance of ~ 10 mm.

A 30×30 mm chip was cut from a sheet of the track detector CR-39, produced by Fukuchi Chemical Industry Co., just before each electrolysis experiment. The chips are carefully manipulated with tweezers. The center area of the front surface, which contacts to the metal film, is scratched to form a 10×10 mm square lines, before removing the manufacturer-supplied blue protective film. The CR-39 chip is mounted in the electrolysis cell immediately after removing the protective film. The scratched surface is referred to as the front surface upon which the metal film cathode is overlaid. The rear surface of the metal film cathode area is set in close contact with the surface of the inside area bounded by the scratched 10×10 mm square line on the front surface of the CR-39 chip. Both the metal film and the CR-39 chip are clamped together on the disc forming the bottom cap of the cell with an O-ring seal.

The electrolyte solution for the heavy water electrolysis was 0.1 and 0.2-M $\text{Li}_2\text{SO}_4/\text{D}_2\text{O}$. That for the light water electrolysis was 0.1-M $\text{Li}_2\text{SO}_4/\text{H}_2\text{O}$ with an initial composition of 1.345 g Li_2SO_4 per 122 ml H_2O . The volume of the electrolyte solution in the test cell was ~ 6 ml.

After the lower portion of the cell was assembled to form a small vessel, the ~6 ml electrolyte solution was poured into the cell. Then, the cover cap holding the anode was put on the upper opening. The electrolysis was conducted mainly for ~20 min by constant application of ~20 mA DC at a voltage of ~6 V. The tests with the electrolysis time extended to 1,200 min were also carried out for heavy water electrolysis. The current for the electrolysis was supplied by a constant-current power supply and no water was added during the electrolysis. After those tests the cell assembly was immediately disassembled to remove the CR-39 chip and the metal film used.

A control experiment and a blank experiment were performed. The CR-39 chips used in control and blank experiments were carefully handled in exactly the same way as those used in the electrolysis experiments.

The control one, which is designated "Reference" in the figures of the present report, followed immediately after the electrolysis experiment. The CR-39 chips used for control experiments were always cut from a part of the sheet, neighboring to that for the corresponding electrolysis experiment. The CR-39 chips were mounted in the newly assembled cell fitted with an unused metal film and an electrolyte in the absence of electrolysis. The exposure time of CR-39 for the control experiments was the same as that for the electrolysis experiment.

In the blank experiment, which is designated as "Background" in the figure, the CR-39 chips were positioned near the ongoing electrolysis cell during the electrolysis.

The CR-39 was etched in 5-M NaOH solution for 8 h at 70 °C immediately after each experiment. The measurements of etch pits were carried out using a digital microscope system (KEYENCE VHX-200), consisting of an optical microscope with a camera and a PC. The small area 0.79 cm² of the metal film cathode and the corresponding 10×10 mm measurement area of the CR-39 chip enable us to count the exact number of the etch pits.

3. Result and Discussion

The appearance of the nuclear pits shows a tendency to have much darker wide rim in the microscope. Because the pit has a relatively deeper bottom and the diameter of the bottom is rather small compared with that of the rim. To the contrary, the other artifactual pits usually give narrow darker rim because of its shallow form. However, there still exist many ambiguous pits whose origin, nuclear or artifactual, is hardly determined. Thus, the etch pits with narrow darker rim were not excluded in counting in this study; all the etch pits observed were counted.

The pits were counted only within the inside area bounded by the scratched 10×10 mm square line on the front surface of the CR-39 chip. The number of pits in the inside area was compared with that found in the control and the blank samples.

Figure 3 shows the typical photomicrograph of pits, which are thought to have the nuclear origin.

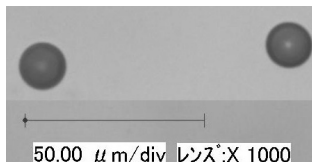


Fig. 3 Photomicrograph of a surface of the CR-39 chip, providing a pair of etch pits.

3. 1 Heavy water electrolysis with Ni cathodes

Figures 4 and 5 show the relations between total numbers and the diameter of the etch pit for heavy water electrolysis using 0.1-M and 0.2-M solutions, respectively. The total number of pits for each diameter bin in these figures is the sum of them over 5 runs. The number of the etch pit in the diameter range 3–9 μm for the chips exposed during electrolysis is larger than that for the control experiment, as seen in Fig. 4. To the contrary, most of the etch pits for the control experiments have diameters larger than 10 μm. However, the former characteristic was unclearly observed for 0.2-M solution, as seen in Fig. 5, where the number of etch pits in the

diameter range 3-9 μm is smaller than that in Fig. 4.

The control experiments are expected to give some nuclear tracks already present in the CR-39 sheet as received from the supplier, as well as those produced during the entire experimental process by radioisotopes such as radon in the environment including air, the electrolyte, etching solution. In addition, some of the pits originating from manufacturing defects will unavoidably have

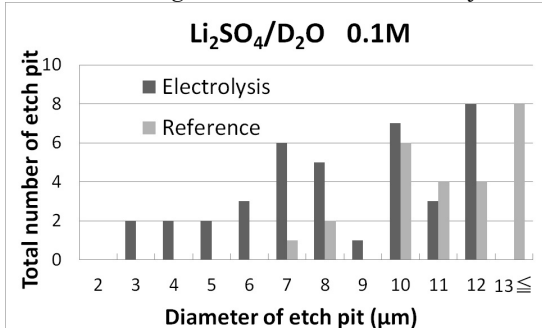


Fig. 4 Distribution of etch pit diameter collected from 5 runs of electrolysis and the corresponding 5 control experiments.

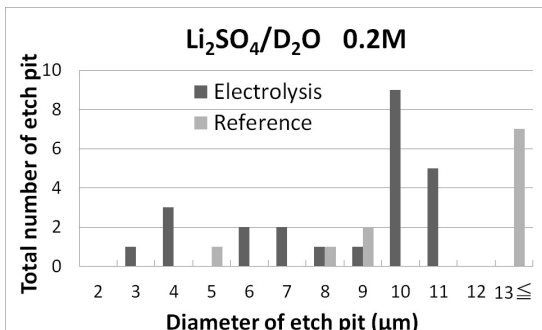


Fig. 5 Distribution of etch pit diameter collected from 5 runs of electrolysis and the corresponding 5 control experiments.

a similar form to that of nuclear pits. Namely, the pits compiled into Fig. 4 and 5 for electrolysis experiments would include the pits originated from manufacturing defects and tracks different from that produced by the electrolysis.

The diameter distribution of etch pit collected from 10 runs of the blank test is given in Fig. 6, where most etch pit have the

diameter in the range of 10-12 μm . This would imply that the most of etch pits with diameter larger than 10 μm in the distribution of Fig. 4 and 5 are not attributed to particles produced by the electrolysis. Figure 7 provides the diameter distribution obtained by summing up the distributions shown in Fig. 4 and 5 with the diameter ranges greater than 10 μm neglected. This distribution could elucidate that marked number of nuclear tracks relating to etch pits with diameter range 3-9 μm were produced during the electrolysis. Referring to the calibration date reported by Roussetski²⁾, we see that the diameter range 6-9 μm corresponds roughly to the energy range of ~1 MeV for protons and 5-30 MeV for α particles.

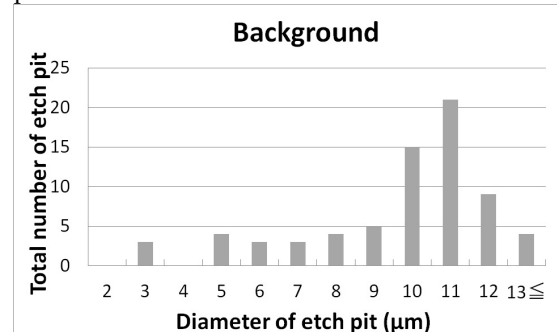


Fig. 6 Distribution of the etch pit diameter collected from 10 blank tests.

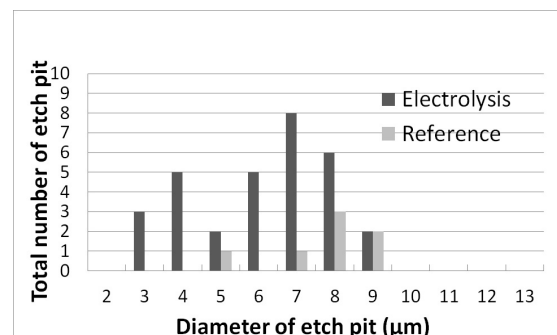


Fig. 7 Diameter distribution obtained by summing up the distributions shown in Fig. 4 and 5 with the diameter ranges greater than 10 μm neglected.

By more carefully reviewing the results, the characteristic of the distribution of Fig. 5 for 0.2-M solution looks similar to that of Fig.

6. This may indicate that the LENR could be more difficult to take place in the higher-density solution.

Of particular interest is the fact that almost no increasing number of etch pit was observed by extending electrolysis time to 1,200 min. This may imply that the most part of the charged particles emission occurred within 20 min from the beginning of electrolysis for the heavy water electrolysis with the Ni cathode. The diffusion constant of D in Ni is so small that the density of D in near surface of Ni cathode could be saturated in short time. Accordingly, the density of D in the uppermost surface region might become large enough for the LENR to occur shortly after beginning of electrolysis.

3. 2 Light water electrolysis with Au cathodes

Figure 8 shows the distribution of the etch pit diameter in a run for light water electrolysis using Au film cathode in 0.1-M Li₂SO₄ solution. It presents rare, but possible distribution with no etch pit observed for the control experiment.

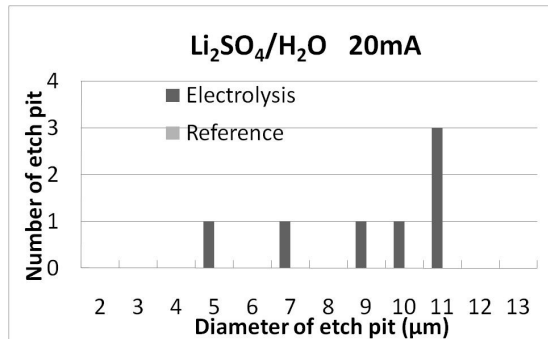


Fig. 8 Diameter distribution of the etch pit observed in an electrolysis experiment with no etch pit observed for corresponding control experiment.

Fig. 9 shows a compiled distribution, where the number in each diameter bin is the summed value for 4 electrolysis runs. It could fairly be seen that the number of the etch pit in the electrolysis case is larger than that in the control experiment in the diameter range 5-9 μm. Some of etch pits with diameter in this range for the electrolysis experiment seem to be attributed to the tracks produced

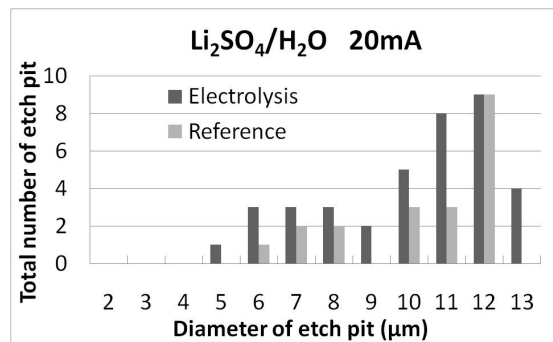


Fig. 9 Distribution of the etch pit diameter collected from 4 runs of electrolysis and the corresponding 4 control experiments.

by the electrolysis. The characteristic of the distribution in the figure looks different from that obtained for electrolysis of 0.1-M Li₂SO₄/H₂O solution using the same Ni film cathode, where a semi-Boltzmann distribution with a peak at 5 μm was observed ⁵⁾. One of the reasons for the difference of the distribution characteristic might be the change in the type of the etch pits counted; only the pits with much darker wide rim were counted in the previous study ⁵⁾.

It has already been confirmed that both the current flowing through the metal cathode and mechanical stirring of electrolyte have no effect on producing tracks at all ⁵⁾.

5. Conclusion

A simple experimental technique using thin Ni and Au film cathodes in conjunction with the track detector CR-39 for nuclear reaction in heavy and light water electrolysis is presented. The result has provided a possibility of LENR occurring on the Ni film cathode during the 20 min Li₂SO₄/D₂O electrolysis and on the Au film cathode in Li₂SO₄/H₂O electrolysis.

All the results might show a characteristic of LENR in the electrolysis experiments that the reaction will not always take place in every experiment but do occasionally under the similar experimental condition.

References

- 1) A. G. Lipson et al., Proc. 11th Int. Conf. Cold Fusion, p. 324 (2004)
- 2) A. S. Roussetski, Proc. 11th Int. Conf. Cold Fusion, p. 274 (2004)
- 3) R. A. Oriani et al., Jpn. J. Appl. Phys., Vol. 41, p. 6180 (2002)
- 4) T. Ohmori et al., Fusion Technol., Vol. 33, p. 367 (1998)
- 5) H. Yamada et al., Proc. 10th Meeting of Japan CF Research Society, p. 41 (2010)

Mesoscopic Catalyst and D-Cluster Fusion

A.Takahashi², A. Kitamura¹, Y. Miyoshi¹, H. Sakoh¹, A. Taniike¹, R. Seto² and Y. Fujita²

¹Kobe University, ²Technova Inc.

Abstract: Discussions with brief summary of the Kobe group's gas-loading experiments are given. Phenomenological modeling on mechanisms are made for explaining observed anomalies in D(H)-overloading and high heat-power release rates from nano-palladium-particles and binary metal PdNi nano-particles dispersed into/onto ZrO₂ ceramics supporter flakes under D(H)-gas loading at room temperature. Roles of the PdO layer on Pd-particle and the Pd-ad-atoms (incomplete outer shell) of nano-Ni-core are modeled as mesoscopic catalysts which have sub-nano-holes (SNH) on nano-particle-surfaces. SNH may realize strong sticking force for D(H)-gas to dissociate and diffuse rapidly into inner local lattice sites. During the beginning process, 4D/TSC cluster fusions with 1watt/g-Pd(or PdNi) may happen on surface SNH sites. By the very over-loading ($x \gg 1$) states in the later region of Phase-I and in the Phase-II after saturation, TSC formation inside nano-particles may be strongly enhanced by the non-linearly coupled QM oscillation (high free energy states of deuterons in local Bloch potentials) under the deep mesoscopic global collective potential well.

Keywords: Pd nano-particle, binary PdNi nano-particle, D(H)-gas-loading, anomalies, over-loading, high heat-power, mesoscopic catalyst, D-cluster, 4D fusion

1. Introduction

Very rapid MD(H)x over-full loading ($x > 1$) under near "zero pressure" of D(H)-gas and anomalously large released heat (0.6-2.0 eV/D(H)) in Phase-I period are reproducibly observed for Pd/ZrO₂ (PZ) and Pd/Ni/ZrO₂ (PNZ) samples by our group¹⁻³. By the forced oxidization (5-10% PdO or MO formation) of used PZ and PNZ samples, a surprising recovery of performance on the loading ratio ($x > 1$) and heat release level (0.9-1.5eV/D(H)) has been repeatedly observed¹⁻³. To study dynamic behavior of D(H)-sorption (adsorption/absorption) from the start, time-dependent measurements^{3,5} of the evolutions for D(H)/M ratios and η -values (dynamic released energy per a D(H)-sorption) have provided quite interesting data, namely the very large dynamic isotope effects, which suggest some "nuclear effects" taking place at least partially⁴. In the present paper, we propose and discuss mechanisms to answer why such "chemical + nuclear" anomalies take place in "mesoscopic" particles dispersed in metal-oxides (ceramics) powders (flakes).

Special roles of the PdO surface layer⁴ and the ad-atoms of Pd on the Ni nano-core are modeled to gain an understanding of the generation of surface sub-nano-holes (SNH). SNH may trap D(H)-clusters on the surface with deep adsorption potential, providing seeds of 4D/TSC-induced 4d fusion

(23.8MeV/⁴He-product)⁴. It enhances D(H)-diffusion into Pd (and the Ni nano-core of binary alloys) lattice sites of nano-particles, and at the end of Phase-I realizes the $x > 1$ state with a "very deep (1.5-1.8eV for PZ and about 0.6eV for PNZ)" global potential for trapping (GPT) of *mesoscopic catalyst* which generates anomalous chemical heat for D(H)-gas absorption at room temperature. In GPT there holds local shrunken Bloch potentials for PdD(H) or NiD₃(H₃) lattice to induce the non-linearly coupled D(H)-oscillation mode that strongly enhances the dynamic TSC (tetrahedral symmetric condensate; transitory Bose-Einstein-Condensate) formation probability inside the nano-particle⁴. Binary-metal nano-particles with incomplete-shell/core, dispersed in ceramics supporter flake, are promising for providing very large ($x > 3.0$) loading and long lasting high level heat-power in repeatable usage.

2. Examples of anomalous data observed

Brief summary is given in this section to show typical anomalies obtained by using PZ, PNZ-I and PNZ2B samples^{3,5,6}. D(H)-gas charging experiments were done for the virgin -as received- samples (#1 runs), the forced de-oxidization samples (#2 runs) and the forced oxidization samples (#3 runs), after baking process. Runs without the baking process are labeled as #1A and #1B. Desorption runs

by evacuation are labeled as #1d and #1Ad. Using the twin system¹⁻³, simultaneous runs for D-gas and H-gas charging were made for measuring time-dependent D(H)-loading rates, heat-powers, gas-pressure, neutron counts (by a ³He counter) and gamma-ray counts (by an NaI counter). No meaningful increases of neutron and gamma-ray counts over natural background were observed for all runs reported here. Heat-power evolution data and gas-pressure data can be classified into two regions, namely the phase-I and the phase-II¹⁻³. In the phase-I interval, major heat release happens with “near zero” gas-pressure and rapidly increasing D(H)-loading rates, while in the phase-II we observe saturated states of D(H)-loading and sometimes find low level excess heat for D-charging only.

2.1 Anomalies by PZ samples

PZ sample is made of 34.6%Pd + 65.4%Zr material plus oxygen-atoms to form nano-Pd/ZrO₂ powder. Sizes in 8-10nm diameter of Pd-nano-particles were analyzed by TEM^{2,3,5}. Detail of experiments is written in Ref-5. Integral heat data in the phase-I for the PZ samples are shown in Fig.1 for time-order of runs.

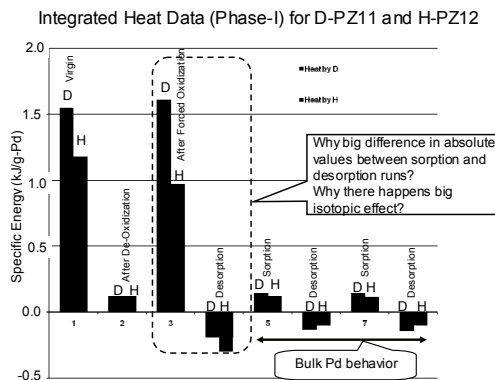


Fig.1 Integral heat data in phase-I obtained by PZ samples

Heat values of #1 runs by virgin samples are anomalously large, compared with known values for bulk-Pd metal as observed in later sorption/desorption runs (#3A, #3Ad, and so on). The runs (#2) after the forced de-oxidization of PZ samples gave similar values to the bulk ones. Observed maximum D(H)-loading ratios, $x = [D(H)]/[Pd]$, for #1 run was over-full loading

$x=2.0$ (H and D), while $x=0.45$ (H) and 0.60 (D) for the #2 runs. Surprisingly the #3 runs after the slight oxidization (speculating 5-8% PdO surface layer formation on Pd-nano-particles⁴) showed “full” recovery of heat-level and over-full loading ratios ($x = 1.4$ for H and 2.0 for D). Heat levels by the D-gas-charging, especially for the #3 run are significantly higher than those of the H-gas-charging. However the desorption runs (#3d) gave much smaller absolute values of heat-absorption (endothermic reaction). In usually known data for bulk Pd give almost same values of heat levels (regarded as binding energies of D(H)-atoms in metal lattice) between the sorption (adsorption plus absorption) exothermic heat and the desorption endothermic heat. It is a common sense of “chemistry” in hydrogen in metal. Why did such large isotopic effects for #1 and #3 runs happen?

In Fig.2, we show isotopic ratios of η -values^{3,5,6}, which are dynamic data of D(H) binding energies (plus alpha for D!) in Pd-nano-particles during the time-dependent sorption process.

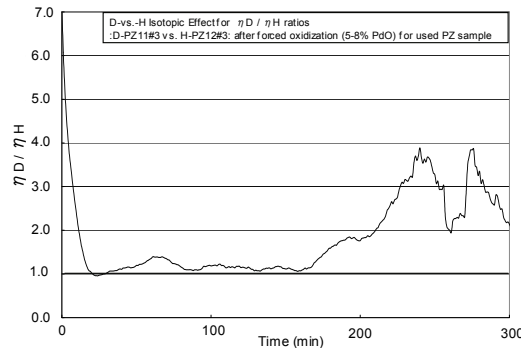


Fig.2 Dynamic isotopic ratios of η -values for oxidized PZ samples (by #3 simultaneous runs for D- and H-loading)

In usual chemistry sense, the ratio should behave around 1.0 and may have about 10% or less isotopic effect, because the binding energies are reflected as almost the same electron-bonding energies between D(H)-atoms and metal lattice-atoms for D- and H-isotopes. Therefore, we are interested in the time-intervals where the ratios deviated much over the 1.0 “chemical line”, as it may show the information of some nuclear-origin energy induced by deuterons. In Fig.2, we notice that the interval for

η -ratio $\gg 1.0$ appears already in the beginning of D(H)-gas charging. The ratio is as large as 6.5 in the very beginning ($\eta=2.0\text{eV}$ for D). It is a surprise and has never been expected in the past Cold Fusion (electrolysis) experiments which required very long “waiting time”. The other large ratios in the later time interval after 200 minutes need our careful study due to the difference of gas-flow rates between D- and H-charging. In addition, we observed sub-phases (the phase-Ia and the phase-Ib)^{3,5}, reason of which should also be investigated further.

2.2 Anomalies by PNZ-type samples

Before PNZ runs, we tested NZ sample (35.8%Ni and 64.2%Zr) to have no measurable D(H)-loading and heat levels at room temperature (around 20 deg C). Then we tested PNZ-I sample (10.5%Pd, 25.3%Ni and 64.2%Zr) to get anomalously large D(H)/Pd ratios and heat-levels³, which were however proportional to the amount of contained Pd-atoms and looks independent of the amount of Ni. The third trial using PNZ2B sample (4%Pd, 29%Ni and 67%Zr) has given us the surprising results⁶, showing very large loading ratios [D(H)]/[M=0.125Pd + 0.875Ni], over 3.0 and anomalously high heat levels. What is the reason of such drastic change between the experimental results for NZ, PNZ-I and PNZ2B? Why can the much smaller amount of Pd atoms in PNZ2B induce the great and anomalous loading and heat effects?

In Fig.3, we show an example of raw data for the #3 (forced oxidization) run using PNZ2B samples.

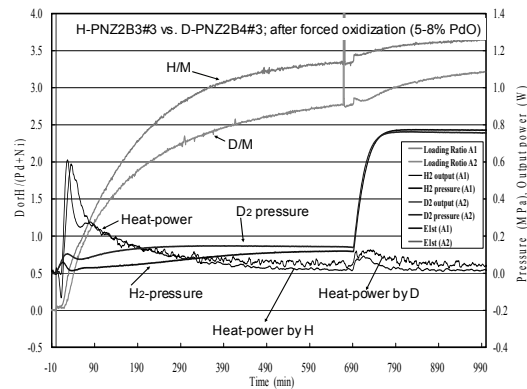


Fig.3: Raw data of D(H)/M ratios, heat-powers and gas-pressure for the PNZ2B(3,4)#3 runs

We see significant isotopic effects in D(H)/M evolutions, heat-power-levels and gas-pressure for about 15 hours twin-cell run. Maximum loading ratios exceeded the 3.0 line. We can see “excess heat-power” for the D-gas charging in the later time region (the phase-II?); reproducibility of which shall be further confirmed. In Fig.4, we show data of heat-powers and η -values.

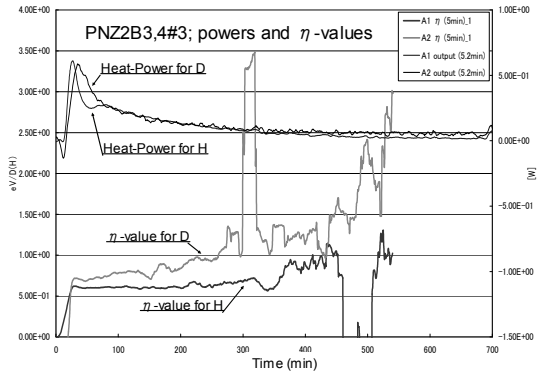


Fig.4: Evolutions of heat-powers and η -values for the #3 runs of PNZ2B samples after the forced oxidization

We see the η -values by the D-gas charging increase more and more as time elapses, while those by the H-gas charging keep almost constant values (about 0.6eV per one H-atom sorption) until about 300 minutes (5 hours). Data for H after about 350 minutes became poor in accuracy due to decaying heat-power level (approaching to zero and difficult to calculate η -values there). The sudden and large peak of η -values for D just after 300 minutes might be by chance and unknown happening. The data for isotopic ratios of η -values are shown in Fig.5.

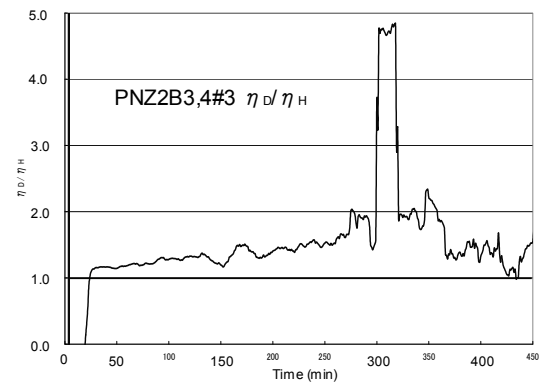


Fig.5: Isotopic ratios of η -values PNZ2B#3 runs after the forced oxidization

These data for the #3 runs of PNZ2B may suggest a gradually enhancing nuclear effect as time elapses.

In Fig.6, we show the data of isotopic ratios of η -values for the #2 (forced de-oxidization) run of PNZ2B samples. We observed very large (near 3.0, see Fig.8) maximum D(H)/M loading ratios and as high heat levels as those of the #1 virgin runs for PNZ2B. It is drastically different aspect from the results of PZ samples. The forced de-oxidization, namely complete reduction of oxygen atoms from the sample *did work* for the anomalous over-loading and high heat-level effect, in the case of binary (Pd-Ni) nano-particles dispersed into/onto ceramics (ZrO_2) supporter flakes. What is the reason?

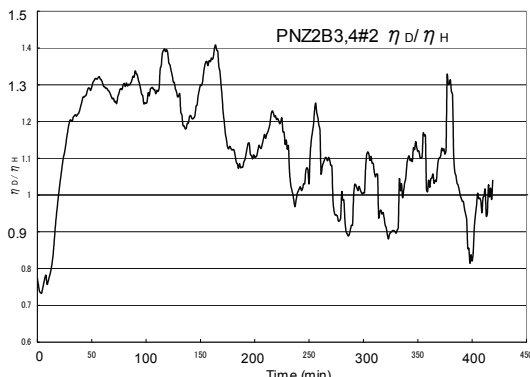


Fig.6: Data for isotopic effect on η -values for the #2 (forced de-oxidization) runs of PNZ2B samples

In Fig.7, we show the data of isotopic ratios of η -values for the virgin (#1) runs of PNZ2B samples

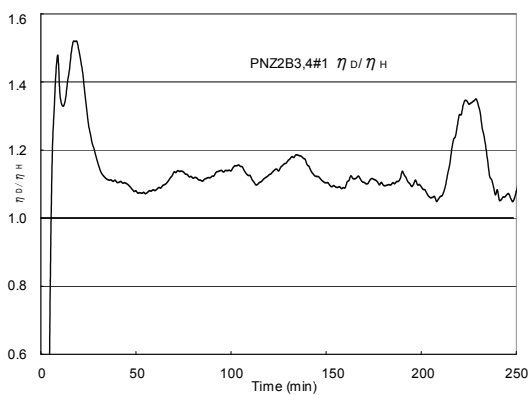


Fig.7: Data for isotopic effect on η -values for the #1 (virgin) runs of PNZ2B samples

These two data (Figs. 6 and 7) show the existence of local time regions where η -values for the D-gas

charging are larger as much as 50% which are already difficult to explain by the isotopic effect of usual chemical reactions. In addition, behaviors of the ratios are very time-dependent, although we expect rather constant ratios near 1.0 for any chemical reactions.

In Fig.8, we summarized observed maximum loading ratios for PNZ2B samples, for the initial series of #1 to #3 runs and the reused series runs.

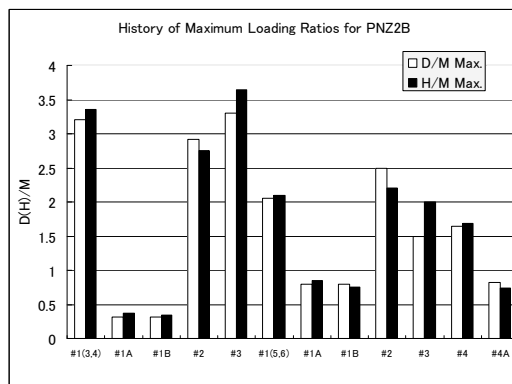


Fig.8: Observed variation of maximum D(H)-loading ratios for the first series runs (3,4) and the reused series runs (5,6) of PNZ2B samples

We see anomalously high loading ratios around 3.0 for #1, #2 and #3 runs, and still high values around 2.0 for reused samples. The PNZ2B sample has a tough life for D(H)-absorption and high heat release. It is a nice indication for industrial application of this CMNS effect in energy production/transfer systems. Observed maximum loading ratios showed similar values between the D-gas loading and the H-gas loading, so that we see no isotopic effect in final integrated loading.

In Fig.9, we show the data of Q1, mean released energy per a D(H)-atom sorption for the PNZ2B samples. The Q1 data correspond to the time-averaged η -values with heat-power weighting functions. The observed Q1 values for the D-gas charging have given “always” larger values than those for the H-gas charging. The excess values (differences) might be attributed to some nuclear effect caused by deuterons. The excess values are significant for the (3, 4)#3, the case of forced oxidation, and the (5, 6)#1, the first run of reused samples. These may be hints for further trials to

enhance the excess energy. The mean “chemical” binding energy is expected to be given by the data of the H-charging. We have had maximum value of 0.6eV by the (3, 4) #2 run and the minimum value in Fig.9 is 0.35eV. Probably, the sub-nano size structures on surface D(H)-adsorption sites are changing from run to run.

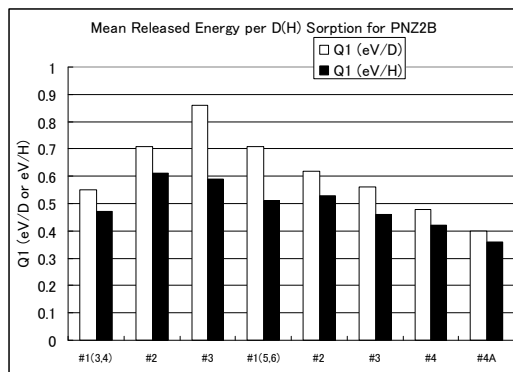


Fig.9: Data of mean released energy per a D(H)-atom sorption for the first series (3,4) runs and the reused series (5,6) runs of PNZ2B samples

3. Mesoscopic Catalyst and D-Cluster

In order to gain some understanding on what is going on in observed anomalies as summarized in Section-2, we extend⁴ here proposal of phenomenological models and related discussions.

In Fig.10, we illustrate a feature of making PZ and PNZ type samples.

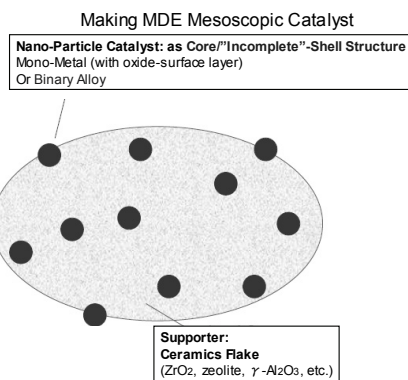


Fig.10: Illustrative feature of PZ and PNZ samples

Mono-metal (Pd in this case) nano-particles (1-10nm diameter in size) with PdO surface layer are dispersed in/on a flake of ceramics supporter (ZrO_2 in our case, and zeolite and gamma-alumina with

nano-pores in other group’s experiments). PdO/Pd nano-particles are replaced with binary nano-particles such as Pd_xNi_y “alloy” with $x+y=1.0$. It is known that binary alloys make a homogeneous lattice of regularly arranged positioning (lattice) of two different atoms. However, as known (see internet googling nano-catalyst) by recent development of nano-catalysts, binary nano-particle makes a outer-shell/inner-core structure and works as “nano-catalyst” because of large “fractal” surface with electron-dangling bonds. Our PdO/Pd nano-particle and Pd_xNi_y binary nano-particle (around 2nm diameter⁶) are supposed to work as nano-catalysts having the shell/core structure.

In Fig.11, we show schematic pictures of Pd_xNi_y binary nano-particles for the case a) of $x=2/8$ and $y=6/8$, which is corresponding to the PNZ-I sample, and the case b) of $X=1/8$ and $y=7/8$ which is corresponding to the PNZ2B sample.

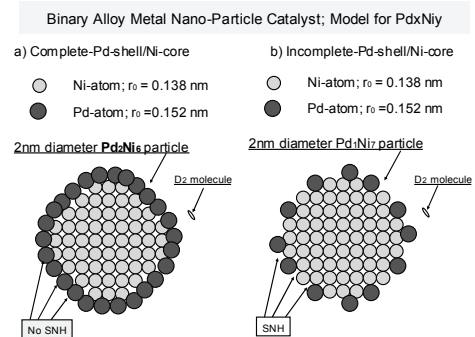


Fig.11: Illustration of Pd_xNi_y binary nano-particles having shell-core structure

In the case of a) complete-Pd-shell/Ni-core structure, incoming D_2 (or H_2) molecules will be trapped by dangling bonds of Pd-layer, dissociated into two D atoms and absorbed as making PdD state, which however blocks additional D_2 molecules to be trapped and in addition the formed PdD layer also blocks trapped deuterons diffusing into inner Ni-core-lattice (fcc structure as Pd). This feature may explain the loading and heat results obtained for the PNZ-I (10%Pd) sample, which does not work well.

In the case of b) “incomplete”-Pd-shell/Ni-core structure, many sub-nano-holes (SNH) can be formed on its surface as illustrated, where we expect

increased electron-dangling bonds to stick strongly incoming D₂ molecules to dissociate and diffuse into inner Ni core lattice. As we modeled the role of oxygen-atoms in PdO surface layer of PZ sample⁴, Pd ad-atoms of the incomplete outer shell have a role to generate SNHs for working as “mesoscopic catalyst”. In the case of PZ samples, we need to supplement oxygen after the #1 run for recovering as oxygen-atoms in PdO layer are gone away by the D(H)-charging. In contrast, Pd ad-atoms on the binary nano-particle remain and are active after the #1 run and revive fully by the forced de-oxidization. This is commonly the reason why PNZ2B samples worked still strongly for the reused series runs (5, 6).

As we have already discussed in Ref-4, the surface SNHs are seeds for making 4D/TSC transient Bose-Einstein condensates just from the beginning time of D-gas charging. The anomaly of η -values and their isotopic ratios in the beginning interval in Fig.2 can be explained by the 4D/TSC induced 4d-multi-body simultaneous fusion (break up to two alpha-particles after complex final state nuclear interactions), as causing 1watt-per-one-gram-Pd nano-particle nuclear heating by PZ samples⁴.

In the case of PNZ2B samples, we have observed gradually enhancing trend of η -values as shown in Figs. 4 and 5. We speculate that the anomalously high loading ratios exceeding 3.0 for PNZ2B samples would have suggested the D(H) trapping at T-sites (portion 2.0 of loading ratio) as well as O-sites (portion 1.0 of loading ratio) of Ni fcc local lattice of nano-Ni-core. Remaining component of over 3.0 loading ratio will be attributed to the trapped D-clusters at SNHs on the surface. Such anomalous occupation of T-sites by deuterons will enhance 4D/TSC formation inside Ni-core in the later time interval of Phase-I region and possible in the Phase-II region⁴.

An image of trapping potential of the mesoscopic catalyst is drawn in Fig.12. The left inserted figure illustrates the periodic Bloch trapping potential for the bulk Pd (same feature with larger valleys for bulk Ni). As we discussed already in our previous paper⁴, the mesoscopic global potential of meso-catalyst realizes anomalies in very rapid sorption, over-full-loading of D(H), anomalously large

“chemical” heat, chemical + nuclear combined heat evolution phenomena in the Phase-I interval, and possibly pure nuclear (maybe 4d fusion) heat evolution in the Phase-II region.

For conclusions, please see the abstract on the top.

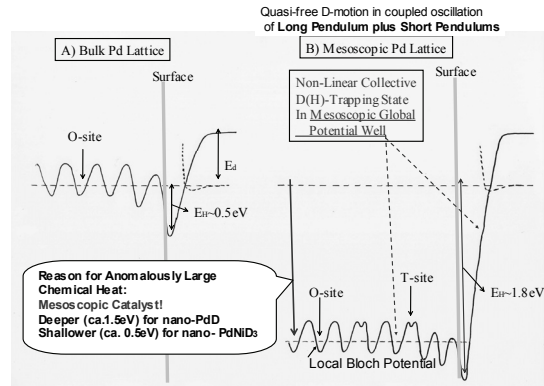


Fig.12: Illustration of mesoscopic global potential for PZ and PNZ type nano-particles

(Note: Proceedings paper for JCF11 Meeting, 11-12 December, 2010, Morioka, Japan: contact author; akito@stuv.zaq.ne.jp)

- 1) A. Kitamura, T. Nohmi, Y. Sasaki, A. Taniike, A. Takahashi, R. Seto, Y. Fujita: *Physics Letters A*, 373 (2009) 3109-3112
- 2) Akira Kitamura, Akito Takahashi, Yu Sasaki, Yuki Miyoshi, Akira Taniike, Reiko Seto and Yushi Fujita: “Heat Evolution from Pd Nanopowders Exposed to High-Pressure Hydrogen Isotopes and Associated Radiation Measurements”, J. Marwan Ed., *JCMNS*, Vol.5, to be appeared in 2011
- 3) Akira Kitamura, Akito Takahashi, Yu Sasaki, Yuki Miyoshi, Akira Taniike, Reiko Seto and Yushi Fujita: “Anomalous Heat Evolution in Charging of Pd Powders with Hydrogen Isotopes”, J. Marwan Ed., *LENR NET Sourcebook Vol.3*, American Chemical Society, to be published in 2010
- 4) A. Takahashi, A. Kitamura, Y. Sasaki, Y. Miyoshi, A. Taniike, R. Seto and Y. Fujita: Role of PdO Surface-Coating in CMNE D(H)-Gas Loading Experiments, Proceedings of 9th Workshop on Anomalies in D(H)-loaded Metals, 16-19 September 2010, Siena, Italy (to be published in *JCMNS* Vol.4, 2011) (see also the paper by A. Takahashi et al., *Proceedings JCF10*, pp.46-53, 2010, JCFRS)
- 5) Y. Miyoshi, H. Sakoh, A. Taniike, A. Kitamura, A. Takahashi, R. Seto and Y. Fujita: this proceedings
- 6) H. Sakoh, Y. Miyoshi, H. Sakoh, A. Taniike, A. Kitamura, A. Takahashi, R. Seto and Y. Fujita : this proceedings

Brief Explanation of Experimental Data Set on Excess Heat and Nuclear Transmutation in Multiplly Nanocoated Ni Wire

Hideo Kozima¹⁾ and Francesco Celani²⁾

- 1) Cold Fusion Research Laboratory, 597-16, Yatsu, Aoi, Shizuoka 421-1202, Japan
- 2) Istit. Naz. Fis. Nucl., Lab. Naz. Frascati, Via E. Fermi 40, 00044 Frascati, Italy

Abstract

Experimental data of excess heat generation and nuclear transmutation obtained in Ni wire multiply nano-coated with Pd and a compound of B, Sr, Ba and Th at up to 900 degC have been analyzed using the TNCF model.

The Ni wire is 50 μ m in diameter and 82 cm long. The coating is made of Pd and the compound about 50 times resulting in a surface layer of about one μ m thick. The maximum excess energy Q_{\max} is 1800 W/g of the Ni wire. There have occurred various nuclear transmutations. The most notable results are enumerated as follows: (1) Elements Ti, Cr, Co, As, Ir, and Tl have increased. (2) B, Sr, Pd and Ba have decreased. (3) Fe and Ni have not showed remarkable change. (4) In the case of B, Sr and Ba, the rates of the decrease are larger for lighter isotopes. (5) $^{10}\text{B}/^{11}\text{B}$ ratio decreased over 14%. (6) ^{105}Pd decreased about 5% and ^{102}Pd increased about 9%.

These data have been analyzed using the TNCF model successfully applied for explanation of various experimental data sets over the past 15 years. We can estimate the parameter of the model n_n using the data for ^{10}B and ^{105}Pd as follows; $n_n = 1.3 \times 10^9 \text{ cm}^{-3}$ (by the decrease of ^{10}B) and $n_n = 2.5 \times 10^{11} \text{ cm}^{-3}$ (by the decrease of ^{105}Pd). These values show the situation in the experiment belong to a range of fairly large value of the parameter where we can expect the nuclear reactions by a single neutron and also a n-p cluster.

The excess heat generation of 1800 W/g at its maximum has been investigated using the value of n_n estimated above and a formula for the excess energy is induced. Assuming the surface layer of 1 μ m thick is made of Pd only, for illustrative purposes, we have obtained Q_{av} about 1% of the observed maximum one. If the average value of the excess energy is about 10% of the maximum, the discrepancy is about one order of magnitude. If we know the correct composition of the surface layer, the calculated value of Q_{av} will increase a little.

The nuclear transmutation of several elements confirmed by the experiment is qualitatively explained assuming the single neutron absorption by elements in the surface layer. The decrease of Ru might be explained by a single n-p cluster absorption.

Keywords: Cold Fusion Phenomenon, Ni Wire, Nuclear Transmutation, Excess Heat, Nanocoating

1. Introduction

The cold fusion phenomenon (CFP), i.e. low energy nuclear reactions in solids with high density hydrogen isotopes at near room-temperature in a non-equilibrium condition including ambient

radiations, has been observed in various materials composed of mainly transition metals and hydrogen isotopes. The phenomenon is characterized by extraordinary excess energy inexplicable by ordinary

chemical and physical processes possible to occur in systems at temperatures around ordinary environment without specific acceleration mechanism. This is the reason some nuclear reactions should be relevant to the cause of the CFP. Based on the experimental data sets obtained until now, the nuclear reactions in CF materials are supposed to occur at boundary regions between a host material (e.g. NiH_x wire) and a guest material (e.g. layer composed of multiply coated nano-films of Pd and (B, Sr, Ba, Th) compound). The guest material is formed automatically in the surface/boundary regions of a host material unintentionally on the surface of cathode in an electrolytic experiment or on the surface of electrode in a plasma discharge experiment [1 – 2]. In some experiments, the guest material is intentionally formed on the host material by artificial manner; coating alien elements on a metal surface or depositing elements on a cathode surface. There are such several examples of artificially formed guest materials as those of Yamaguchi [3], Patterson [4], Szpak [5], Iwamura [6], Celani [7] among others.

The different role of the host and guest materials is speculated as follows from our point of view. The role of the host material (NiH_x , PdD_x , TiD_x , - - -) composed of an interlaced lattices of host metal and occluded hydrogen isotope is to form the cf-matter with a dense neutron liquid.

On the other hand, the guest material composed of irregular array of elements gives an active region for the nuclear reaction resulting in the cold fusion phenomenon (CFP). The neutron Bloch wave in the host material reacts with alien nuclei disturbing regularity of the host material. This is the reason that the nuclear reaction occurs at surface/boundary regions of the host and a guest material.

The alien nuclei in the guest material become agents of the nuclear reactions resulting in the cold fusion phenomenon, i.e. nuclear reactions in transition-metal hydrides and deuterides in ambient radiation at room temperature or at even higher temperatures.

The interesting experimental data obtained in multiply nanocoated Ni wire are investigated from this point of view to give qualitative and semi-quantitative explanation of their typical results.

2. Experimental

In the experiment by Celani et al. [7], the sample is a Ni wire ($\phi = 50 \mu\text{m}$ and length of 82 cm, mass of 14 mg) multiply nano-coated (final thickness $\approx 1 \mu\text{m}$) by Pd and a compound including B, Sr, Ba, and Th by 50 times successive coating. A schematic section of the nanocoated Ni wire is shown in Fig. 1. We can see the system as composed of two parts; the central part is consist of NiH_x forming the host material of the system and the outer part is consist of stratified fifty thin layers of different components including Pd, B, Sr, Ba, Th, H (D). In several experiments to the active gas (H_2 and/or D_2) was added Ar (20-50%) in order to decrease the thermal conductivity and, as consequence, increase the wire temperature at a constant applied electrical power.

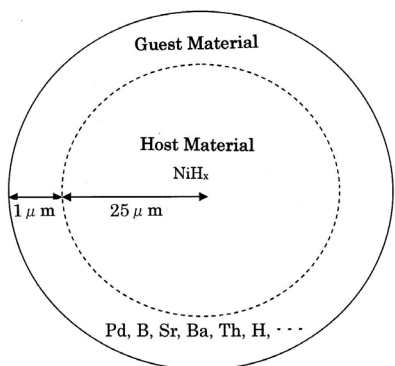


Fig. 1 Schematic cross section of the multiply nanocoated Ni wire.

The Ni wire nanocoated, after several loading-delocalizing and thermal high temperatures cycles, at very high temperatures (900°C) and under electromigration current of the order of 40–45 kA/cm², showed an excess power, in respect to a similar “virgin” wire with the same applied power (148W), of about 26W. The (main) gas atmosphere was hydrogen added of argon (ratio 60/40) at a pressure of 6 atm at room temperature.

Some compositional and isotopic anomalies were detected by PIXE and ICP-MS analysis. Some of them are so large that it is difficult to think they can arise

from systematic or statistic errors. As a general trend, by ICP-MS analysis, in the case of elements with several isotopes (B, Sr, Ba), the rate of decreasing is larger for lighter isotopes. Such effect is clearly evident with B₁₀/B₁₁ ratio: it decreased of over 14%. A special situation happened for Pd coating: it seems reduced (about 5%) Mass 105 (isotopic abundance 22.3%) and largely (about 9%) increased Mass 102 (isotopic abundance 1%).

In Fig.2 are shown the results of analysis by PIXE [7].

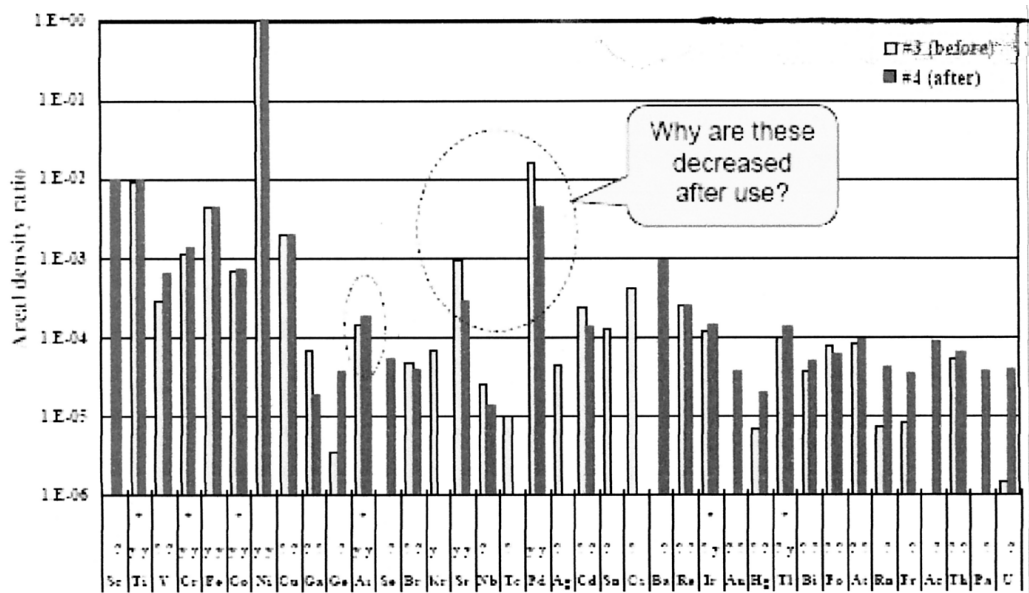


Fig. 2 Change of elemental composition before and after H₂ gas loading by PIXE.

3. Theoretical investigation

According to the recipe of the TNCF model [Kozima Development, Science,], excess energy and nuclear products may be generated by all nuclear reactions occurring in the sample as a whole, mainly in the guest material.

3.1 Nuclear Reactions between Trapped Neutrons and Nuclei in the Guest Material

The trapped neutron in the TNCF model exists in the host material and its density is vastly intensified at surface/boundary regions where is the guest materials. Number N_{nX} of nuclear transmutation (NT) of a nucleus X by absorption of a neutron in the TNCF model;

$$N_{nX} = 0.35 n_n v_n n_X \sigma_{nX} V \tau \quad (1)$$

where n_n and v_n are the number density and thermal

velocity of the trapped neutrons in the model, n_X is the number density of the nucleus X in the active volume V where the transmutation occurs in a time τ , and σ_{nX} is the absorption cross section of a thermal neutron by the nucleus X ([1] Section 11.1, [2] Sec. 3.2).

It should be noticed at first that we have determined the parameters n_n using many experimental data sets and tabulated them in Tables 11.2 and 11.3 of [1] (and Tables 2.2 and 2.3 of [2]). The values have been determined as tabulated there and are in the range 10^8 to 10^{11} cm^{-3} .

Numerical values in the equation (1):

$$v_n = 2.20 \times 10^5 \text{ cm/s (at room temperature)}$$

$$n_{\text{Pd}} = 6.88 \times 10^{22} \text{ cm}^{-3} \text{ (assuming Pd lattice)}$$

$\sigma_{n\text{Pd}105} = 2.025 \times 10 \text{ b} = 2.025 \times 10^{-23} \text{ cm}^2$ (for ^{105}Pd and thermal neutron)

$\sigma_{n\text{B}10} = 3.837 \times 10^3 \text{ b} = 3.837 \times 10^{-21} \text{ cm}^2$ (for ^{10}B and thermal neutron)

The cross sections of neutron capture increase, like $1/E$ in log-log scale, at lower energies. In principle, the energy of neutron can be even lower than thermal.

The Eq. (2.1) for the number of reactions in a volume V and time τ is rewritten as follows to make the meaning of each term clearer;

$$N_{nX} = (0.35n_n v_n)(n_X \sigma_{nX})(V\tau). \quad (2)$$

The quantity in the first bracket relates to the cf-matter in the host material, the second to the agent element X, the third to the experimental condition. The relevant quantity of the isotope ^A_ZX of an element X in the sample is $\rho_{XA}\sigma_{XA}$ where ρ_{XA} is the abundance in percent and σ_{XA} is the cross section for a neutron absorption of the isotope ^A_ZX . If we know the density n_X of the element X in the sample, we obtain the relevant quantity $(n_X \sigma_{nX})$ of the element X in Eq. (2) by summing up $\rho_{XA}\sigma_{XA}$ over A and multiplying by n_X ;

$$N_{nX} = (0.35n_n v_n) n_X \sum_A \rho_{XA} \sigma_{XA} V\tau. \quad (3)$$

To calculate excess heat generated by nuclear reactions in the sample, we need another modification of the equation. If a reaction between a thermal neutron and a nucleus X generate excess energy q_X , the total excess energy Q_X in a unit volume and unit time is given by the number N_{nX} of reactions in the volume V and time τ multiplied by q_X and divided by $V\tau$;

$$Q_X = Q_X(V, \tau) / V\tau = N_{nX} q_X. \quad (4)$$

When there are isotopes ^A_ZX of the element X with abundance ρ_{XA} , the corresponding energy Q_A by an isotope ^A_ZX generating q_{XA} is given as follows;

$$Q_A = 0.35n_n v_n n_X \rho_{XA} \sigma_{XA} q_{XA}$$

And then, the total energy Q_X by the element X with a density n_X in a unit volume and time is given by a summation of Q_A over A ;

$$Q_X = \sum_A Q_A = 0.35n_n v_n n_X \sum_A \rho_{XA} \sigma_{XA} q_{XA}. \quad (5)$$

If there are several agent nuclei X, X', - - - in the active region, the total excess energy Q generated in a sample in unit volume and time is given by summation of the Q_X over X;

$$Q = \sum_X Q_X = 0.35n_n v_n \sum_X n_X \sum_A \rho_{XA} \sigma_{XA} q_{XA}. \quad (6)$$

3.2 Explanation of Experimental Data by the TNCF Model

Qualitative explanation of experimental facts explained in Section 2 is naturally deduced from the characteristics of the TNCF model. Brief explanation is given as follows.

3.2.1 Decrease of B_{10}/B_{11} ratio and $^{105}_{46}\text{Pd}$.

The change of a nucleus ^A_ZX of an element X is governed by a quantity $(n_X \sigma_{nX})$ of Eq. (3). Looking into the table of nuclei, we know this quantity $(n_X \sigma_{nX})$ for $^{10}_5\text{B}$ (B_{10}) and $^{105}_{46}\text{Pd}$ is very large compared to other isotopes of these elements; 7.59×10^3 and 4.522 , respectively. The larger the value $(n_X \sigma_{nX})$ of a nucleus

${}^A_Z X$ is, the more nuclei transmute to the isotope with a higher mass number ${}^{A+1}_Z X$. Therefore, ${}^{10}_5 B$ and ${}^{105}_{46} Pd$ decrease remarkably compared to other isotopes.

The decrease of ${}^{105}_{46} Pd$ by 5% in one month is used to calculate the parameter n_n in Eq. (1) to give the value for this case;

$$n_n = 2.5 \times 10^{11} \text{ cm}^{-3}. \quad (7)$$

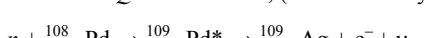
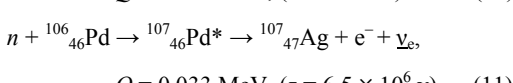
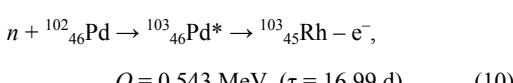
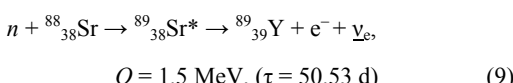
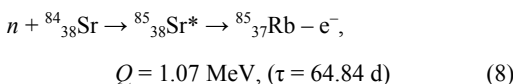
This value is in the upper level of n_n determined hitherto and we may expect occurrence of nuclear reactions mediated by the neutron-proton cluster ${}^4_2 \delta$ even in this system.

3.2.2 General Tendency of Isotope Change

It is noticed that the rate of decreasing is larger for lighter isotopes in the case of elements with several isotopes (B, Sr, Ba). This tendency is explained by the same reasoning given above for the decrease of ${}^{10}_5 B$ and ${}^{105}_{46} Pd$. The nuclear transmutation governed by the quantity $(n_X \sigma_{nX})$ shifts isotopes to the ones with a higher mass number by one.

3.2.3 Decrease of Sr and Pd, and increase of As.

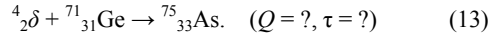
Looking into the table of isotopes, we notice that Sr and Pd have many isotopes which decay into other elements after absorption of single neutron. For instance, we can write down several such reactions as follows;



$$Q = 1.12 \text{ MeV}, (\tau = 13.7 \text{ h}) \quad (12)$$

These examples show clearly possible decrease of Sr and Pd by the mechanism of single neutron absorption followed by decay to another element.

On the other hand, the increase of As is explained by absorption of a neutron-proton cluster ${}^4_2 \delta$ even if the decrease of Ge is not confirmed in the experiment;



3.2.4 Excess Energy Generation

The reaction equations (7) – (11) give us possible source of excess energy by nuclear reactions between agent nuclei in the guest material and the trapped neutrons. Summing up excess energy generated in possible reactions, we can calculate total excess energy produced in the sample by the assumed mechanism of the TNCF model. The effectiveness of the model will be justified by successive explanation of the nuclear transmutation and excess energy generation adjusting the single parameter n_n .

The excess energy is expressed as follows in this model for a guest material composed of Pd, Ni, B, Sr, Ba, Th, H and Ar;

$$Q (\text{MeV}) = 0.77 \times 10^5 n_n \times [0.05 n_B + 0.01 n_{Sr} + 0.62 n_{Ba} + 49.65 n_{Th} + 2.67 n_{Pd} + 3.67 n_{Ni} + (0.737 \rho_1 + 3.44 \times 10^{-3} \rho_2) n_H + 1.63 n_{Ar}] \times 10^{-24}. \quad (14)$$

n_X is the number density in cm^{-3} of an element X, and ρ_1 and ρ_2 are ratios of protium and deuterium in the guest material, respectively.

Illustrative calculation of this value Q for a surface layer, or a guest material, on the Ni wire is made for a hypothetical composition PdH and the value of n_n given in Eq. (9). The result is given as

$$Q_{th} = 0.09 \text{ W} \quad (15)$$

for the sample with the same size used in the

experiment [7]. This value should be taken as an average value of the excess energy expected in the hypothetical system with the same sample size to the one in the experiment [7].

The maximum excess energy measured in the experiment is rewritten as follows;

$$Q_{\text{ex, max}} = 25.2 \text{ W.} \quad (16)$$

If we know the average value of the excess energy observed in the experiment, the comparison becomes more meaningful. It may be possible to assume the average value is one order of magnitude smaller than the maximum (16). In the theoretical formula (14), there are several effective terms for the excess energy production such as the terms by Ba, Th, Ni and ^1H in addition to that of Pd. Considering these possible contributions to the excess energy, the value given in Eq. (15) will be increased by a factor of one order of magnitude.

4. Conclusion and Discussion

The analysis briefly explained in this paper gives consistent explanation of the experimental data [7] in themselves and also consistent with other experimental data sets obtained since 1989 and explained with our model [1, 2]. Further, specific experiments and more detailed elemental analysis are needed for a conclusive understanding/explanation of the phenomena.

It will be useful to plan novel experiments considering relations of several observables a part of which described in this paper. The science of the cold fusion phenomenon should be established on systematic data sets in physics, chemistry and catalytic chemistry of materials exhibiting wonderful events inexplicable by conventional knowledge.

References

- 1 H. Kozima, *Discovery of the Cold Fusion Phenomenon* (Ohtake Shuppan Inc., 1998). ISBN 4-87186-044-2.
2. H. Kozima, *The Science of the Cold Fusion Phenomenon*, Elsevier Science, 2006. ISBN-10: 0-08-045110-1.
3. E. Yamaguchi and T. Nishioka, "Direct Evidence for Nuclear Fusion Reactions in Deuterated Palladium," *Proc. ICCF3* (October 21 - 25, 1992, Nagoya, Japan), pp. 179 – 188 (1993), Universal Academic Press, Tokyo, Japan, 1993.
4. Patterson G.H. Miley and J.A. Patterson, "Nuclear Transmutations in Thin-film Nickel Coatings undergoing Electrolysis," *J. New Energy* 1-3, pp. 5 – 34 (1996).
5. Szpak S. Szpak, P.A. Mosier-Boss, and M. H. Miles, "Calorimetry of the Pd + D Codeposition," *Fusion Technol.*, **36** (1999) 234-241.
- 6 Y. Iwamura, T. Itoh, M. Sakano and S. Sakai, "Observation of Low Energy Nuclear Reactions induced by D_2 Gas Permeation through Pd Complexes," *Proc. ICCF9* (2002, Beijing, China), pp. 141 – 146 (2005).
- 7 F. Celani, P. Marini, V. Di Stefano, M. Nakamura, O.M. Calamai, A. Spallone. A. Nuvoli, E. Purchi, V. Andreassi, B. Ortenzi, E. Righi, G. Trenta, A. Mancini, A. Takahashi and A. Kitamura, "First measurement on Nano-coated Ni Wire, at Very High Temperature, under He, Ar, H_2 , D_2 Atmosphere and Their Mixtures," Paper presented at 9th International Workshop on Anomalies in Hydrogen/Deuterium Loaded Metals (Certosa di Pontignano, Siena-Italy; Sept. 17 – 19, 2010).

Localization of Nuclear Reactions in the Cold Fusion Phenomenon

Hideo Kozima,

Cold Fusion Research Laboratory, 597-16 Yatsu, Aoi, Shizuoka, Shizuoka 421-1202, Japan

Abstract

One of the characteristics of the cold fusion phenomenon (CFP), i.e. low energy nuclear reactions in solids with high density hydrogen isotopes at near room-temperature in ambient radiations, is the localization of nuclear reactions relevant to the phenomenon. The earliest data sets showing the localization of nuclear reactions were given by Iyengar and Srinivasan (1989, 1990) for product tritium localized in spots (fraction of a millimeter or less in size) at surfaces of a Ti sample. Morrey et al. (1990) reported ${}^4_2\text{He}$ in surface layers of Pd with a width of about 25 μm . Okamoto et al. (1994) observed nuclear transmutation of minor elements in surface layers of Pd samples, especially ${}^{27}_{13}\text{Al}$ into ${}^{28}_{14}\text{Si}$, in a layer of about 2 μm . Miley et al. (1996) observed various transmutation products, especially transmutation of ${}^A_{28}\text{Ni}$ isotopes, in the thin Ni layer of width about 0.1 μm in a protium system. Mizuno et al. (1996) also observed similar nuclear transmutations in PdD_x and AuH_x systems. Iwamura et al. (2002, 2005) observed transmutations of Sr, Cs and Ba into Mo, Pr and Sm, respectively, in/on a Pd surface layer of thickness about 10 nm (100 Å). Furthermore, the second product confirmed its spatial localization with a diametrical size of about 100 μm . Thus, we know that the reaction products of the CFP are localized in regions at surface layers about a few μm in width of massive CF materials and also in thin CF materials with layer structures of widths less than one μm .

The confinement of nuclear reactions in surface/boundary layers of a few μm might be a characteristic of the CFP in protium and deuterium systems. This characteristic of the CFP is explained by the structure of a CF material composed of (1) a host material composed of a metal and a hydrogen isotope and (2) a guest material including agents for the CFP on the surface of the former. The localization of nuclear reactions in the guest material in spot-like regions is another characteristic showing nuclear reactions between the agent (such specific nuclei as alien nuclei (Li, Sr, Cs) or the irregularity of atomic arrays). These characteristics of localized nuclear reactions are investigated quantum mechanically using properties of nucleus and proton/deuteron wavefunctions in the CF material.

Keywords: Cold Fusion Phenomenon, Nuclear Reaction, Localization

1. Introduction

To make people recognize importance of the controversial research fields like the cold fusion phenomenon that they have not known well about the details of experimental data in it, it is necessary to arrange experimental data sets along lines easy to understand the complexity of the data. One of

characteristics of the cold fusion phenomenon (CFP), i.e. phenomenon composed of nuclear reactions in complex solid materials containing a lot of hydrogen isotopes in a non-equilibrium condition including ambient radiations, is the localization of reactions revealed by transmuted nuclei in surface or boundary layers with a width of about a few micrometer (1 μm =

10^{-4} cm). The localization of the transmuted nuclei is one of the direct evidences of nuclear reactions in the CFP ([1.1], Section 2.2.1.1). If we are able to understand the cause of this localization in terms of common senses of the modern science, it is helpful to make the phenomenon recognized as an object of science and also to investigate the CFP as a part of modern science in interdisciplinary field among nuclear physics, solid-state physics and catalytic chemistry.

There are many experimental data sets showing the surface nature of nuclear reactions in the CFP observed from the year of 1989 and increasing the number and accuracy of measurements until now. The first confirmation of the locality of the phenomenon may be the paper by Morrey et al. [1.2] observing He atoms in the surface layer of width about $25\mu\text{m}$ of the Pd sample in which excess heat was observed. Iyengar and Srinivasan et al. [1.3, 1.4] observed tritium localized in spots (fraction of a millimeter or less in size) at surfaces of Ti samples. Following these pioneering works, there have reported various data sets showing localization of nuclear products in surface layers of massive CF materials [1.5 – 1.15] and also in several layer structures with width less than $1\mu\text{m}$ [1.16 – 1.29].

The localization of nuclear products should be investigated as it is and also in relation to other events in the CFP to clarify the mechanisms realizing the wonderful events of the CFP.

In this paper, we give an approach to the unified explanation of the localization of nuclear emission sources, ${}^4_2\text{He}$ generation and nuclear transmutations in the CFP using a phenomenological model and a quantal approach to the mechanism of nuclear reactions in CF materials.

2. The Trapped Neutron Catalyzed Fusion

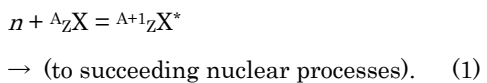
(TNCF) Model and Experimental Data Sets

The TNCF model proposed by us [2.1] and extended later to explain nuclear transmutations with the large changes of mass and proton numbers [1.1] is used to explain nuclear transmutations observed in localized regions in this section. From experimental facts, we assume materials where occurs the cold fusion phenomenon (CFP) are divided into two regions. (1) The first is the **host material** composed of interlaced lattices of (a) Pd, Ti, Ni, C, or several other elements and (b) protium or deuterium. (2) The second is the **guest material** composed of elements placed in the surface or boundary regions of the host material with different regularity from the first.

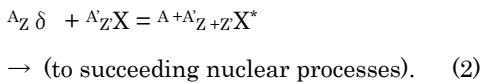
The key assumption of the model is the existence of the so-called trapped neutrons in the host material in a neutron band. The **neutron Bloch waves** in the band are reflected at the boundary of the host and guest materials making accumulation of Bloch waves. The accumulation makes the density of the trapped neutron at the boundary region very high as $10^8 - 10^{11}\text{ cm}^{-3}$.

The model assumes three types of nuclear reactions between the trapped neutron and a nucleus ${}^A_Z\text{X}$ placed in the guest material out of phase of the lattice of the host material:

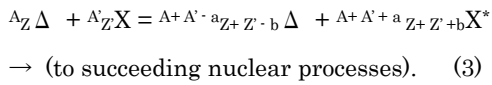
1. Absorption of single neutron by a nucleus ${}^A_Z\text{X}$ followed by a disintegration of ${}^{A+1}_Z\text{X}^*$:



2. Absorption of a neutron-proton cluster ${}^A_Z\delta$ by a nucleus ${}^A_Z\text{X}$:



3. Nuclear interaction between a neutron drop ${}^A_Z\Delta$ and a nucleus ${}^A_Z\text{X}$:



The neutron cluster ${}^A_Z \delta$ and neutron drop ${}^A_Z \Delta$ are assumed to be composed of Z protons and $(A - Z)$ neutrons. The difference is only the number of nucleons in them; A is supposed to be less than 10 in the cluster and larger than or equal to 10 in the drop.

2.1 Data by Morrey et al. [1.2]

The first evidence of locality of nuclear reactions was observed by Morrey et al. [1.2] when they tried to check generation of ${}^4_2 He$ in PdD_x samples that had shown excess heat by Fleischmann et al. [2.2]. They have observed ${}^4_2 He$ in the surface layer of width $40 \mu m$ of the sample with an amount incompatible with the excess heat reportedly observed in the same sample. The discrepancy was resolved by our consideration of the mechanism catalyzed by a trapped neutron between ${}^6_3 Li$ nucleus at the surface producing excess heat and ${}^4_2 He$ by a phenomenological model [2.1, Section 11.8].

2.2 Data obtained in BARC (Bhabha Atomic Research Center) in India [1.3, 1.4]

Localization of tritium in TiD_x was observed by a group in BARC (Bhabha Atomic Research Center) in India [1.3, 1.4]. They concluded that tritium is invariably concentrated in highly localized spots (fraction of a millimeter or less in size) each containing typically about 10^{12} to 10^{14} atoms (2 to 200 kBq) of tritium. In addition to the localization of the product tritium, they observed a high ratio N_t/N_n of tritium to neutron as $10^6 - 10^9$ ($N_t/N_n|_{ex} \sim 10^6 - 10^9$).

The large imbalance in production rates of tritium and neutron has been explained by a mechanism occurring in the CF material by the TNCF model [1.1,

2.1, 2.3] which predicts the ratio of about 10^7 ($N_t/N_n|_{th} \sim 10^7$).

2.3 Data by Dash et al. [1.5, 1.6]

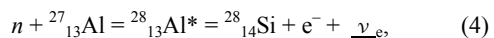
Surface morphology and change of elements in the surface layer of PdD_x samples have been investigated by Dash et al.

The changes of isotope ratios of Ti and Pd observed by them have been qualitatively explained by the TNCF model ([1.1] Appendix C7, [2.4]). The cause of high temperature at the surface region resulting in the complex morphology observed by Dash et al. has been investigated using the TNCF model. The same investigation will be applied to the hot spots containing tritium about 10^{12} to 10^{14} atoms observed by Iyengar et al [1.3].

It is interesting to note their result [1.6] that the excess heat generation does not occur when H₂SO₄ is replaced by D₂SO₄ in the Pd/D₂O + H₂SO₄ system. This point will be discussed elsewhere [2.5].

2.4. Data by Okamoto et al. [1.7]

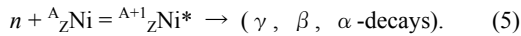
The data by Okamoto et al. obtained in a Pd/D₂O+LiOD/Pt system was successfully analyzed by the single neutron absorption mechanism of the TNCF model. The result explains the observed decrease of Al and increase of Si by the following reactions;



where $\bar{\nu}_e$ is the electron neutrino.

2.5. Data by Miley et al. [1.16, 1.17]

The data of nuclear transmutation observed by Miley et al. [1.16, 1.17] in beads (microspheres) of polystyrene core plated with thin ($\sim 1 \mu m$) metal films of Cu, Ni and/or Pd on the surface [1.18] were analyzed by the TNCF model with a single neutron absorption followed by a decay depending on the intermediate excited nucleus:



The resultant ratio of nickel isotopes ${}^A_Z \text{Ni}$ ($A = 59, 63$ and 65) is compared with the experimental result as follows:

$$(N_{59} : N_{63} : N_{65})_{\text{ex}} = 1 : 0.27 : 0.12. \quad (6)$$

$$(N_{59} : N_{63} : N_{65})_{\text{th}} = 1 : 0.17 : 5.73 \times 10^{-3}. \quad (7)$$

On the other hand, the excess heat expected from the assumed nuclear reactions is compared with the experimental result assuming that the liberated energy was totally thermalized in the system;

$$P_{\text{ex}} = 0.5 \pm 0.4 \text{ W}. \quad (8)$$

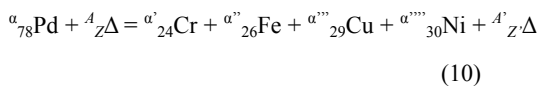
$$P_{\text{th}} = 0.12 \text{ W}. \quad (9)$$

We may conclude that the coincidence of the theoretical and the experimental results is fairly good.

From their figures showing profiles of newly generated elements in PdD_x system, we cite here those for isotopes of chromium (Cr) [1.10].

The elements produced in the surface region of Pd samples includes light nuclei (O, C, Ca, Na, Mg and Al) and heavy nuclei (Cr, Fe, Cu, Zn, Br, Xe, Cd, Hf, Re, Pt, Ir and Hg) and the shifts of isotopic abundances from natural ones are small in the former and large in the latter.

A possible explanation of the reactions to generate those various elements, especially the heavy nuclei, is given by the nuclear reactions (2.3) catalyzed by the neutron drops ${}^A_Z \Delta$. An example of possible nuclear reactions mediated by the neutron drops ${}^A_Z \Delta$ in the cf-matter formed at around surface region are written down as follows ($\alpha = 190 - 198$);



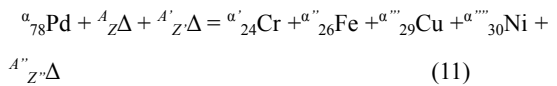
when $\alpha = 102 - 110$, $\alpha + A = \alpha' + \alpha'' + \alpha''' + \alpha'''' + A'$, $78 + Z = 24 + 26 + 29 + 30 + Z'$.

Another possible reaction may be that with two neutron drops as follows;

The other various products such as Fe, Si, Mg, Cu, Cr, Zn, and Ag should be explained by the use of the reactions (2.3) catalyzed by neutron drops. Some of these cases are given in the next subsection.

2.6 Data by Mizuno et al. [1.9 – 1.12]

Mizuno et al. and Ohmori et al. have made various excellent experiments on the protium and deuterium systems with Au, W, Pt, Pd and Ni cathodes and have reported the results in many papers including ones cited in this paper [1.9 – 1.12]. Localization of nuclear transmutation products at surface regions has been determined in addition to the change of surface morphology.

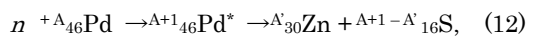


with $\alpha + A + A' = \alpha' + \alpha'' + \alpha''' + \alpha'''' + A''$, $78 + Z + Z' = 24 + 26 + 29 + 30 + Z''$.

2.7 Data by Qiao et al. [1.13]

Qiao et al. [1.13] made an experiment of excess heat and nuclear transmutation on a Pd wire with a diameter $340 \mu\text{m}$ deuterated by the gas contact method. After one year of loading and de-loading process, they measured the element composition of the sample at six points.

The data of Zn are analyzed by the NT with the single neutron absorption followed by a fission. The probable reaction inducing the transmutation of Pd into Zn is written down as follows assuming a fission reaction:



with $A = 102 - 110$ and $A' = 64 - 70$ for stable isotopes and therefore

$$A + 1 - A' \equiv A'' \geq 33. \quad (13)$$

The cross section σ for the absorption

reaction in the above reaction ranges from 0.2 to 20 barns; $\sigma = 3.36, 0.52, 20.25, 0.30, 8.50$ and 0.23 barns for $A = 102, 104, 105, 106, 108$ and 110 , respectively. Assuming the intermediate nucleus $^{A+1}_{46}\text{Pd}^*$ in the above reaction is unstable and decays by and by into Zn and S, we can calculate the number of Zn atoms N_{Zn} generated in a time τ as a function of the density of the trapped neutron n_{n} by the following relation according to our recipe of our model [1.1, 2.1, 2.3]:

$$N_{\text{Zn}} = 0.35 n_{\text{n}} v_{\text{n}} n_{\text{Pd}} V \tau \sum_A \sigma_A p_A \xi, \quad (14)$$

where v_{n} is the thermal velocity of the trapped neutron, n_{Pd} is the density of palladium, p_A (in %) is the natural abundance of a Pd isotope with mass number A , σ_A is the absorption cross section of the above reaction for a mass number A and V is the volume of the sample. \sum_A means a summation on A and ξ is the factor to show the degree of instability of the trapped neutron and assumed to be 1 at boundary region in our model.

Using an average value $N_{\text{Zn}} = 4.065 \times 10^{-3} n_{\text{Pd}}$ V of the experimental data at Points 1 to 4 generated in $\tau = 1 \text{ y}$ ($= 3.15 \times 10^7 \text{ s}$) and $V = (1.7^2 - 1.3^2) \times 10^{-4} \text{ cm}^3 = 1.2 \times 10^{-4} \text{ cm}^3$ per unit length of the Pd wire, we obtain the parameter n_{n} as follows ($\xi = 1$ is assumed);

$$n_{\text{n}} = 9.9 \times 10^8 \text{ cm}^{-3}, \quad (15)$$

which is in the lower range of values determined for other experimental data sets [2.2].

Many of the isotopes of sulfur (S) generated finally in the above reaction have β -decay modes and generate chlorine (Cl) or finally argon (Ar) which are gaseous and not expected to remain in the sample to be detected there.

The excess heat accompanied with the fission

generating Zn is estimated taking only the predominant modes in the above reaction and is $Q_{\text{th}} \approx 0.5 \text{ W}$. This value of excess heat is compared with the value $Q_{\text{ex}} = 0.82 \text{ W}$ obtained by them (cf. [2.1] Section 11.12d, [2.6]).

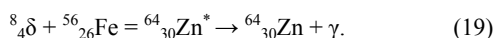
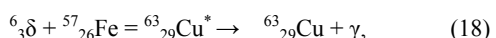
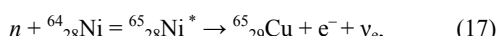
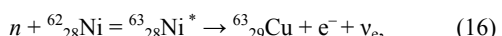
2.8 Data by Campali et al. [1.14, 1.15]

Campali et al. [1.14, 1.15] investigated photon and particle emission, heat production and surface transmutation in the Ni-H system loaded by gas contact with cylindrical and planar samples of pure Ni and Ni alloy ($\text{Ni}_{7.6}\text{Cr}_{20.6}\text{Fe}_{70.4}\text{Mn}_{1.4}$). Their results give us another interesting example of the CFP in protium systems with identification of the place where occur nuclear reactions resulting in transmutations at the sample surface.

New elements between C and Zn were observed after same months of heat production, the concentrations of which depended on the position.

The concentrations of the new elements Cu and Zn varied along the rod surface of the Ni alloy sample.

The mechanism of Cu and Zn formation in this case may be the single neutron and neutron-proton cluster absorptions followed by decay processes. Several examples of the reaction are written down as follows [1.1 (Section 2.5), 2.1 (Section 11.11)];

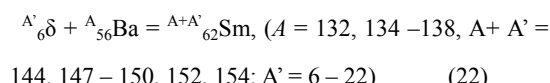
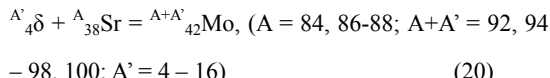


2.9 Data by Iwamura et al. [1.19 – 1.23]

The interesting experimental data sets obtained by Iwamura et al. [1.19 – 1.23] give us information about the local nature of the nuclear transmutation and also a

phase of neutron-nucleus interactions in the CFP, the absorption of a neutron-proton cluster by a nucleus. They used a specific structure called “Pd complex.”

After adding alien elements Cs, Sr or Ba on the surface, D₂ gas was permeated through this structure, they investigated the surface of the complex and found nuclear transmutations of elements Cs to Pr, Sr to Mo and ^A₅₆Ba to ^{A+12}₆₂Sm. This results have clearly demonstrated the nuclear reactions catalyzed by neutron-proton clusters ⁸₄δ and ¹²₆δ that were already assumed before to explain nuclear transmutations (NTs) observed in deuterium and protium systems [1.2, 2.2];



In the case of the third reaction (22), they confirmed the transmutation from ¹³⁷₅₆Ba and ¹³⁸₅₆Ba to ¹⁴⁹₆₂Sm and ¹⁵⁰₆₂Sm, respectively [1.22]. These cases are explained by the reaction associated with the neutron drop ¹²₆δ.

In addition to the data of nuclear transmutations catalyzed by the ^A_Zδ, they determined the locality of the positions where occur these NTs to generate Pr, Mo and Sm by using 100- and 500-micron x-ray beams.

The localization of the nuclear transmutation confirmed in this experiment reminds us the localization of tritium observed by Iyengar et al. [1.3]. These localizations of nuclear products may be explained by the positive feedback mechanism described in our paper on the complexity [1.24] occurring in this case in localized regions.

In conclusion, their extensive data sets determined the localization of nuclear reactions

resulting in the NTs at hot spots with a diameter up to 10 to 50 nm (100 to 500 Å) in the surface layer of thickness up to 10 nm (100 Å).

2.10 Data by Szpak et al. [1.25 – 1.28]

Szpak et al. used a specific sample of the co-deposited Pd/D films on Au foils and Ni screens to observe the CFP with CR-39 and other techniques. Spectacular results obtained by them include localization of the heat sources in close proximity to the electrode-solution contact surface, occurrence of pits, or localized “hot spots,” change of surface morphology (cauliflower, dendrite, fractal), nuclear transmutations generating Al, Mg, Ca, Si, Zn and so on, generation of tritium, emission of energetic particles including neutrons with energies up to about 10 MeV. Also, they observed effects of static electric field on the excess heat and morphology change. It is interesting that their confirmation of a positive of protium in the Pd system but is less effective than deuterium for the CFP in pits formation. Similar difference between H and D in the Pd system is also observed by Celani et al. [2.7].

The emission of neutrons with energies about 10 MeV is analyzed in the paper presented at JCF11 [2.8].

2.11 Data by Celani et al. [1.29]

Celani et al. have done experiments with new type samples of Pd and Ni wire coated with thin multilayer nano-materials and treated in D₂ and H₂ gas with sample temperature up to 900 C. In the case of Ni wire [1.29], they observed change of surface morphology and changes of amounts (Ti, Cr, Co, As, Ir, Ti are increased and Sr, Pd are decreased) and changes of isotope ratios of Pd and B (¹⁰⁵₄₆Pd and ¹⁰₅B/¹¹₅B ratio decreased) while the amounts of Fe and Ni are constant.

They observed a general tendency for the decrease

of concentrations of isotopes that the smaller the mass number of the isotope, the larger the decrease of its concentration. This tendency seems to show the nuclear transmutation (NT) by the single neutron absorption (2.1).

This mechanism for the NT is also useful to understand the remarkable decreases of $^{105}_{46}\text{Pd}$ and $^{10}_{5}\text{B}/^{11}_{5}\text{B}$ ratio if we consider the large cross-sections for thermal neutron absorption of $^{105}_{46}\text{Pd}$ and $^{10}_{5}\text{B}$ compared to other isotopes (20.25 and 3837 b, respectively). The increase of As may be the result of NT (2.2) by an absorption of $^{42}\delta$ by $^{31}_{71}\text{Ga}$ while the decrease of the latter is not certain by their data. Reactions of this type have been used in Section 2.8 to explain the data by Campali et al. and confirmed by Iwamura et al. [1.20] already.

Their results have shown that the Ni-H system generates excess heat as well as the Pd-D system they used before confirming the long-lasting experience of Focardi et al. [2.9, 2.10].

3. Discussion and Conclusions

As we have shown above that the locality of the CFP is fairly common in protium and deuterium systems, it is necessary to explain it from unified point of view applicable to the both systems. The TNCF model proposed by us [1.1, 2.2 – 2.8] has given qualitative explanation of several data sets some of which are explained in Section 2. It means that the model may contain essentials of physics of nuclear reactions resulting in the CFP.

The local nature of the reaction in the CFP at the surface regions with a depth of about one micrometer ($\mu\text{ m}$) may be explained by the accumulation of neutron Bloch waves and formation of the cf-matter at surfaces elaborated to justify the foundation of the

model (cf. e.g. [1.1] Section 3.7.2.3).

On the other hand, the localization in spots with a diameter of a few $\mu\text{ m}$ is a manifestation of specialty of nuclear reactions catalyzed by the trapped neutrons. Alien nuclei in the surface containing the cf-matter interact with trapped neutrons to induce reactions (2.1) – (2.3). Once a reaction occurs, the liberated energy is used to increase temperature of the site. The higher the temperature of the lattice, the easier the CFP occurs as many experimental data show (e.g. Celani et al. [1.29]). This process gives a positive feedback for the CFP resulting in the changes of the surface morphology observed very often in many experiments by different researchers.

The occurrence of positive feedback in the microscopic region resulting in changes of surface morphology might be an evidence for the macroscopic events observed several times in the process of CF investigation. This possibility had been pointed out in the papers presented at JCF8 [3.1] and ICCF14 [3.2].

The experimental data sets obtained in XLPE (cross-linked polyethylene) showing nuclear transmutations accompanied with water tree formation [3.3] explained by our model [3.4, 3.5] are another example of localization of nuclear reactions in the CFP even if the localization in this case is indirectly exhibited.

Using the experimental data sets introduced in Sections 2 and 3, we can contemplate applicability of the reactions (2.1) – (2.3) considered in the TNCF model.

The single neutron reaction (2.1) have been applied very widely to explain numerical relations between numbers of events N_x and N_y of events X and Y (X, Y : excess heat Q , nuclear transmutation NT, neutron n , triton t , helium 4 (^4_2He), - - -). Taking into further data

obtained recently, we may conclude that the reaction (2.1) is applicable to the situation where the neutron density n_n assumed in the model is not too high ($n_n \leq 10^9 \text{ cm}^{-3}$). Main products of this mechanism are triton, excess heat, and nuclear products with small shifts of mass numbers as many examples given in Section 2. (cf. [2.2] Tables 11.2 and 11.3 or [1.1] Tables 2.2 and 2.3)

The neutron-proton cluster reaction (2.2) have been applied to cases where occur nuclear transmutations with shifts of proton and mass numbers by more than two and four, respectively. Their examples are given in Subsection 2.7 and 2.8 in this paper. This reaction may be applicable to the situation where the neutron density n_n in the model is fairly high ($n_n \geq 10^9 \text{ cm}^{-3}$).

The reaction (2.3) catalyzed by the neutron drop has been used to explain nuclear transmutations with enormous variety of product nuclides observed by Miley et al. [1.16, 1.17] and Mizuno et al. [1.9, 1.10] and Ohmori et al. [1.11, 1.12] in protium and deuterium systems. The situation where the reaction (2.3) occurs may be realized by formation of the cf-matter with a very high value of n_n ($n_n \geq 10^{10} \text{ cm}^{-3}$).

In these more than 20 years after the discovery of the cold fusion phenomenon [2.1], there have been elaborated various investigations cultivating new samples and applying new experimental techniques. As a result, we have wide view on the CFP in protium and deuterium systems; (1) localization of nuclear reactions producing tritium and nuclear transmutations at surface/boundary regions with a depth of about $1 \mu \text{m}$ and a width of about a few μm , (2) neutron emission with energies from about 3 to more than 10 MeV, (3) several laws or regularities of events in the CFP. These features of this phenomenon may be useful to accomplish the physics of the cold fusion phenomenon. We hope that the trial given in this paper serves as a

useful step to the goal.

Acknowledgement

The author would like to express his thanks to Y. Iwamura for the paper [1.23] and to F. Celani for the paper [1.29] making possible to use their detailed data in this paper.

References

- 1.1 H. Kozima, *The Science of the Cold Fusion Phenomenon*, Elsevier Science, 2006. ISBN-10: 0-08-045110-1.
- 1.2 J.R. Morrey, M.R. Caffee, H. Farrar, IV, N.J. Hoffman, G.B. Hudson, R.H. Jones, M.D. Kurz, J. Lupton, B.M. Oliver, B.V. Ruiz, J.F. Wacker and A. Van, "Measurements of Helium in Electrolyzed Palladium," *Fusion Technol.* **18**, 659 (1990).
- 1.3 P.K. Iyengar, "Cold Fusion Results in BARC Experiments" *Proc. 5th International Conf. on Emerging Nucl. Energy Systems.* (1989. Karlsruhe, Germany) p. 291 (1989). And also P. K. Iyengar & M. Srinivasan (Eds), "BARC Studies in Cold Fusion (April-September 1989)" *Report BARC-1500*, (1989).
- 1.4 M. Srinivasan et al., "Observation of Tritium in Gas/ Plasma Loaded Titanium Samples," in *Anomalous Nuclear Effects in Deuterium /Solid Systems* (1990. Provo, Utah, USA), *AIP Conference Proceedings* 228, p. 514. American Institute of Physics, New York.
- 1.5 D.S. Silver, J. Dash and P.F. Keefe, "Surface Topography of a palladium Cathode after Electrolysis in Heavy Water," *Fusion Technol.* **24**, pp. 423 – 430 (1993). And also J. Dash et al., "Changes in Surface Topography and Microcomposition of a Palladium Cathode caused by Electrolysis in Acidified Light Water" *Cold Fusion Sourcebook* (Minsk, Belarus, 1994), pp. 172 – 180 (1994).

- 1.6 W.-S. Zhang and J. Dash, "Excess Heat Reproducibility and Evidence of Anomalous Elements after Electrolysis in Pd/D₂O+H₂SO₄ Electrolytic Cells," *Proc. ICCF13*, pp. 202 – 216 (2008).
- 1.7 M. Okamoto et al., "Behavior of Key Elements in Pd for the Solid State Nuclear Phenomena Occurred in Heavy Water Electrolysis," *Proc. ICCF4*, Vol.3, p.14 (1994), EPRI, Palo Alto, California, USA.
- 1.7 J.O'M. Bockris and Z. Minevski, "Two Zones of 'Impurities' Observed after Prolonged Electrolysis of Deuterium on Palladium," *Infinite Energy*, **5 & 6**, 67 – 70 (1995 – 96).
- 1.9 T. Mizuno, T. Ohmori and M. Enyo, "Anomalous Isotopic Distribution in Palladium Cathode after Electrolysis," *J. New Energy* **1-2**, pp. 37 – 44 (1996)
- 1.10. T. Mizuno et al., "Isotopic Changes of the Reaction Products induced by Cathodic Electrolysis in Pd," *J. New Energy* **1-3**, pp. 31 – 45 (1996)
- 1.11 T. Ohmori, T. Mizuno and M. Enyo, "Isotopic Distribution of Heavy Metal Elements Produced during the Light Water Electrolysis on Gold Electrode," *J. New Energy* **1-3**, pp. 90 – 99 (1996)
- 1.12 T. Ohmori, T. Mizuno, Y. Nodasaka and M. Enyo, "Transmutation in a Gold-Light Water Electrolysis System," *Fusion Technol.* **33**, pp. 367 – 382 (1998).
- 1.13 G.S. Qiao, X.M. Han, L.C. Kong and X.Z. Li, "Nuclear Transmutation in a Gas-Loading H/Pd System," *J. New Energy* **2-2**, pp. 48 – 52 (1997).
- 1.14 E. Campali, G. Fasano, S. Focardi, G. Lorusso, V. Gabbani, V. Montalbano, F. Piantelli, C. Stanghini, and S. Veronesi, "Photon and Particle Emission, Heat Production and Surface Transmutation in Ni-H System," *Proc. ICCF11*, pp. 405 – 413 (2006).
- 1.15 E. Campali, S. Focardi, V. Gabbani, V. Montalbano, F. Piantelli, S. Veronesi and S. Veronesi, "Surface Analysis of Hydrogen-Loaded Nickel Alloys," *Proc. ICCF11*, pp. 414 – 420 (2006).
- 1.16 G.H. Miley, G. Narne, M.J. Williams, J.A. Patterson, J. Nix, D. Cravens and H. Hora, "Quantitative Observation of Transmutation Products occurring in Thin-film coated Microspheres during Electrolysis," *Proc. ICCF6* (1996, Hokkaido, Japan) pp. 629 – 644 (1996).
- 1.17 G.H. Miley and J.A. Patterson, "Nuclear Transmutations in Thin-film Nickel Coatings undergoing Electrolysis," *J. New Energy* **1-3**, pp. 5 – 34 (1996).
- 1.18 J. Patterson, "US Patent #5,607,563" *Elemental Energy (Cold Fusion)*, 22, pp. 3 – 17 (1997).
- 1.19 Y. Iwamura, T. Itoh, N. Gotoh, M. Sakano and I. Toyoda, "Detection of Anomalous Elements, X-ray and Excess Heat induced by Continuous Diffusion of Deuterium through Multi-layer Cathode (Pd/CaO/Pd)," *Proc. ICCF7* (April 20 - 23, 1998, Vancouver, Canada), pp. 167 – 171 (1998). ⁵⁷Fe/⁵⁶Fe ratio increased largely.
- 1.20 Y. Iwamura et al., "Observation of Low Energy Nuclear Reactions induced by D₂ Gas Permeation through Pd Complexes," *Proc. ICCF9* (2002, Beijing, China) pp. 141 – 146 (2005).
- 1.21 Iwamura, T. Itoh, M. Sakano, S. Sakai and S. Kurabayashi, "Low Energy Nuclear Transmutation in Condensed Matter induced by D₂ Gas Permeation through Pd Complexes: Correlation between Deuterium Flux and Nuclear Products," *Proc. ICCF10* (2003, Massachusetts, USA) pp. 435 – 446 (2006).
- 1.22 Y. Iwamura, T. Itoh, M. Sakano, N. Yamazaki, S. Kurabayashi, Y. Terada, T. Ishikawa and J. Kasagi, "Observation of Nuclear Transmutation Reactions induced by D₂ Gas Permeation through Pd Complexes" *Proc. ICCF11*, pp. 339 – 349 (2006)
- 1.23 Y. Iwamura et al., "Observation of Surface Distribution of Products by X-ray Fluorescence spectrometry during D₂ Gas Permeation through Pd

- Complexes” *Proc. ICCF12* pp. 178 – 187 (2006).
- 1.24 H. Kozima, “The Cold Fusion Phenomenon as a Complexity (3) – Characteristics of the Complexity in the CFP –,” *Proc. JCF8*, pp. 85 – 91 (2007).
- 1.25 S. Szpak, P.A. Mosier-Boss, and M. H. Miles, “Calorimetry of the Pd + D Codeposition,” *Fusion. Technol.*, **36** (1999) 234-241.
- 1.26 S. Szpak, P.A. Mosier-Boss, J. Dea and F. Gordon, “Polarized D+/Pd-D₂O System: Hot Spots and ‘Mini-Explosions,’” *Proc. ICCF10*, pp. 13 – 22 (2006).
- 1.27 S. Szpak, P.A. Mosier-Boss, C. Young, F.E. Gordon, “The Effect of an External Electric Field on Surface Morphology of Co-deposited Pd/D Films” *J. Electroanal. Chem.* pp. 284 – 290 (2005).
- 1.28 Szpak et al. “SPAWAR Systems Center-Pacific Pd:D Co-Deposition Research: Overview of Refereed LENR Publications,” *Proc. ICCF14*, pp. 772 - 777 (2010)
- 1.29 F. Celani et al., “First measurement on Nano-coated Ni Wire, at Very High Temperature, under He, Ar, H₂, D₂ Atmosphere and Their Mixtures,” Paper presented at 9th International Workshop on Anomalies in Hydrogen/Deuterium Loaded Metals (Sept. 17 – 19, 2010).
- 2.1 H. Kozima, *Discovery of the Cold Fusion Phenomenon* (Ohtake Shuppan Inc., 1998). ISBN 4-87186-044-2.
- 2.2 M. Fleischmann, S. Pons and M. Hawkins, "Electrochemically induced Nuclear Fusion of Deuterium," *J. Electroanal. Chem.*, **261**, 301 – 308 (1989).
- 2.3 H. Kozima, “Quantum Physics of Cold Fusion Phenomenon,” *Developments in Quantum Physics Researches – 2004*, pp. 167 – 196, ed. V. Krasnoholovets, Nova Science Publishers, Inc., New York, 2004. ISBN 1-59454-003-9.
- 2.4 H. Kozima et al., “TNCF Model Explanation of Cold Fusion Phenomenon in Surface Layers of Cathodes in Electrolytic Experiments” *J. New Energy* **7-1**, pp. 81 – 95 (2003).
- 2.5 H. Kozima and F. Celani, “Brief Explanation of Experimental Data Set of Excess Heat and Nuclear Transmutation in Multiply Nanocoated Ni Wire,” *Proc. JCF11* (in this issue).
- 2.6 H. Kozima, K. Yoshimoto, H. Kudoh, M. Fujii and M. Ohta, “Analysis of Zn and Excess Heat Generation in Pd/H₂ (D₂) System by TNCF Model,” *J. New Energy* **6-3**, pp.97 – 102 (2002)
- 2.7 F. Celani, A. Spallone, T. Toripodi, D. Di Giacchino, P. Marini, V. Di Stefano, A. Mancini and S. Pace, “New Kinds of Electrolytic Regimes and Geometrical Configurations to Obtain Anomalous Results in Pd(M)-D Systems,” *Proc. ICCF6*, pp. 93 – 104 (1996).
- 2.8 H. Kozima, “Neutron Emission in the Cold Fusion Phenomenon,” *Proc. JCF11* (in this issue).
- 2.9 S. Focardi, R. Habel and F. Piontelli, ”Anomalous Heat Production in Ni-H System,” *Nuovo Cimento*, **107A**, 163 (1994).
- 2.10 E.G. Campari, S. Focardi, V. Gabbani, V. Montalbano, F. Piantelli, E. Porcu, E. Tosti and S. Veronesi, ”Ni-H System,” *Proc. ICCF8* pp. 69 - 74 (2000).
- 3.1 H. Kozima, “The Cold Fusion Phenomenon as a Complexity (3) – Characteristics of the Complexity in the CFP –,” *Proc. JCF 8*, pp. 85 – 91 (2007).
- 3.2 H. Kozima, “Complexity in the Cold Fusion Phenomenon,” *Proc. ICCF14* (August 10 – 15, 2008, Washington D.C., USA), Eds. J. Nagel and M.E. Melich, pp. 613 – 617 (2010).
- 3.3 T. Kumazawa, W. Nakagawa and H. Tsurumaru, “A Study on Behavior of Inorganic Impurities in Water Tree,” *Electrical Engineering in Japan* **153**, 1 – 13

(2005).

3.4 H. Kozima, "An Explanation of Nuclear Transmutation in XLPE (Crosslinked Polyethylene) Films with and without Water Trees," *Proc. JCF8*, pp. 44 – 50 (2007).

3.5. H. Kozima and H. Date, "Nuclear Transmutations in Polyethylene (XLPE) Films and Water Tree Generation in Them," *Proc. ICCF14*, pp. 618 – 622 (2010).

Numerical simulation of the motion of cascade vortices in the sub-surface layer

Hiroo NUMATA

Tokyo Institute of Technology, 2-12-1, O-okayama, Meguro Tokyo 152-8552 Japan

E-mail: numata.h.aa@m.titech.ac.jp

Abstract: In the cold fusion experiment, there observed vortex patterns on a thick Pd electrode surface during long-term electrolysis in 0.1M LiOD. To understand the peculiar phenomenon, we had proposed N-cycle model, which is composed of four sequential processes including the CF reaction. In this study, numerical simulation for the analysis of the vortex patterns was performed to elucidate the relation between the vortex formation and the CF reaction. Supposing that the hypothetical particles mass evolved due to the CF reaction energy, we performed the numerical simulation using discretization method for the analysis of 3D motion of the hypothetical particles mass. The experimental results showed that the ejected particles mass from one side to another in a given rectangular box (simulate the sub-surface layer) exhibited a helical trajectory as a function of magnetic field. The traces of the ejected particles mass on another side composed vortex pattern. There has been remained more accurate simulation to examine the structure of the layer and the influence of the magnetic field.

Keyword: Computational fluid dynamics, Pd, Nuclear reaction cycle model, vortex, numerical simulation

1 Introduction

During long-term electrolysis for well annealed thick Pd rod ($9.0\text{ mm}\phi$) in 0.1M LiOD, vortex pattern was observed^{1,2)}. The morphology of the post-electrolysis electrodes revealed the two long faults without any cracks on the surface. Since the formation of this peculiar pattern of vortices can be highly plausible to the result of the Cold Fusion (CF) reaction, the precise mechanism of vortices formation must be elucidated in relation with solid state phenomenon accompanied with long-term evolution of deuterium in 0.1M LiOD. So far, an in-situ measurement of the solid state properties of dilation, resistance and electrode potential revealed that the thick Pd electrode was composed of the core structure enveloped by the sub-surface layer. The latter exhibits non-equilibrium deuterium absorption/desorption reaction. Then, N-reaction cycle model proposed^{3,4)} is composed of four sequential processes: in-taking and compression — triggering (the CF reaction) — scavenging. The last process: scavenging shows the traces of vortex on the electrode surface as a consequence of the process continuation. In the last papers^{5,6)}, the vortex pattern was successfully obtained in 2D space analyzing the motion of the hypothetical particles mass by a numerical simulation method: Lattice gas cellular automata (LGCA) numerical simulation. However, there still remained ambiguity in the vortex and the CF reaction relation. In this study, because of a lack of the computational resource for 3D LGCA simulation, the other numerical simulation method, numerical simulation using discretization method, is applied for the analysis of 3D motion of the hypothetical

particles mass as functions of magnetic field and matrix inhomogeneity.

2 Experimental

2.1 Long-term evolution of deuterium on thick rod Pd electrode in 0.1M LiOD

Cold fusion experiments at ambient temperatures have been conducted by electrolysis of heavy water on a Pd electrode. In Fig.1 the electrolysis

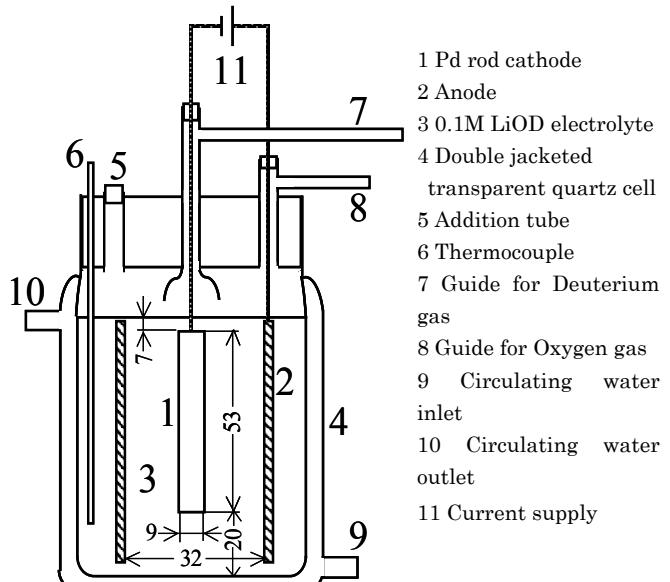


Fig.1 Schematic diagram of electrolytic cell for deuterium absorption on a Pd electrode in 0.1M LiOD.

equipment, especially the geometrical shape and arrangement of the electrode, the counter electrode (anode) and an electrolyte are shown, while the measurement systems with respect to excess heat, neutron emission, and an isothermal water bath are not drawn. Using a potentiostat (or current supply) a constant cathodic current was applied to the Pd electrode on which an evolution of deuterium gas was occurred. By continuing a state where deuterium is strongly absorbed in the Pd electrode, heat generation or emissions of neutrons or charged particles was observed. We successfully performed non-intermittent electrolysis for two and ca. six months with two experimental runs, referred to Exp.1 and Exp.2, respectively. The experimental apparatus and procedures are:

(1) Cast rod Pd electrode (2) Thicker rod Pd electrodes (Rods with 9mm and 21mm diameters¹⁻²⁾ (3) Preparatory gas phase absorption of D₂ (D/Pd = 0.36) (4) Increase in electrolysis current density in a form of stepwise (5) Temperature cycling. The experimental runs were conducted twice in 0.1M LiOD by using the rod Pd electrodes with a diameter of 9mm referred to Exp.1³⁾ and a diameter of 21mm referred to Exp.2.¹⁻²⁾ The surface pretreatment and electrolysis conditions are shown in Table 1 and the results of neutron measurement are described elsewhere.¹⁻²⁾

3 Results and Discussion

3.1 Experimental results of vortex for N-reaction cycle model

As shown in Table 1 the electrolysis for deuterium absorption was conducted as follows; the electrode was removed from the cell and carefully re-installed four times during which the diameter of the electrode was measured at three positions (top, middle and bottom). During 1st run the dilation at the bottom end showed 7 % while in those of 2nd- 4th runs the values at these positions approached asymptotically to 7.8-8.3 %.

Figure 2 shows a significant morphology of a thick rod Pd electrode observed on the surface

Table1 Experimental conditions of Exp.1.

Run No.	Current, mAc ⁻²	Pretreatment
1st	0.05-40	Cast, 800°C anneal(10 ⁻⁶ Torr)
	40-500	Acid treatment
2nd	40	Polishing, Acid treatment, Evacuation, D ₂ gas charge
3rd	40	Evacuation, Polishing, Acid treatment
4th	40	Evacuation, Polishing, Acid treatment

after long-term electrolysis in 0.1M LiOD.^{1-2, 7)} This peculiar pattern was named as a vortex. It is not the substance adhered on the surface, but is a material on which the pattern was deeply impressed in a shape of a ditch. This is the morphology which formation mechanism will be elucidated in the present study.

Alternately, we have investigated the microscopic structural change of Pd absorption/desorption by electrolysis as a fundamental study of deuterium absorption behavior. Although a precise description is not shown in this paper, structural change of discrimination of the sub-surface and the bulk was developed by the deformation during prolonged deuterium absorption.⁸⁻⁹⁾ The above result with respect to the structural change of Pd must be useful in the elucidation of intake of reactant followed by compression of N-cycle model. (see Fig.3)

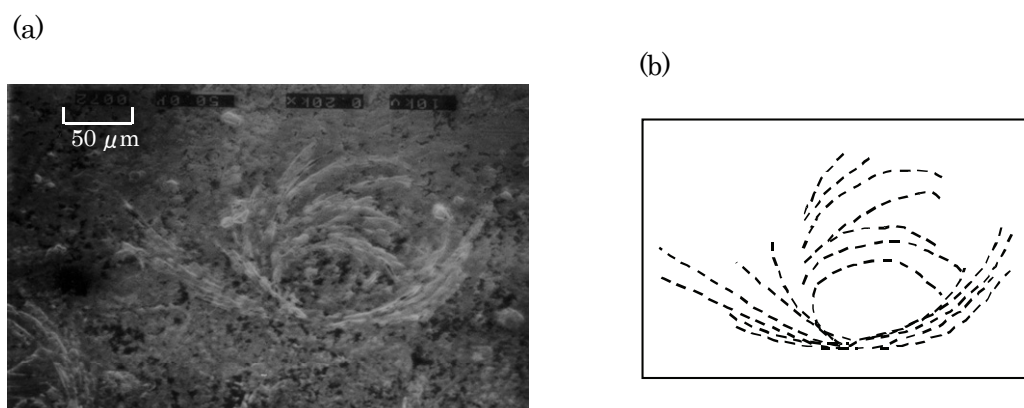


Fig.2 Vortex appeared on Pd electrode surface after long-term electrolysis in 0.1M LiOD (a), Duplicate of SEM picture (b).

3.2 N-reaction cycle model

Considering that such structural changes on the electrode surface and the bulk are related with the CF reaction, it is possible to think these unusual treatments as a precursor to the CF. That is, the electrolysis performance makes the special microstructure (shown below in the simulation model), where that process is named as the intake reactant followed by compression. Next, the CF reaction could be initiated by some trigger. At this moment, in the matrixes around reaction sites the explosive energy of the CF reaction is transferred to the kinetic energy of the mobile hypothetical particles mass. In order to make the explosive energy spread over from the reaction site, the hypothetical particles mass (a group of small charged particles is considered as particles mass in this study) was assumed to be a working medium in the following simulation. Instantaneously, flow with high energy evolves and inevitably interacts with the matrix of the sub-surface layer leaving in vortices on the sample's surface (vortex shown in Fig.2).

Under such an idea, by considering the phenomena as an analogy with an energy engine (4 reciprocating cycle), N-reaction cycle model^{3-4, 8)} was proposed. As schematically shown in Fig.3, it consists of 4 sequential processes: in-take and compression — trigger — reaction — scavenger where instead of the CF reaction and trigger, microstructure formation is incorporated into the successive chain and followed by scavenger. The following two key points are beneficially realized: (1) enhanced reproducibility of the experiments resides in continuation of the cycle (2) on systematic consideration the hindered factors might come to the surface. In Fig.3 the reaction vessel (indicated by double solid lines) is composed of the tough wall, which might be formed after long-term electrolysis or under repeated deuterium absorption/desorption performances. It is noted that the wall functions facile desorptive contraction/sluggish absorptive expansion.^{8,9)}

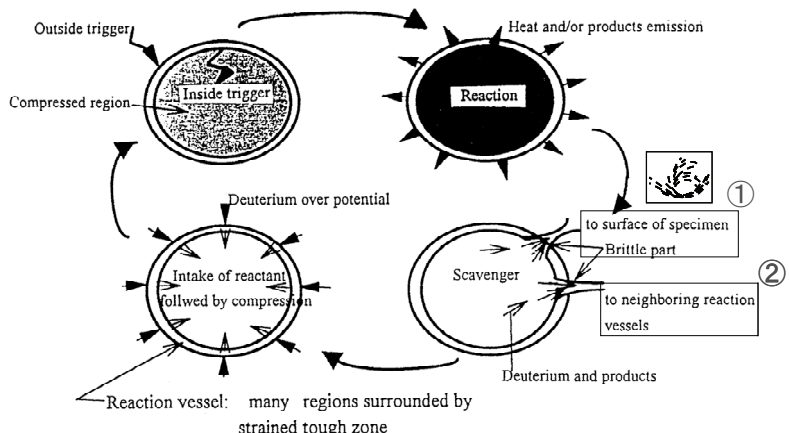


Fig.3 Schematic of nuclear reaction cycle model.

For scavenger the followings are demonstrated; the in-situ measurement of the physicochemical properties of Pd-H(D) system elucidated the formation of fine nano-precipitates: Pd-D_{2-x} in β-phase matrix. These precipitates assume the characteristics of non-equilibrium, hence superplasticity is often observed during their transient state. Therefore, it is envisaged that the above mentioned flow could trail through such matrix: sub-surface layer resulting in the experimentally observed vortices.

3.3 Result of Lattice Gas Cellular Automata for simulating the motion of the hypothetical particles mass in the sub-surface layer

The application of numerical simulation methods helps us to understand microscopic mechanism of the vortices formation in relation with N-cycle model. Before discussion of the numerical calculations, it is noted that there are two numerical simulation methods: LGCA (in Chapters 3.3-3.4) and discretization method (in Chapter 3.5) have been utilized in our work, whereas the goal of both methods is expected to approach toward the same conclusion (characteristics see Appendix 2). Let's focus our attention to the scavenger process after the CF reaction from a microscopic view point. The key issues are the evolution of the hypothetical

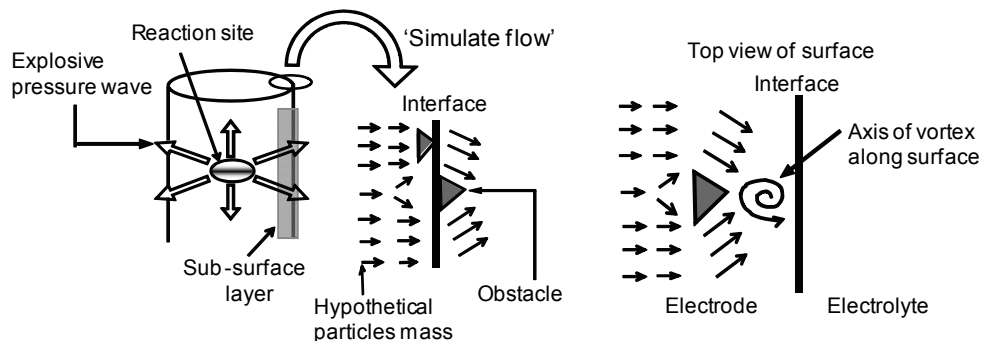


Fig.4 Perspective view of out flow of the hypothetical particles mass and vortex evolved at the interface.

particles mass with high energy, the interaction of particles mass with obstacles, and motion with magnetic field interaction through the sub-surface layer.

In the left of Fig.4, the schematic shows that the hypothetical particles mass with high energy evolves as a Scavenger process after the reaction. Subsequently, they spread outside 360° radial direction, and some parts reach the sub-surface layer. The condition for the radial motion will be established using a long prism crystal.¹⁾ View from upper shows aligned vectors coincidentally rushes towards the interface as ‘Simulated flow’. (see the left of Fig.4) There has been appeared simulated flow vectors normal to the electrode interface. It is easily understood for such flows to be disturbed due to the obstacles. In the right of Fig.4, it shows how evolves a vortex behind an obstacle as a result of flow disturbance. Noticeably, the axis of the vortex is along that of the cylindrical electrode.

Firstly, the results⁵⁻⁶⁾ of LGCA simulation for the vortex pattern are described. The morphological identification of the vortices has been done by comparing the 2D LGCA patterns with those experimentally obtained. The results of the simulation qualitatively well agree with the experimental patterns. By the way, as a necessary condition for this simulation, all the flows should synchronize with the occurrence of the reaction. It is tentative understanding how such flows (composed of the hypothetical particles mass) gain considerable amounts of energy. However, the fusion energy might be transferred to deuterons, and then the hypothetical particles mass near the reaction sites becomes a high pressure. Thus, the motion explosively occurs with surrounding 360° of the reaction sites.

Secondly, obstacles might be embedded beneath the surface due to structural inhomogeneity. The precipitates such as PdO, Li₂O and LiD, and/or vacancy cluster can correspond to actual structural inhomogeneity. In the right of Fig.4, under the flow of the hypothetical particles mass the vortex was evolved behind an obstacle.

More advanced LGCA simulations showed that the cascade of two identical rectangular domains containing each a plate evolved an individual vortex behind each plate.⁶⁾ This suggests the one-to-one correspondence between a simple obstacle and a vortex evolved by the flow. However, this is the case when two obstacles regularly aligned to generate corresponding vortices. In as received Pd such obstacles surely distribute in the matrixes and hence vortices make the different patterns corresponding to the distribution. Then, next research should be directed toward more complicated cases to simulate the motion of the hypothetical particles mass. This research still continues.

3.4 Structure and properties of the sub-surface layer deduced from Scavenger process of N-cycle model

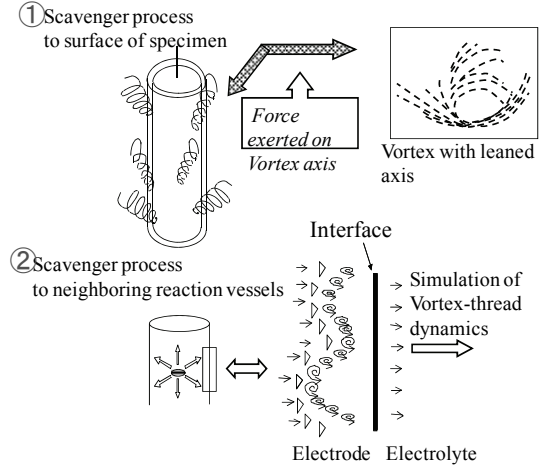


Fig.5 Schematics of vortex with leaned axis and vortex thread during Scavenger process: motion of the hypothetical particles mass from vessel to surface and from a vessel to a neighboring one.

In Scavenger of Fig.3, there were naturally assumed alternative two mechanisms of the hypothetical particles mass motions as a result of N-cycle model examination. One is ① of Fig.3: to electrode surface and another ② of Fig.3: to a neighboring reaction vessel. Two characteristic morphologies of the surface and the underneath microstructure are discussed vide infra, in relation with the appearances of the Scavenger process. In Fig.5① it shows the locus of the occasional particle flow on the Pd surface (correspond to Fig.3 ①), which was identical to the experimentally observed vortex pattern. By comparing the vortex pattern with the experimentally obtained one the axis of the motion leaned due to the interface’s magnetic field.¹⁰⁾ On the other hand, Fig.5② shows the continuous flow of the hypothetical particles mass from a vessel to a neighboring one (corresponds

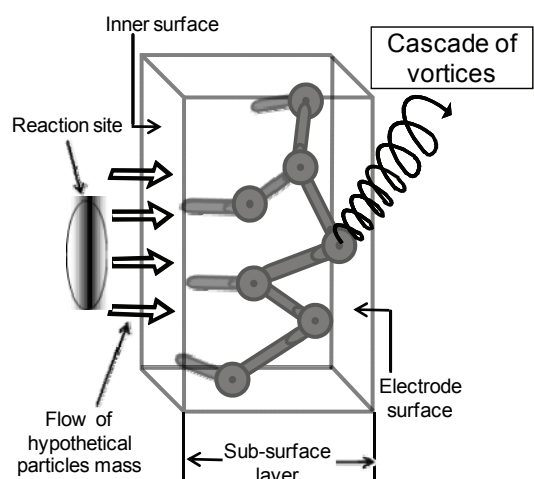


Fig.6 Motion of the hypothetical particles mass and evolved cascade vortices in sub-surface layer.

to Fig.3②). In the right of Fig.5② many vortices are evolved behind obstacles and a cascade of vortices is seen. It has been suspected that the hypothetical particles mass also has the vortex pattern at the electrode surface. Hence, a reasonable inference leads conclude us that the vortex occurred occasionally, while the cascade vortices, vortex-thread, moves underneath the electrode surface. This view might not be inconsistent with the irregularity of sub-surface layer under an annealing at 1100°C.¹¹⁾ Therefore, it is claimed that the appearances of the vortices are strongly concerned with the kinetics of the mass transfer phenomenon underneath the surface.

In Fig.6 the structure of 3D sub-surface layer is schematically shown, where the explosive energy is transferred from the reaction site. There appeared to move the hypothetical particles mass through the thick piping. The vortex threads themselves (see Fig.5②) may enable to move instead of the hypothetical particles mass. However, there still exists ambiguity on how large scale of vortices evolved (actually those diameters range to c.a. 80μm). Then it necessitates to present accurate model with respect to energy and mass transfer in the sub-surface layer. Momentum and mass transportation in the sub-surface layer might be accomplished in the following ways; it holds forward transportation rate and backward one equal implying an equilibrium state, and otherwise net transportation rate with either direction continues implying a non-equilibrium state. (Fig.7) In the latter case, as shown in Fig.7 the net flow encounters by Rayleigh–Taylor’s instability resulting in an evolution of vortices.

Thus, it has become apparent that the electrode surface involving sub-surface layer significantly influences the motion of particles by electromagnetic field and barriers (e.g. wall and obstacle). Since N-cycle model predicted that the hypothetical particles mass explosively spouted out from the reaction site and reached to the area of sub-surface layer, it is required to analyze the

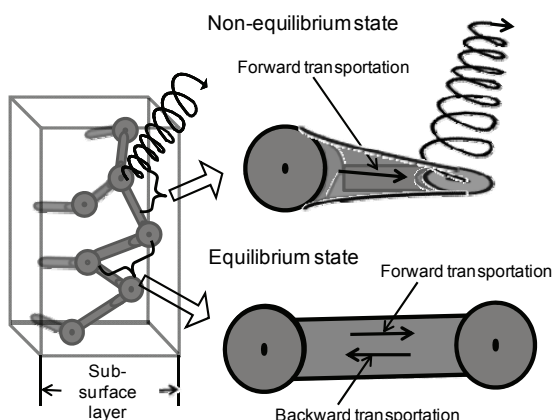


Fig.7 Transportation phenomenon in sub-surface layer and evolution of vortex.

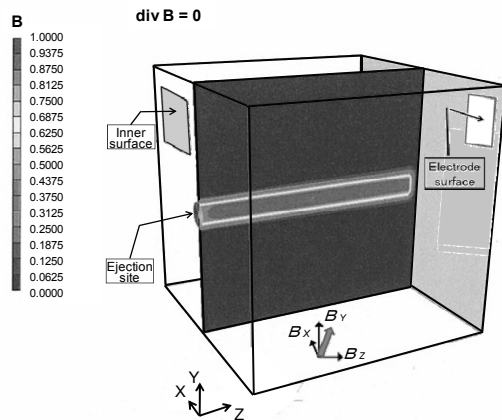


Fig.8 Magnetic field distribution on the ejection site in the sub-surface layer.

motion with magnetic field interaction within the sub-surface layer.

3.5 Motion of the hypothetical particles mass under the influence of magnetic field

We analyzed the motion of the hypothetical particles mass through the sub-surface layer using discretization method (refer Appendix 1) under the influence of magnetic field. As mentioned before, the hypothetical particles mass possessing initial velocity v_0 normal to the inner surface moves through the sub-surface layer. For simulation, the interaction with the magnetic field was incorporated where its distribution is assumed, as shown in Fig.8. It expands like the cylinder on the ejection site. The higher values concentrate along the centerline of the cylinder, while it abruptly attenuates at the periphery of the column. Due to such magnetic field distribution the hypothetical particles mass moves helically confined within the column.

The ejected particles mass trajectory draws helical streamlines as shown in Fig.9. The source of the ejection is set at the inner surface where

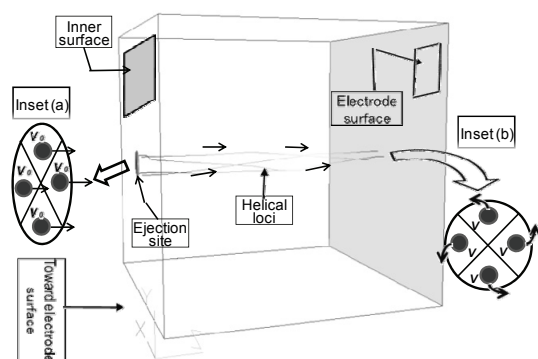


Fig.9 Time evolution of streamlines of the particles mass ejected at the inner surface toward the electrode surface in the sub-surface layer. Inset (a) shows four particles possessing initial velocity v_0 on the quadru poles of the ejection disk and that of (b) shows reached particles possessing velocity v .

four particles mass were artificially placed as shown in the left side of the simulating 3D space. In the figure, each particles mass exhibits a helical streamline reaching at the surface of the electrode. On the electrode four particles mass coincidentally move outside where each particles mass left the corresponding loci. Inspecting the trajectory of the particles mass on the electrode surface, the vector of each particles mass composes curvature with concentric as shown in the inset (b). Supposedly, the shape may exhibit some energetic particles ejected from the sub-surface layer. Thus, the hypothetical particles mass moves 3D space of the sub-surface layer presenting vortex due to the interaction with magnetic field.

Although obstacle's distribution is not taken into, as preliminary, the sources of the energetic particles mass are located at the inner surface from which the flow evolved by the ejection as schematically shown in the inset (a) of Fig.9.

4 Conclusion

In this study, the numerical simulation using discretization method was applied to analyze the motion of the hypothetical particles mass. For simulation the structure and magnetic field distribution in the sub-surface layer were incorporated, and the time evolution of the particles' motion exhibited helical trajectory ejected to the electrode surface. Such moving particles mass with high energy was attributable to the CF reaction energy, as explained using N-cycle reaction model. The traces of ejected particles mass composed the vortex pattern.

Acknowledgement

We would like to express sincere thanks to Mr. T. Suzuki of Concentration Heat and Momentum-Japan Ltd. for technical advices.

References

1. H. Numata et al.: Proc. Conf. Science of Cold Fusion, Vol.33, pp.71, T.BRESSANI et al. eds., SIF, Bologna, Italy (1991)
2. R. Takagi et al.: Fusion Technol., **19** (1991)2135
3. H. Numata et al.: Proc. Mini. Symp. Cold Fusion, Tokyo Metropolitan Univ., pp.129 (1990).
4. H. Numata: Proc. Conf. 3rd New Hydrogen Energy Basic Research, pp.55 (1996)
5. H. Numata and M. Ban: Proc. JCF9, pp.74 (2009)
6. H. Numata and M. Ban: Proc. JCF10, pp.68 (2010)
7. H. Numata and I. Ohno: Fusion Technol., **38** (2000)206
8. H. Numata and I. Ohno: **ICCF6**, Toya Japan, vol.1, pp.213(1997)
9. H. Numata and M. Ban: Proc. JCF7, pp.6 (2006)
10. The magnetic field strength map of the electrolysis system was calculated by ANSYS (FEM) assuming that a cylindrical metal stud was surrounded by an ionic liquid at a given current supply (ex.5A) (refer H. Numata and M. Ban: Proc. JCF6, pp.32 (2005))
11. K. Kandasamy et al.: Surface and Coating Technol., **35**(1988)93

Appendix 1

Kinetic equation of the motion of the hypothetical charged particle (negative unit charge) under magnetic field is shown,

$$\mathbf{F} = q\mathbf{V} \times \mathbf{B}$$

where \mathbf{F} indicates force on charged particle, q electric charge, \mathbf{V} velocity and \mathbf{B} magnetic field strength. Velocity and position of charged particle change with time,

$$\mathbf{V} = \mathbf{V}^{\text{old}} + \mathbf{F}/m \cdot \Delta t$$

$$\mathbf{X} = \mathbf{X}^{\text{old}} + \mathbf{V} \Delta t$$

where \mathbf{X} and \mathbf{V} indicate position and velocity with advanced time $t + \Delta t$, \mathbf{V}^{old} and \mathbf{X}^{old} velocity and position at given time t , m mass, Δt time increment. The followings are initial conditions for \mathbf{X} and \mathbf{V} ,

$$\mathbf{V}_0 = (0, 0, v_0), t = 0$$

$$\mathbf{X}_0 = (0, 0, 0), t = 0.$$

Appendix 2

Scenario and characteristics of the numerical simulations of the hypothetical particles mass's motion in the subsurface layer.

	Cellular automata	Discretization method
principle law of motion	momentum and mass conservation	Maxwell's equation, fluid equation
component particle	fluid element (microscopic)	ejected particles mass flow possessing charge (macroscopic)
driving force, B.C.	pressure difference between inflow and outflow; 2D rectangular domain, incompressible fluid	Electro-magnetic field; 3D hexahedron, incompressible fluid
Advance-ment	cascade of vortices: vortex thread, interaction with obstacles, curved wall, various physical constants	realization of precise electro-magnetic field, evaluation of complex matrix
superiority	incorporation of obstacle's interaction, begin with no budget	easy calculation of complex fluid (ex. 3D and matrix)
semi goal	integrated understanding in relation with N-cycle model	

Neutron Emission in the Cold Fusion Phenomenon

Hideo Kozima

Cold Fusion Research Laboratory, 597-16 Yatsu, Aoi, Shizuoka, Shizuoka 421-1202, Japan

Abstract

The physics of the cold fusion phenomenon (CFP), i.e. low energy nuclear reactions in solids including high density hydrogen isotopes at near room-temperature in a non-equilibrium condition including ambient radiations, has not yet been given appropriate explanations in spite of abundant experimental data obtained in these more than twenty years. We focus on the nature of neutrons from cold fusion (CF) materials observed in these years to investigate mechanisms relevant to nuclear reactions responsible for the neutron emission.

In the data sets by Jones et al. (1989), Shani et al. (1989), Takahashi et al. (1990, 1991), Bressani et al. (1991, 1992), and Okamoto et al. (1993) obtained in the early stage of this field, we point out the energy spectrum of the emitted neutrons extends more than about 7 MeV – which is consistent with recent observation of neutrons with more than 9.6 MeV by Szpak et al. (2008).

The data from De Ninno et al. (1989) shows the bifurcation aspects of the CFP as previously pointed out by us (1999). The neutron vs. tritium ratio N_n/N_t of about 10^{-6} to 10^{-9} observed by Srinivasan et al. (1990) accords with our model ($\approx 10^{-7}$) and is a manifestation of the mechanism relevant to the nuclear reactions simultaneously generating tritons and neutrons in the CF materials.

There is decisive evidence of thermal neutron effects on the neutron emission, (1) null results obtained by Ishida (1992), Jones et al. (1994), Forsely et al. (1998), and (2) enhancements obtained by Shani et al. (1989), Celani et al. (1992), Stella et al. (1993).

The neutron energy spectra extending up to about 10 MeV and the existence of the CFP in protium systems exclude *d-d* fusion as a fundamental nuclear reaction responsible this phenomenon. We have presented therefore a phenomenological model with a single adjustable parameter that is able to explain the experimental facts depicted above qualitatively and sometimes semi-quantitatively.

In this paper, we give an explanation of the characteristics of the neutron emission, the existence of neutrons with energies up to 10 MeV, the bifurcation of temporal evolution and N_n/N_t ratios of the order of 10^{-6} to 10^{-9} , using concepts developed in the phenomenological explanation of events in the CFP. These phenomena are viewed as results of complexity in the CF materials composed of agents (nuclear species) interacting nonlinearly.

Keywords: Cold Fusion Phenomenon, Neutron Emission, Pd-D System, Ni-H System

1. Introduction

The cold fusion phenomenon (CFP) stands for “nuclear reactions and accompanying events occurring in solids with high densities of hydrogen isotopes (H and/or D) in ambient radiation” belonging to the

Solid-State Nuclear Physics (SSNP) or the Condensed Matter Nuclear Science (CMNS). To confirm the existence of nuclear reactions in solids at or near to room temperature, one of the most decisive evidences is the detection of neutrons, which is a direct indication of nuclear reaction [*Science* Section 2.2.1.1], emitted by the solids as have been observed from the beginning of the cold fusion (CF) research in 1989.

Jones et al. [1.1] observed neutron emission from a TiD_x ($x \approx 2$) sample charged deuterium using an electrolytic method in the $\text{Ti}/(\text{D}_2\text{O} + \text{LiOD})/\text{Pt}$ system showing the existence of neutrons with energies from 2.5 up to 8 MeV. At first the data obtained by Jones et al. were considered to show the existence of the d - d fusion reaction generating 2.5 MeV neutrons corresponding to the most significant peak in the observed energy spectrum. Later experiments by others [1.2 – 1.7], however, have shown the existence of higher energy neutrons up to ~ 10 MeV not only in deuterium but also in protium systems. Looking into the spectrum shown in the paper by Jones et al., we notice several small peaks above 2.5 MeV which may be signals corresponding to higher energy neutrons observed later. Recently, Szpak et al. [1.8, 1.9] obtained interesting data showing the existence of neutrons with energies more than 9.6 MeV consistent with previous data sets.

On the other hand, the temporal behavior of neutron emissions shows another feature of nuclear reactions resulting in the neutron emission. The data sets obtained by De Ninno et al. [1.10] have shown statistical behavior of nuclear reactions in CF materials. Similar data were obtained by Menlove et al. [1.12]. The data sets by Srinivasan et al. [1.11] also have shown temporal evolution of neutron emission and tritium production and also tritium- to-neutron yield

ratios in the majority of these experiments were in the range of 10^6 to 10^9 in accordance with our theoretical value, $N_t/N_n \approx 10^7$.

Battaglia et al. [1.13] have shown the possibility to estimate that about one reaction with neutron emission occurs every 10^{11} reactions in the NiH_x system which has been used to investigate the CFP by their group for more than 10 years.

The data by De Ninno et al. have shown behaviors similar to those discovered in complexity and suggest nonlinear interactions in open and nonequilibrium CF materials resulting in the CFP.

In relation to the mechanism of nuclear reactions in CF materials at room temperature, it is necessary to recognize the decisive role of thermal neutrons on the neutron emission. Shani et al. [1.14], Celani et al. [1.15], and Stella et al. [1.16] have shown that the existence of the thermal neutrons has induced a positive effect on the neutron emission from the PdD_x samples. On the other hand, Ishida [1.17], Jones et al. [1.18], and Forsely et al. [1.19] have obtained null results when there are no background thermal neutrons. These data sets have given support to the decisive role of thermal neutrons in the CFP.

It is helpful to investigate experimental data sets showing neutron emissions from solid materials including high-density hydrogen isotopes (CF materials) from a point of view consistent with nuclear and solid-state physics to give quantum mechanical explanation of nuclear reactions in them. In this paper, we introduce typical data sets including recent ones and give a unified explanation consistent with knowledge of modern solid-state and nuclear physics.

2. Experimental Data

In these 21 years since the discovery of the cold

fusion phenomenon (CFP), very many experimental data sets ranging from excess heat to nuclear transmutation including neutron emission and gamma ray emission have been obtained with ever-increasing variety of experimental conditions and measuring techniques. However, the variety of the experimental data has not met with appropriate theoretical counterparts. We have presented a phenomenological model with an adjustable parameter based on experimental data that successfully explains the experimental data qualitatively and semi-quantitatively [2.1 – 2.3].

The experimental data on neutron emission are divided into two types, one with and one without the energy spectrum.

2.1. Energy Spectra of Emitted Neutrons

The energy spectra of neutrons emitted from CF materials, TiD_x , PdD_x , NiH_x , have been considered as one of the key evidences of nuclear reactions in the system and investigated from the first stage of the research.

The data from Jones et al. [1.1] were the first which indicated the existence of 2.5 MeV neutrons in the spectrum of neutrons from TiD_x . In their spectrum, however, there are weak signals showing higher energy neutrons up to about 10 MeV.

In the same period, Shani et al. [1.14] measured the neutron energy spectrum from a neutron irradiated PdD_x target to show a role of background neutrons in the emission of neutrons from the sample. However, in contrast to their purpose, they also showed enhancement of the reaction rate in PdD_x compared with the gaseous D_2 target.

The existence of higher energy components in the energy spectrum has been shown by Takahashi et al.

[1.2 – 1.3], Bressani et al. [1.4 – 1.6], Okamoto et al. [1.7] in the early period of the research.

Mosier-Boss et al. [1.8, 1.9] have obtained clear evidence showing the existence of high energy neutrons with energies more than 9.6 MeV by a different method, but similar to the above results which had been obtained by several researchers. In their data [1.9], the presence of three α -particle tracks outgoing from a single point is diagnostic of the $^{12}\text{C}(n, n')3\alpha$ carbon break up reaction and is easily differentiated from other neutron interactions occurring within the CR-39 detector. The presence of triple tracks suggests that DT reactions that produce ≥ 9.6 MeV neutrons are occurring inside the Pd lattice.

2.2. Neutron Bursts

On the other hand, the numbers of emitted neutrons have shown different features of the nuclear reactions in CF materials. The first data of this type was obtained by De Ninno et al. [1.10] followed by Menlove et al. [1.12] in TiD_x systems. In the data obtained by De Ninno et al., two interesting features exist which are analyzed in the next section.

A similar neutron emission pattern was obtained by Iyengar et al. in PdD_x systems.

Several investigations on the number of neutrons in relation to other events as tritium generation and excess heat have been reported.

Iyengar et al. [1.11] observed simultaneous production of neutrons and tritium in a Pd-Ag alloy/ $\text{NaOD}/\text{D}_2\text{O}$ system and also concluded that the neutron-to-tritium yield ratios in the majority of these experiments were in the range of 10^{-6} to 10^{-9} .

Battaglia et al. [1.13] observed neutron emission in Ni-H gas contact systems and concluded that the

neutron flux is correlated with the power excess rate increase instead of the power excess level and a neutron emission occurs every 10^{11} reactions related with excess heat generation.

Keeney et al. [2.4] observed neutron emission from gas and acid loaded TiD_x samples with high reproducibility (40%) with almost no background neutrons. In the process of this experiment, the authors emphasize the importance of non-equilibrium conditions. This result seems in contradiction with the effect of thermal neutrons described at the end of Section 1. We surmise that there is an effect of non-equilibrium conditions on the neutron band in the host material and formation of the cf-matter in the guest material, as discussed in our paper [2.5].

The effect of non-equilibrium conditions on the CFP has been observed recently by Celani et al. in NiH_x system for excess heat [2.6].

It should be noticed that the reproducibility of events in the CFP is inevitably qualitative as almost all experimental data sets shows (e.g. Fig. 3 and Table 1 of [2.4]) due to the complexity in the CFP as briefly explained in Subsection 3.2.

3. Analysis of the Experimental Data Sets by the TNCF Model

The experimental data sets introduced briefly in Section 2 tell us various facts related to the physics of the cold fusion phenomenon if we see them from an appropriate point-of-view. First of all, we would like to see them as a phenomenon caused by a common cause. This is the reason why we favor an approach to the various events from a unified point of view using a model based on the experimental data as a whole. [2.1 – 2.3]

Some of the earlier data sets have been analyzed

from that point of view successfully and we give our analysis of data sets given above using the same artifice.

3.1 Energy spectra of emitted neutrons showing a new mechanism

The energy spectra and evidence of high energy neutrons with energies up to about 10 MeV are qualitatively explained by our model as the diagram obtained by simulation shows ([2.3, Fig. 3.1]).

This is decisive evidence of a new mechanism to induce neutrons in CF-materials other than *d-d* fusion reactions supposed to be fundamental nuclear reactions working in the CFP. The nuclear reactions catalyzed or participated by neutrons in the material may be responsible for the CFP, as this simple simulation shows [2.3].

3.2 Complexity exhibited by neutron bursts

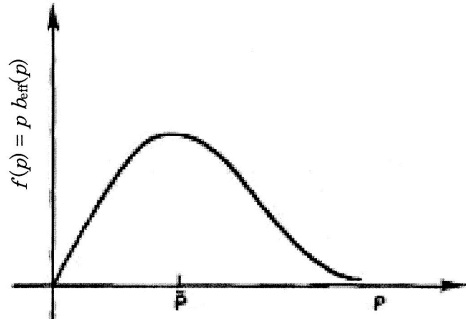


Fig. 3.1 Recursion function $f(p)$ as a function of a variable p : $f(p) = pb_{\text{eff}}(p)$

On the other hand, the temporal evolution of neutron emission observed by De Ninno et al. [1.1 0] and Iyengar et al. [1.11] remind us of the recursion function $f(p)$ (Fig. 3.1) appeared in Feigenbaum's theory [3.1, 3.2]. These data by De Ninno et al. and Iyengar et al. are a rare fortunate gift exhibiting the nature of nuclear reactions as a manifestation of complexity. The point of view including this factor of

complexity has been useful in investigation of the CFP.
[3.1, 3.2]

4. Discussion and Conclusion

The experimental data sets showing neutron emission from TiD_x , PdD_x , and NiH_x samples, a part of which have been introduced in this paper, give clear evidence of nuclear reactions in CF materials composed of transition metals and hydrogen isotopes. The occurrence of nuclear reactions resulting in neutron emission in protium and deuterium systems is decisive evidence of new mechanisms other than $d-d$ reactions supposed to be a cause of the CFP by the pioneers of this wonderful field.

As our simple simulation depicted in Fig. 3.1 [2.3] shows, a mechanism involving neutrons may give a clue to resolve this riddle if we seek a common cause for the CFP both in protium and deuterium systems. The TNCF model proposed by us [2.1 – 2.3] is a trial to explain various observations of physical quantities in the CFP from a unified point of view. The trial is fairly successful giving qualitative and sometimes semi-quantitative explanations for observables in the CFP.

The quantal investigation of the bases of the TNCF model has been employed by us [2.2 – 2.3] using novel data in nuclear physics, solid-state physics and catalytic chemistry. The work has been primitive at present but seems a step toward understanding the complex features of the CFP.

It is also helpful to see CFP from the viewpoint of complexity. We have shown the existence of several laws between observables of the CFP consistent using the laws in the complexity theory [3.1 – 3.3].

In conclusion, we can list up the meaning of the experimental results on the neutron emission as

follows:

1. Neutron emission with neutron energies E_n up to 10 MeV from CF materials has been observed in TiD_x , PdD_x , and NiH_x systems. Thermal neutron effects (null results and enhancements) have been confirmed.
2. We need to discover a mechanism applicable to these events in deuterium and protium systems if we seek a common cause for the neutron emission in the CFP.
3. Our TNCF model gives a possible mechanism applicable to the both systems.
4. Some features of the neutron emission have similarities to the behavior of complexity revealed by logistic difference equation (l.d.e.), as shown in our previous papers.
5. This characteristic of neutron emission suggests nonlinear interactions between agents in the guest material resulting in events of the CFP including nuclear transmutation and neutron emission and therefore excess energy generation.

Acknowledgement

The author would like to express his thanks to Dr. F. Celani for his kindness in providing their recent data on the Ni wire [2.6] and a copy of the paper by Battaglia et al. on the neutron emission in the Ni-H system.

References

- 1.1 S.E. Jones, E.P. Palmer, J.B. Czirr, D.L. Decker, G.L. Jensen, J.M. Thorne and S.E. Tayler, "Observation of Cold Nuclear Fusion in Condensed Matter," *Nature* **338**, 737 – 740 (1989).
- 1.2 Takahashi, A., et al., "Emission of 2.45 MeV and higher energy neutrons from D_2O -Pd cell under biased-pulse electrolysis." *J. Nucl. Sci. Technol.*, **27**, 663 – 666 (1990).
- 1.3 A. Takahashi, T. Iida, T. Takeuchi, A. Mega, S.

- Yoshida and M. Watanabe, "Neutron Spectra and Controllability by PdD/Electrolysis Cell with Low-High Current Pulse Operation" *Proc. ICCF2*, pp. 93 – 98 (1991).
- 1.4 T. Bressani, D. Calvo, A. Feliciello, C. Lamberti, F. Iazzi, B. Minetti, R. Cherubini, A.M.I. Haque and R.A. Ricci, "Observation of 2.5 MeV Neutrons emitted from a Titanium- Deuterium Systems," *Nuovo Cimento* **104A**, 1413 – 1416 (1991). TiD_x, neutron energy spectrum with meaningful signals at about 2.5 MeV and rather ambiguous ones at higher energies up to 8 MeV.
- 1.5 E. Botta, T. Bressani, D. Calvo, Q. Feliciello, P. Gianotti, C. Lamberti, M. Agnello, F. Iazzi, B. Mietti and A. Zecchina, "Measurement of 2.5 MeV Neutron Emission from Ti/D and Pd/D systems," *Nuovo Cimento* **105A**, 1663 – 1671 (1992).
- 1.6 M. Agnello, E. Botta, T. Bressani, D. Calvo, A. Feliciello, P. Gianotti, F. Iazzi, C. Lamberti, B. Ninetti and A. Zecchina, "Measurement of 2.5 MeV Neutron Emission from Ti/D and Pd/D Systems," *Proc. ICCF3* (1992, Nagoya, Japan) pp. 433 – 436 (1992),
- 1.7 Okamoto et al., *Proc. ICCF3* p. 173 – 178 (1993), *Fusion Technol.* **19**, 357 – 359? (1991).
- 1.8 S. Szpak, P.A. Mosier-Boss, F. Gordon, J. Dea, M. Miles, J. Khim and L. Forsley, "LENR Research using Co-Deposition," *Proc. ICCF14* (2008, Washington D.C., USA) pp.? - ? (2010).
- 1.9 P.A. Mosier-Boss, S. Szpak, F.E. Gordon, and L.P.G. Forsley, "Triple Tracks in CR-39 as the Result of Pd/D Co-deposition: Evidence of Energetic Neutrons," *Naturwissenschaften*, in press. (2008).
- 1.10 A. De Ninno, A. Frattolillo, G. Lollobattista, G. Martinio, M. Martone, M. Mori, S. Podda and F. Scaramuzzi, "Evidence of Emission of Neutrons from a Titanium-Deuterium System," *Europhys. Lett.* **9**, 221 – 224 (1989).
1. 11 P.K. Iyenger and M. Srinivasan, "Overview of BARC Studies in Cold Fusion," *Proc. ICCF1* (1990. Salt Lake, U.S.A.), pp. 62 – 91 (1990). 1.12 H.O. Menlove, M.A. Paciotti, T.N. Claytor and D.G. Tuggle, "Low-Background Measurements of Neutron Emission from Ti Metal in Pressurized Deuterium Gas," *Proc. ICCF2* (1991, Como, Italy), pp. 385 – 394 (1991).
- 1.13 A. Battaglia, P. L. Daddi, S. Focardi, V. Gabbani, V. Montalbano, F. Piantelli, P. G. Sona and S. Veronesi, "Neutron Emission in Ni-H System," *Nuovo Cimento* **A112**, 921 – 931 (1999).
- 1.14 G. Shani, G. Cohen, A. Grayevsky and S. Brokman, "Evidence for a Background Neutron Enhanced Fusion in Deuterium Absorbed Palladium," *Solid State Comm.* **72**, 53 (1989).
- 1.15 Celani et al., "Search for Enhancement of Neutron Emission from Neutron-Irradiated, Deuterated High-Temperature Superconductors in a Very Low Background Environment," *Fusion Technol.* **22**, 181 (1992).
- 1.16 Stella et al. "Evidence for Stimulated Emission of Neutrons in Deuterated Palladium," *Frontiers of Cold Fusion (Proc. ICCF3)* (1992, Nagoya, Japan), p. 437 (1993).
- 1.17 Ishida, "Study of the Anomalous Nuclear Effects in Solid-Deuterium Systems," *Master Degree Thesis*, Tokyo University, February 1992.
- 1.18 S.E. Jones, D.E. Jones, S.S. Shelton and S.E. Tayler, "Search for Neutron, Gamma and X-Ray Emission from Pd/LiOD Electrolytic Cells; A Null Results," *Trans. Fusion Technol.*, **26**, 143 (1994).
- 1.19 L. Forsley, R. August, J. Jorne, J. Khim, F. Mis and F. Phillips, "Analyzing Nuclear Ash from the Electrocatalytic Reduction of Radioactivity in Uranium and Thorium," *Proc. ICCF7*, pp.128 – 132 (1998)

2.1 H. Kozima, *Discovery of the Cold Fusion Phenomenon* (Ohtake Shuppan Inc., 1998). ISBN 4-87186-044-2.

2.2 H. Kozima, H., "Quantum Physics of Cold Fusion Phenomenon," *Developments in Quantum Physics Researches – 2004*, pp. 167 – 196, ed. V. Krasnolovets, Nova Science Publishers, Inc., New York, 2004. ISBN 1-59454-003-9

2.3 H. Kozima, *The Science of the Cold Fusion Phenomenon*, Elsevier Science, 2006. ISBN-10: 0-08-045110-1.

2.4 F.W. Keeney, S.E. Jones, A.C. Johnson, P.L. Hagelstein, G. Hubler, D.B. Buehler, F.E. Cecil, M.R. Scott and J.E. Ellsworth, "Neutron Emission from Deuterided Metals," *Proc. ICCF10*, pp. 525 – 533 (2003).

2.5 H. Kozima, "Localization of Nuclear Reactions in the Cold Fusion Phenomenon" *Proc. JCF11* (in this issue).

2.6 F. Celani et al. "First measurement on nano-coated Ni wire, at very high temperature, under He, Ar, H₂, D₂ atmosphere and their mixtures," Paper presented at 9th International Workshop on Anomalies in Hydrogen/Deuterium Loaded Metals (Sept. 17 - 19, 2010, Pontignano, Italy).

3.1 H. Kozima, "The Cold Fusion Phenomenon as a Complexity (2) – Parameters Characterizing the System where occurs the CFP –" *Proc. JCF8* (Nov. 29 – 30, 2007, Kyoto, Japan), pp. 79 – 84 (2008).

3.2 H. Kozima, "Complexity in the Cold Fusion Phenomenon," *Proc. ICCF14* (August 10 – 15, 2008, Washington D.C., USA), pp. 613 – 617 (2010).

3.3 H. Kozima, "The Cold Fusion Phenomenon as a Complexity (3) – Characteristics of the Complexity in the CFP –" *Proc. JCF8* (Nov. 29 – 30, 2007, Kyoto, Japan), pp. 85 – 91 (2008).